QUANTIFYING THE IMPACT OF PUMP PERFORMANCE, CHEMICAL CONVERSION, AND MATERIAL PROPERTIES ON SOLAR HYDROGEN PRODUCTION

A Thesis
Presented to
The Academic Faculty

by

Colby Lewis Jarrett

In Partial Fulfillment
of the Requirements for the Master's Degree
Mechanical Engineering from the
George W. Woodruff School of Mechanical Engineering

Georgia Institute of Technology
December 2014

QUANTIFYING THE IMPACT OF PUMP PERFORMANCE, CHEMICAL CONVERSION, AND MATERIAL PROPERTIES ON SOLAR HYDROGEN PRODUCTION

Approved by:

Dr. Asegun Henry, Advisor
School of Mechanical Engineering
Georgia Institute of Technology

Dr. Kenneth Sandhage
School of Materials Science and Engineering
Georgia Institute of Technology

Dr. Baratunde A. Cola
School of Mechanical Engineering
Georgia Institute of Technology

Date Approved: October 20, 2014

ACKNOWLEDGMENTS

First, I would like to thank my mother, father, and sister for their never ending support. Their love is my cornerstone and without it, completing this thesis would not have been possible. Secondly, I would like to thank my advisor, Dr. Asegun Henry for everything he has provided during this process. His support, drive, critique, and patience motivated me beyond what I thought was possible. I sincerely enjoyed his guidance during my time at Georgia Tech, and I know I benefited greatly from a creative thoughtful mentor.

I would also like to that the many other faculty members of Georgia Tech who contributed the work of my thesis. Specifically, thank you to Dr. Kenneth Sandhage for taking time to answer my many questions and provided a valuable material science point of view. His detailed critique and contributions greatly improved this thesis. A special thank you to our collaborator, Dr. William Cheuh of Stanford University for teaching me the material science topics required to complete this work and always making himself available to answer questions and trouble shoot the experiments. This work would not have been possible without his input from both an engineering and material science prospective.

Additionally, I would like to thank every member of my research group at Georgia Tech for all the help I received. I thoroughly appreciated collaborative and productive environment that Dr. Henry and his group work hard to maintain. Furthermore, thank you to Dr. Shannon Yee and his research group for the comments and recommendations regarding my work during group meetings.

I would also like to thank the many fellow graduate students that I have come to know as dear friends. I would not have made it through the many challenges of graduate school without their friendship and I am grateful that I have gotten to know many wonderful people. In addition, thank you to my dearest friend, Johnathan Miller, for being and endless source of motivation and encouragement.

Finally, I would like to thank the ARPA-E agency for the financial support of project DE-AR0000339, through which this work was made possible.

TABLE OF CONTENTS

LIST OF TABLES

Page

LIST OF FIGURES

Page

LIST OF SYMBOLS AND ABBREVIATIONS

OSM	Oxygen Storage Material
OSC	Oxygen Storage Capacity
TGA	Thermogravimetric Analysis
H_2O	Water Molecule
H_2	Hydrogen Molecule
O_2	Oxygen Molecule
ΔG	Change in State Gibbs Free Reaction Energy
ΔH	Standard State Reaction Enthalpy upon Reduction
ΔS	Standard State Reaction Entropy upon Reduction
T	Temperature
R	Universal Gas Constants
K_{WS}	Chemical Equilibrium Constant for Water Dissociation
p_{O_2}	Oxygen Partial Pressure
p_{H_2}	Hydrogen Partial Pressure
p_{H_2O}	Water Partial Pressure
p_{Total}	Pressure
η	Thermal to Chemical Conversion Efficiency
T_H	Reduction Temperature
T_L	Oxidation Temperature
M_xO_y	Metal Oxide OSM
M	Metal Oxide OSM reduced to a Pure Metal

NRC	Nonstoichiometric Redox Cycle
δ	Off-Stoichiometry of OSM
δ_R	Off-Stoichiometry of OSM after Reduction
δ_O	Off-Stoichiometry of OSM after Oxidation
n_{H_2}	Moles of Hydrogen Produced per Mole of OSM per Cycle
n_{H_2O}	Moles of Water Used for Oxidation per Cycle
CeO_2	Cerium Oxide
O_O^x	Oxygen Atom on an Oxygen Lattice Site
Ce_{Ce}^x	Cerium Atom on a Cerium Lattice Site
$V_O^{\cdot\cdot}$	Doubly Ionized Oxygen Vacancy
$Ce_{Ce}^{'}$	Cerium Atom on a Cerium Lattice Site with a single Localized Electron
K_{ws}^{KV}	Chemical Equilibrium Constant Ceria Oxidation with Water (Kröger–Vink)
CO_2	Carbon Dioxide Molecule
CO	Carbon Monoxide Molecule
W_{Pump}	Work to Drive the Vacuum Pump
Q_{Total}	Total Energy Input to System
Q_{Reheat}	Energy Needed to Heat OSM from T_L to T_H
Q_{RXN}	Energy of Endothermic Reduction Reaction
Q_{Water}	Energy Needed to Generate Steam at T_L
Q_{Out}	Energy Removed when Cooling OSM from T_H to T_L
ε_S	Efficiency of solid phase heat Recovery
ε_G	Efficiency of Gas Phase Heat Recovery

Δt	Cycle Time
Q_{Loss}	Heat Leak from the System
HHV_{H_2O}	Higher Heating Value of Hydrogen
LHV_{H_2O}	Lower Heating Value of Hydrogen
C_P^{OSM}	Molar Specific Heat of the OSM
$C_P^{H_2O}$	Molar Specific Heat of Water
F_{Reheat}	Energy Factor for Temperature Change
F_{RXN}	Energy Factor for Endothermic Reduction
F_{Water}	Energy Factor for Generating Steam
F_{Pump}	Energy Factor for Generating Steam
F_{Loss}	Energy Factor for Heat Leak
R_{TM}	Ratio of OSM Thermal Mass to Inert Reactor Thermal Mass
$\dot{Q}_{Re\text{-}Rad}$	Heat Leak Rate from Re-radiation at the Solar receiver
C_{H_2O}	Extent of Chemical Conversion of Steam into H_2 During OSM Oxidation Step
R_{H_2O}	Ratio of Water to Hydrogen
$R_{\Delta H}$	Ratio of ΔH to the Change in Enthalpy of Water Dissociation
η_{Pump}	Efficiency of Vacuum Pump
$T°$	Reference temperature
$P°$	Reference Pressure
R	Gas Constant
W_{Pump}^{ideal}	Ideal Pump Work
$W_{Friction}$	Lost Frictional Work of Vacuum Pump
ΔH_{H_2O}	Enthalpy of Liquid Water Dissociation

ΔH^{Steam}	Enthalpy of OSM Oxidation with Steam
$h^{s}_{M_xO_{y-\delta_O}}$	Specific Enthalpy of an OSM
$h^{g}_{O_2}$	Specific Enthalpy of Oxygen gas
$h^{g}_{H_2}$	Specific Enthalpy of Hydrogen Gas
$\dot{Q}_{Loss}$	Heat Leak Rate
n_{O_2}	Moles of Oxygen Produced per Mole of OSM per Cycle
V	Voltage
F	Faraday's Constant
MM	Molar Mass
DSC	Differential Scanning Calorimetry
r	Atomic Radius
ρ^{atomic}	OSM Atomic Density
A_C	Avogadro's Constant

SUMMARY

.

As renewable energy production becomes more prevalent, the challenge of producing renewable dispatchable fuel for the transportation sector remains unresolved. One promising approach is to produce hydrogen from solar energy which can be used directly as a fuel or a precursor to synthetic liquid hydrocarbon fuel. Of the methods to produce hydrogen from solar energy, two step thermochemical cycles show the most promise for high conversion efficiency. A two-step thermochemical reactor produces hydrogen through two reversible reaction steps which use a recycled intermediate oxygen storage material (OSM).

Due to the strong coupling between reactor design, operational parameters, and OSM properties, the direct comparison of two OSMs is not straightforward. The oxygen storage capacity (OSC) of an OSM describes the number of oxygen vacancies that are created and used to split water during each cycle. Therefore, a material's OSC is a direct measure of the hydrogen produced per cycle. Currently, many studies which investigate new OSMs for water splitting simply measure OSC of two materials under common reduction and oxidation conditions. Also for such studies, the OSM is completely re-oxidized to near stoichiometry. However for two different OSMs, peak performance is likely to occur at different operating conditions and simply comparing the OSC will not determine the better preforming material, particularly if the complete re-oxidation of the OSM requires large amounts of unreacted steam which must be preheated.

In order to guide the designs of OSMs for two-step thermochemical hydrogen production, first Chapter 2 develops a methodology to model the max performance

possible for a two-step thermochemical cycle. The novel contribution of this model considers the strong coupling between reactor operation, OSM properties, and reactor performance. The results highlight the importance of examining the work required to reduce the oxygen partial pressure during reduction and the energy needed to produce the steam required for re-oxidation. Next, with the aim of achieving higher thermochemical efficiencies, the systematic change of OSM material properties is explored. By optimizing reactor operating conditions for each new value of a particular OSM property, maximum efficiencies are calculated. These results demonstrate important implicit relations between OSM and reactor operating conditions, and also qualitatively bound this particular OSM material property. Furthermore, these results show how the measuring and comparing the OSC under one condition alone is not a sufficient assessment of new OSMs.

With the need for a more sophisticated method of evaluating OSM performance (beyond measuring only OSC), a method utilizing thermogravimetric analysis (TGA) is proposed in Chapter 3. This approach utilizes TGA to map the off-stoichiometry of a new OSM. With this data, the modeling method developed in Chapter 2 is applied to determine maximum reactor efficiency possible for the conditions considered. Furthermore, an OSM screening method is reviewed which measures the OSC of a material under conditions which do not require excessive amounts of work to reduce the oxygen partial pressure during reduction or prohibitively large amounts of unreacted steam during oxidation. The combination of these two OSM evaluation methods allows many materials to be evaluated quickly, and facilitates further characterization new OSMs to determine if they show promise as potentially high performance materials.

Additionally, by comparing the predicted maximum efficiency of a new OSM with the efficiency of current OSMs, this method facilitates the comparison of two different OSMs on equal footing.

Finally, Chapter 4 describes the experimental equipment and methodology required for this approach and also highlights important considerations specific to evaluating the off-stoichiometry of an OSM via TGA. This experimental setup and methodology are then used to screen two batches of OSMs for high OSC without requiring prohibitively large amounts of unreacted steam for re-oxidation in Chapter 5. Lastly, the method described in Chapter 2 is applied to predict the maximum efficiencies possible with a new OSM from the off-stoichiometry measured via TGA. While this material does not perform better than the state of the art OSM (ceria), it does demonstrate how these types of materials could indeed be promising and warrant further investigation.

CHAPTER 1

INTRODUCTION

Pollution, greenhouse gas generation, global warming, and finite natural hydrocarbon reserves are all shortcomings of energy derived from fossil fuels. These issues make the development of a clean, sustainable energy infrastructure a pressing technological challenge [1-7]. [8]. Photovoltaics and concentrated solar thermal power are becoming more established technologies for grid electricity production, but the issue of finding a path to renewable and dispatchable fuel for the transportation sector remains a daunting challenge. One promising approach which has received attention for over 50 years is to chemically store energy from solar radiation by splitting water to produce hydrogen. Here, hydrogen can service a dispatchable fuel or feed stock for the production of synthetic liquid hydrocarbon (i.e. Fischer-Tropsch Process) [9-13]. In this chapter, methods of producing hydrogen from solar energy will be review and one particular method (two-step thermochemical cycles) will be highlighted, explained, and motivate as the topic of this thesis.

Storing Solar Energy Chemically

Solar energy can be employed to split water in many ways such as solar driven electrolysis [4, 5, 14-16], photocatalysis[17, 18], and direct water thermolysis [13, 19, 20]. However, the maximum efficiency of solar driven electrolysis is limited to the efficiencies of electricity production (40%-60%). Combined with collection losses and electrolyzer losses, the maximum solar to chemical conversion efficiencies for solar driven electrolysis are typically reported at 10-25% [15, 21-23]. On the other

hand, photocatalysis does not require electricity production however, this approach only uses a portion of the solar spectrum and its maximum efficiency is limited to the portion of the solar spectrum it utilizes [24]. In contrast, direct solar driven water thermolysis does not inherently require thermodynamic work (e.g. electrical input) and utilizes the entire solar spectrum. These attributes make direct water thermolysis a simple, straightforward approach to solar fuel production which has high theoretical efficiencies compared to electrolysis and photocatalysis [20, 25, 26]. The chemical reaction for direct water thermolysis is shown below.

$$H_2O \rightarrow H_2 + \frac{1}{2}O_2 \tag{1.1}$$

However to completely split water, this chemical reaction must be thermodynamically favorable, meaning the change in standard state Gibbs free energy (ΔG) must be less than or equal to zero. ΔG is composed of the change in enthalpy (ΔH) and change in entropy (ΔS) of the reaction. This relation is shown in Eq. (1.2) where T is the absolute temperature. For reaction (1.1), ΔH and $T\Delta S$ are shown as functions of temperature in Figure 1.1.

$$\Delta G = \Delta H - T\Delta S \tag{1.2}$$

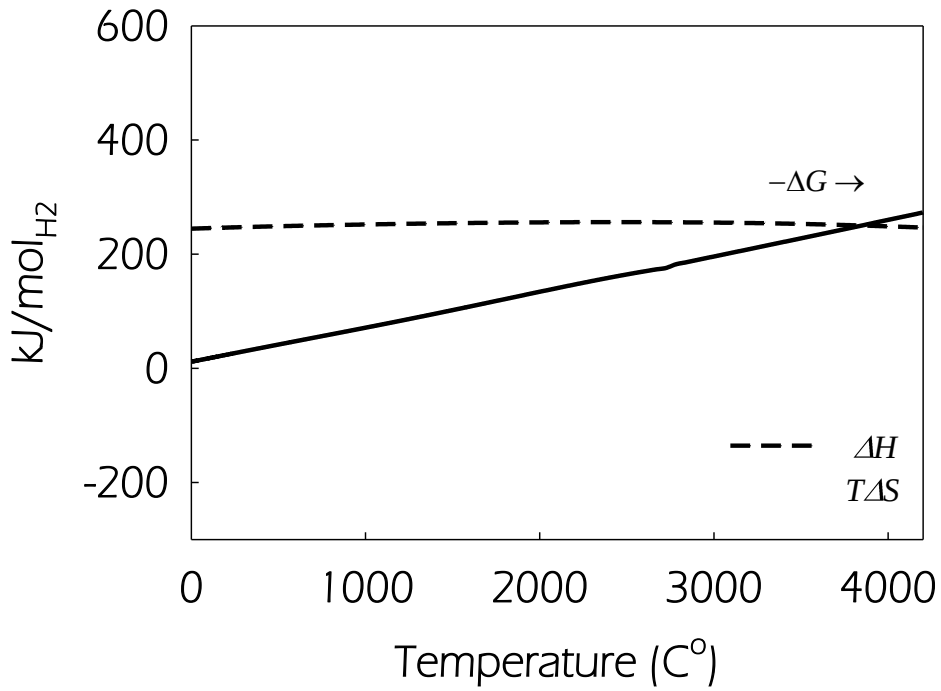

Figure 1.1: The change in enthalpy (ΔH) and entropy (ΔS) for water thermolysis vs. temperature.

The value of ΔH for water dissociation is relatively low (241 kJ/mol H_2), but ΔS is also small because one gas reacts to from another gas (water reacts to form a hydrogen and oxygen gas mixture). Therefore, to have values of ΔG that are less than or equal to zero, high temperatures are required to make the absolute value of $T\Delta S$ become larger than the value of ΔH . While temperatures near 4000°C are required for reaction (1.1) to proceed to completion and convert a large percentage of the available water to hydrogen, moderate dissociation of water can be achieved at lower temperatures.

If the temperatures required for reaction (1.1) to proceed to completion are not achieved, ΔG determines the oxygen, hydrogen, and water partial pressures present at chemical equilibrium, and is defined through the equation below.

$$\Delta G = -RT \ln\left(K_{WS}\right) = -RT \ln\left(\frac{p_{o_2}^{1/2} \times p_{H_2}}{p_{H_2O}}\right) \tag{1.3}$$

where R is the universal gas constant, K_{WS} is the equilibrium constant for reaction (1.1), and p_{O2}, p_{H2}, and p_{H2O} are the partial pressures of oxygen, hydrogen, and water respectively. Under these conditions, the percent of water which is split to produce hydrogen as determined by equation (1.3) is shown below.

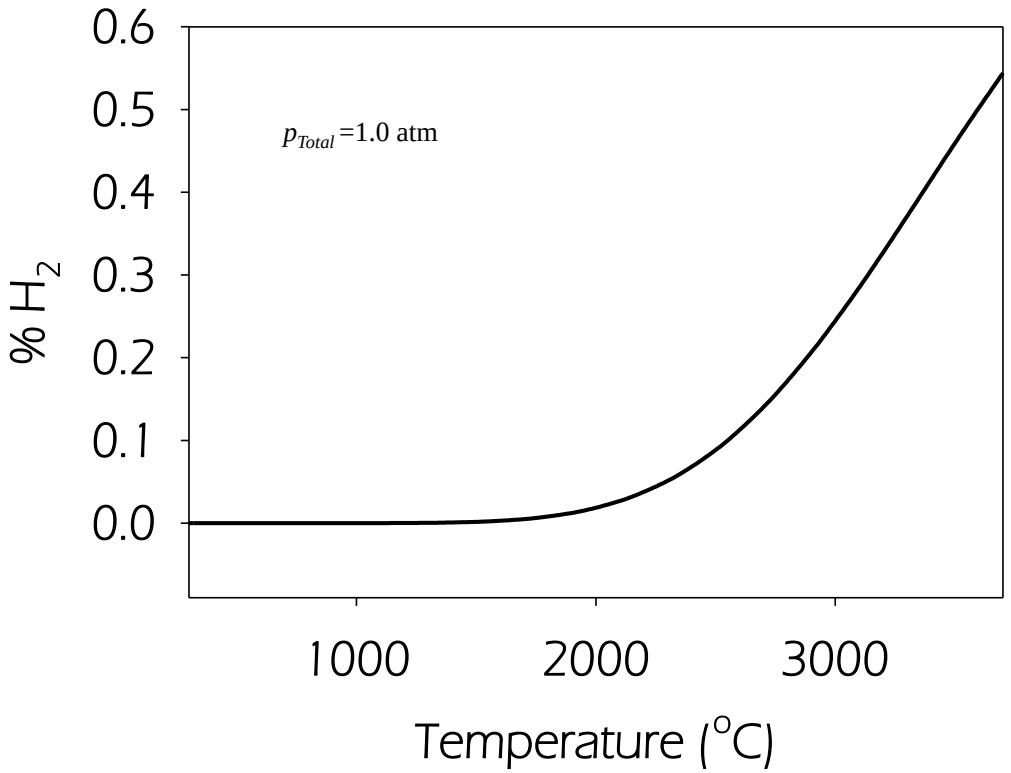

Figure 1.2 Percent of water converted to hydrogen by direct water thermolysis predicted by thermal equilibrium at different temperatures.

For direct water thermolysis at lower temperatures, only a fraction of the water is converted to hydrogen which is then separated from the remaining water and oxygen. However, even at 2500K this technology's feasibility is limited because of radiation losses through the solar receiver aperture, compatible reactor materials, and the difficulty of separating the gaseous reaction products before they are cooled and recombined [13].

Thermochemical Cycles

The high temperatures required for solar driven thermochemical hydrogen production can be reduced by dividing Eq. (1.1) into two or more reaction steps. Furthermore, this pathway produces oxygen and hydrogen in separate reaction, eliminating issues of gaseous product separation. Many different reaction cycles can be used for solar driven hydrogen production, and they vary in the number of reaction steps. Processes with larger number of steps typically require lower maximum temperatures but suffer from reduced efficiency due to heat recovery and product separation throughout the many steps. Processes with fewer steps can have higher efficiencies but typically require higher maximum process temperatures. Hundreds of thermochemical cycles with varying numbers of reaction steps have been proposed and investigated for water thermolysis [9, 12, 27]. Abanades et al. [27] reviewed 280 of these processes and screened them according to the following criteria: maximum required temperature, number of reaction steps, number of chemical elements in the cycle, technical feasibility, economic feasibility , predicted exergy efficiency, and environmental safety. The authors highlighted cycles with fewer steps (e.g. two steps cycles) as the most promising cycles due to their simplicity and high theoretical

efficiency [13, 15, 28-38]. Furthermore, recent improvements in solar concentrators have increased the maximum temperature at which solar radiation can be collected, making the two step cycles even more attractive.

Conceptually, a two-step thermochemical cycle can be based on an oxygen storage material (OSM) or a hydrogen storage material. However, many metal hydrides lack the necessary high temperature stability and bond strength to facilitate efficient water splitting. Therefore, this thesis only focuses on oxygen storage based cycles which utilize an intermediate OSM to absorb and release oxygen through two revisable reactions: one which produces oxygen gas and one which split water to produce hydrogen gas.

State of the Art

Typically, new technologies are compared against the current commercially viable reference technology for process evaluation. Currently, commercial solar-driven hydrogen production does not exist but could achieved by coupling commercial solar electricity production to available alkaline electrolyzes [12]. Siegel et al. [15] obtained values of 11%, 13%, and 18% for the annual theoretical efficiency of electrolysis driven by photovoltaic, molten salt tower, and dish stirling sources respectively. These lower efficiencies are partially caused by significant losses from electricity production (40-60%), losses which are avoided by thermochemical hydrogen production [9]. While efficiencies for water electrolysis can vary, the minimum efficiency goal for solar driven thermochemical hydrogen production to become commercially viable is typically reported between 20-25% [12, 15, 27]. This goal requires thermal to chemical conversion efficiencies (thermochemical conversion

efficiency, η) between 30-45%, after solar collection losses are considered [15]. However, it should be noted that other techno-economic analyses have shown that solar driven thermochemical fuel production can be economically viable at thermochemical conversion efficiencies of 20% [39, 40].

While reports on the required efficiency for commercialization differ, currently even the lowest of these target efficiencies is not possible. Even though the potential for efficiencies above 30% has been confirmed by models of thermochemical reactors [15, 32, 35], these high predicted efficiencies have yet to be realized in practice. Efficiency improvements have been achieve by implementing synthesized OSM monoliths to exploit high density and macro-porosity which increases both OSM mass loading and volumetric absorption of concentrated solar radiation. However, current demonstrated average operating efficiencies are on the order of 1%, with peak efficiencies limited to 4%[29]. These values are still far below the 20-30% metric for commercial viability. For these demonstrations, reactor use direct radiation to heat the OSM. This method of heating creates a power mismatch between incoming solar energy and chemical fuel generated, limiting system efficiency. However, new reactor designs and improved OSMs could mitigate the losses associated with this power mismatch, increases thermochemical efficiency.

The primary focus of this work will be the possible enhancement of thermochemical performance through the implementation of improved OSMs. With many OSM options and material variations enabled by alloying, it is important to establish a framework for evaluating the extent to which such materials can actually improve the system level efficiency. In the next chapter, a general framework is

developed that, for the first time, allows for the optimization of thermochemical conversion efficiency for two step thermochemical cycle by simultaneously considering the OSM properties and operating conditions of the thermochemical two-step redox cycle. Using ceria as the base-case OSM, we explore the potential improvement from employing an alternative OSMs by highlighting two system energy inputs which previously have not been studied in detail (the energy required to drive the vacuum pump and the energy needed to preheat unreacted water used for oxidation). Furthermore we demonstrate the importance of these considerations towards the improvement of system efficiency. Next, evaluation of relevant material properties via TGA is discussed in chapters 3 and 4. By incorporating such measurements into the thermodynamic reactor model of Chapter 2, the maximum efficiency possible with new OSM can be evaluated and high performance OSMs identified.

Oxygen Storage Materials

For two step thermochemical cycles, an intermediate OSM (such as a metal oxide, M_xO_y) is first reduced at high temperatures (T_H). This endothermic reaction is described in Eq. (1.4). The OSM is then cooled to a lower temperature (T_L), where it is re-oxidized when exposed to steam through the exothermic reaction in Eq. (1.5).

$$M_xO_y \rightarrow xM + \frac{y}{2}O_2 \tag{1.4}$$

$$xM + yH_2O \rightarrow M_xO_y + yH_2 \tag{1.5}$$

While the process described by Eq. (1.4) and (1.5) represents the complete reduction of an OSM to its pure metal phase (*M*) [41], this is not always the case. The oxide may only partially reduce to a nonstoichiometric state. The same is true for the oxidation step, resulting in a nonstoichiometric redox cycle (NRC) composed of reactions described below.

$$M_xO_{y-\delta_O} \rightarrow M_xO_{y-\delta_R} + \frac{\delta_R - \delta_O}{2} O_2 \tag{1.6}$$

$$M_xO_{y-\delta_R} + n_{H_2O}H_2O \rightarrow M_xO_{y-\delta_O} + (\delta_R - \delta_O)H_2 + \{n_{H_2O} - (\delta_R - \delta_O)\}H_2O \tag{1.7}$$

For the metal oxide, δ_R and δ_O represent the off-stoichiometric oxidation states achieved during the reduction and oxidation reactions respectively. Their difference is the hydrogen produced per cycle (n_{H_2}). Here, the units of $\delta_R - \delta_O$ can be taken as moles of hydrogen produced per mole of OSM per cycle. The OSM may be a pure or alloyed material undergoing partial reduction/oxidation, or an arbitrary number of compounds or solution phases that absorb and release oxygen through reversible reactions [42]. For Eq. (1.7), $\{n_{H_2O} - (\delta_R - \delta_O)\}H_2O$ is included to represent the partial conversion of H_2O to H_2, which will be discussed in detail in Chapter 2. Due to partial conversation of H_2O to H_2, which is limited by thermodynamics and kinetics of the oxidation reaction, a value of n_{H_2O} larger than δ_R-δ_O will likely be required to achieve the target δ_O needed for high conversion efficiencies. One of the principle advantages of NRCs is their potential for high cyclability with low OSM

degradation, because the OSM retain the same crystallographic phase throughout the cycle.

For each step of a NRC, the equilibrium δ can be found from: the thermochemical properties of the OSM, temperature, and oxygen partial pressure through Eq. (1.8) [43]. Here *ΔH(δ)* and *ΔS(δ)* are the enthalpy and entropy changes of the OSM associated with the loss of oxygen. The values of these enthalpy and entropy changes are generally functions of δ and for some materials also exhibit significant variation with temperature.

$$\Delta H(\delta) - T\Delta S(\delta) = -RT\ln\left(p_{O_2}\right) \tag{1.8}$$

By rearranging Eq.(1.8), Eq. (1.9) can be used to find $\Delta H(\delta)$ and $\Delta S(\delta)$ from an experimental values of δ as a function p_{O2} and temperature (shown later in Figure 2.2). Neglecting the temperature dependence, $-R\ln\left(p_{O_2}^{1/2}\right)$ can be plotted verses $1/T$ for constant values of δ and this data fit with a straight line. The slopes of these lines are ΔH and the y intercepts are $-\Delta S$ corresponding to specific values of δ.

$$\frac{\Delta H}{T} - \Delta S = -R\ln\left(p_{O_2}\right) \tag{1.9}$$

Recently, cerium dioxide (ceria, CeO_2) has received much attention in literature as an OSM for NRCs primarily due to is nonvolatile reduced state ($CeO_{2-\delta}$), fast oxidation kinetics, extended cycle durability, and its ability to support a large oxygen defect concentration in the fluorite phase (ceria's native stoichiometric crystal structure) [8, 29]. For reduced ceria, the oxygen off-stoichiometry is achieved

through the creation of oxygen vacancies in the OSM lattice rather than interstitial metal atoms. The reduction reaction described by this defect model can be described by doubly ionized oxygen vacancies, written below in Kroger-Vink notation[44]. This model can be validated by deriving the dependence of off-stoichiometry (δ) on oxygen partial pressure for small deviation from stoichiometry.

$$O_O^x + 2Ce_{Ce}^x \rightarrow V_O^{\cdot\cdot} + 2Ce_{Ce}^{'} + \frac{1}{2}O_2^{gas} \tag{1.10}$$

Here, O_O^x is an oxygen atom an oxygen lattice site, Ce_{Ce}^x is a cerium atom on a cerium lattice site, $V_O^{\cdot\cdot}$ is a doubly ionized oxygen vacancy, $Ce_{Ce}^{'}$ is a cerium atom on a cerium lattice site with a single localized electron, and O_2^{gas} is an oxygen gas dimer. The equilibrium constant for this reaction predicts the amounts of each species percent at thermodynamic equilibrium and is shown below.

$$K_{ws}^{KV} = \frac{\left(V_O^{\cdot\cdot}\right)\left(Ce_{Ce}^{"}\right)^2\left(p_{O_2}\right)^{1/2}}{\left(O_O^x\right)\left(Ce_{Ce}^x\right)^2} \tag{1.11}$$

For small deviation from stoichiometry, O_O^x and Ce_{Ce}^x reduce to one. Furthermore, through site and charge conservation, $V_O^{\cdot\cdot}$ and $Ce_{Ce}^{"}$ are equivalent δ and 2δ respectively. Therefore, the dependence of δ on p_{O2} can be derived (shown below).

$$\delta \propto p_{O_2}^{-1/6} \tag{1.12}$$

Instead, if ceria defects are models as singly ionized oxygen vacancies, then the reaction must be modified as shown below. Here, $V_O^{\cdot}$ represents the single ionized oxygen vacancy which for small deviations from stoichiometry is equal to δ. Again, $Ce_{Ce}^{'}$ is a cerium atom on a cerium lattice site with a single localized electron, but for this defect model, $Ce_{Ce}^{'}$ is equal to δ. The dependence of δ on p_{O2} can be again derived and is also shown below.

$$O_O^x + 2Ce_{Ce}^x \rightarrow V_O^{\cdot} + Ce_{Ce}^{'} + \tfrac{1}{2} O_2^{gas} \tag{1.13}$$

$$\delta \propto p_{O_2}^{-1/4} \tag{1.14}$$

These relations are graphically illustrated below on a map of ceria's off-stoichiometry versus p_{O_2}. In the following figure, the red line shows the slope of $\log(\delta) \propto -\tfrac{1}{6}\log(p_{O_2})$ and the blue line is $\log(\delta) \propto -\tfrac{1}{4}\log(p_{O_2})$. However, the observed dependence of δ on p_{O_2} agrees best with $\log(\delta) \propto -\tfrac{1}{5}\log(p_{O_2})$ which might imply some combination of singly and doubly ionized oxygen vacancies [44].

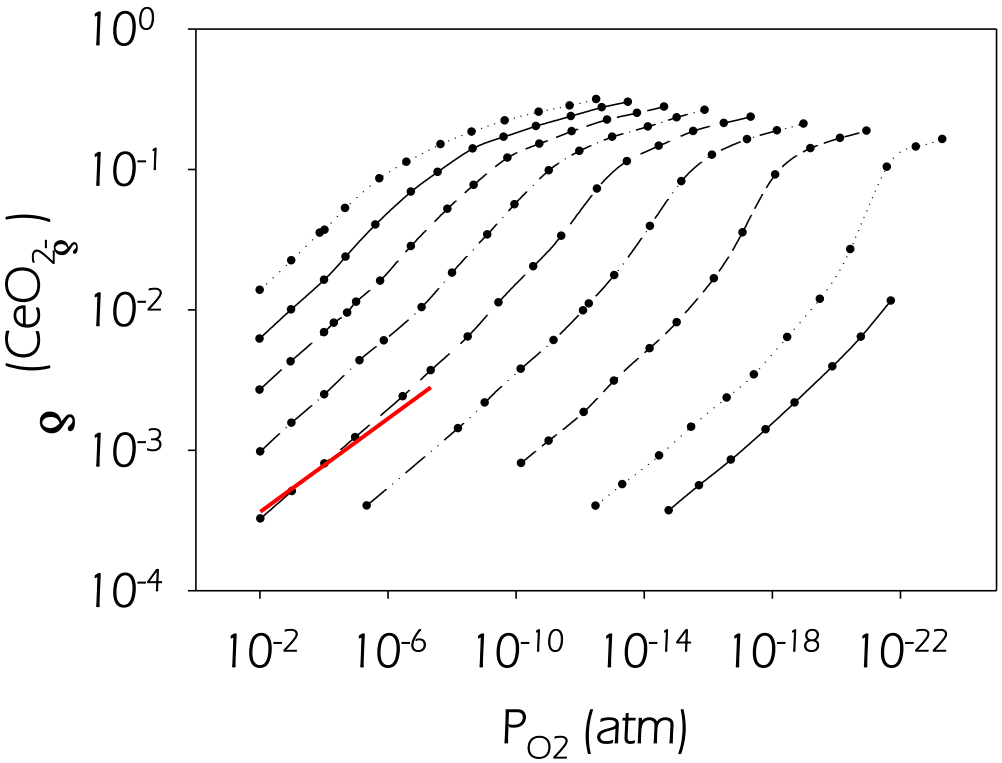

Figure 1.3: Isothermal δ versus p_{O2} for nonstoichiometric ceria from 750 °C and 800-1500°C in 100°C increments. Measurements by Panlener et al. [45] shown in black. The red trend line illustrates a log(δ) dependence of -1/6log(p_{O2}), and the blue trend line illustrates a log(δ) dependence of -1/4log(p_{O2}), and

For ceria with and without oxygen vacancies, $M_xO_{y-\delta_O}$ and $M_xO_{y-\delta_R}$ have the same metal sub lattice with varying amounts of vacancies on the oxygen sub lattice. Unlike other OSM's such as zinc oxide which reduces to volatile zinc vapor and oxygen gas, ceria experiences no structural phase change. This ability to avoid phase change is highly attractive for thermochemical hydrogen production because it eliminates the need to handle different materials during each reaction step enabling the OSM to be a monolith or to be supported on a substrate. Furthermore by avoiding phase transitions, kinetic limitations which result from the potential decrease in

oxygen mobility or increased activation barriers caused by the enthalpy of phase change are avoided. Other promising materials included transition metal perovskite oxides [46-48] and iron ferrites [49] which can achieve relatively high extents of reduction, thereby yielding more hydrogen per cycle than ceria. These materials will be discussed in further detail in Chapter 5. An idealized schematic of reactions (1.6) and (1.7) using ceria as the OSM is shown below.

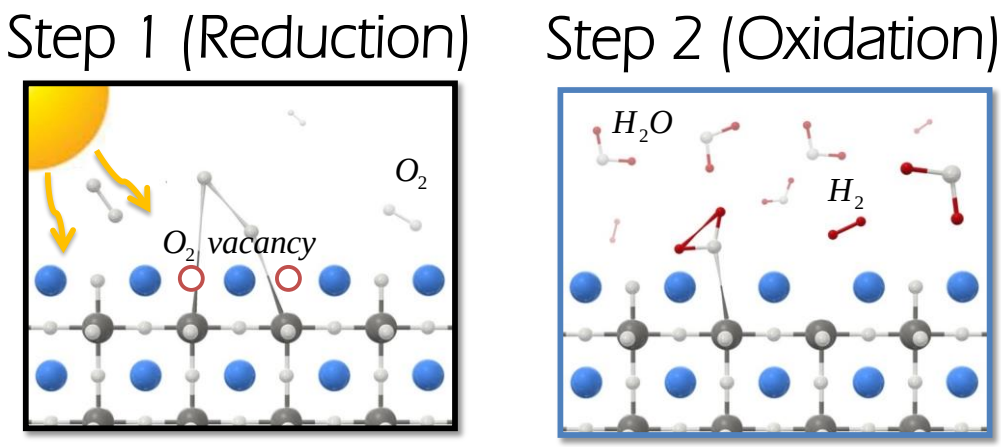

Figure 1.4: Idealized atomic schematic of each reaction of a two-step thermochemical cycle with ceria as the OSM. Step 1, reduction (left). Step 2, oxidation (right).

For step 1 of Figure 1.4, the ceria is first heated to a high temperature with concentrated solar power in a low oxygen pressure environment. Under these conditions, the OSM reduces, evolving oxygen gas and creating vacancies in the OSM lattice. In step 2, the temperature is reduced and the material is exposed to water vapor. Here, the OSM splits a portion of the water to re-oxidize producing hydrogen gas. While the values of ΔH and ΔS depend on the OSM used in the process, for all two-step cycles of interest, the maximum required temperature is less than that of

direct water thermolysis. If ceria is used as the OSM, variations of the standard state ΔH and $T\Delta S$ for Eqs. (1.6) and (1.7) are shown in below [50].

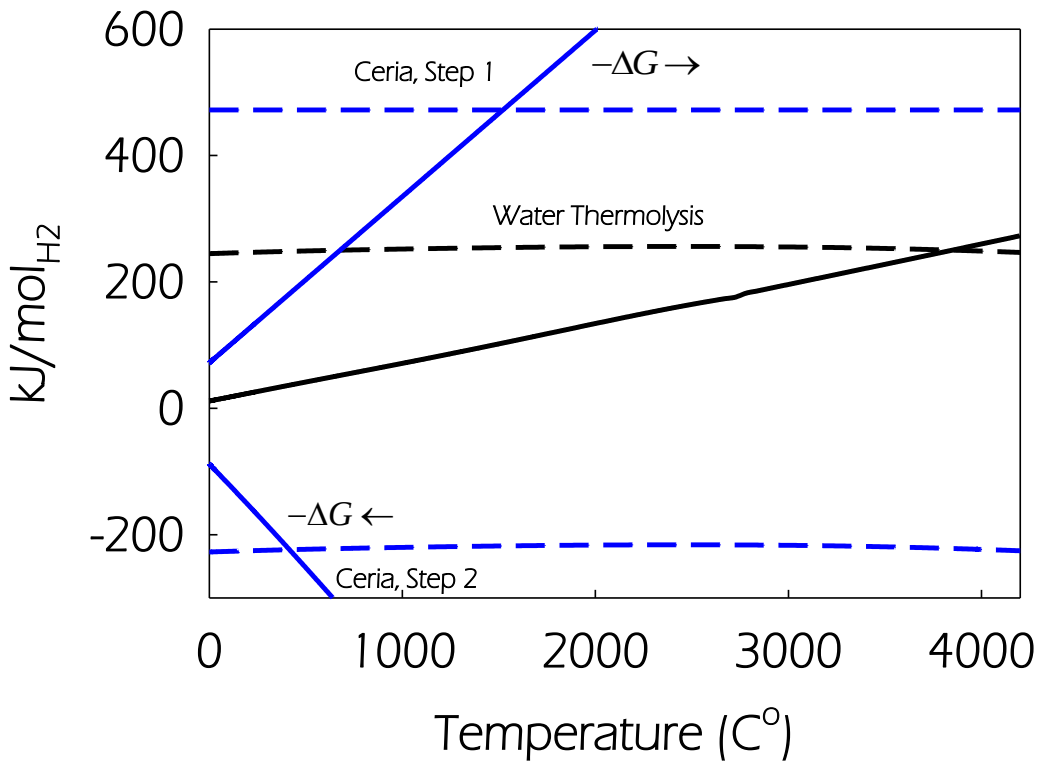

Figure 1.5: Change standard state enthalpy and entropy of water thermolysis and each reaction of a two-step thermochemical cycle where ceria is used as the OSM. Ceria is shown in blue and water thermolysis is shown in black. Standard that enthalpies are shown as solid lines and standard state entropy are shown as dotted lines.

Figure 1.5 shows how the value of ΔH for OSM reduction (step 1) is much larger than the enthalpy of water thermolysis (460 kJ/mol H_2), but because the solid oxygen of the OSM reacts to form diatomic oxygen gas, the value of ΔS is large relative to the reaction entropy of direct water thermolysis. Therefore, the temperature required for the value of ΔG to become negative is lower than the temperature needed to split water directly. These two step cycles can also split carbon dioxide to

generate CO by replacing the second step with the reaction described in Eq. (1.15). By simultaneously combining Eqs. (1.7) and (1.15), Furler et al. demonstrated the co-generation of H_2 and CO (syngas) [51].

$$M_xO_{y-\delta_R} + n_{C_2O}CO_2 \rightarrow M_xO_{y-\delta_O} + (\delta_R - \delta_O)CO + \left\{n_{CO_2} - (\delta_R - \delta_O)\right\}CO_2 \qquad (1.15)$$

CHAPTER 2

REACTOR CYCLE EFFICIENCY

As new OSMs are developed, it is important to establish a framework for evaluating the extent to which such materials can actually improve the system level NRC efficiency. In this chapter, a general framework is developed that, for the first time, allows for the optimization of NRC efficiency by simultaneous consideration of OSM properties and operating conditions of the thermochemical two-step redox cycle. Using ceria as the base-case OSM, we explore the potential improvement from employing alternative OSMs by highlighting two system energy inputs which previously have not been studied in detail. Furthermore, we demonstrate the importance of these considerations towards the improvement of system efficiency.

Reactor

A schematic illustration of a thermochemical two-step metal oxide redox cycle is shown in Figure 2.1 which demonstrates the relevant energy and mass balances. Here, an intermediate OSM, such as a metal oxide, is first reduced at a high temperature, T_H (via Reaction (1.6)). The OSM is then cooled to a lower temperature, T_L, where it re-oxidizes when exposed to steam (via Reaction (1.7)). In the indicated cycle, a vacuum pump is used to reduce the total pressure and oxygen partial pressure (p_{O2}) to enable the reduction of the OSM. The energy input to the system includes the work needed to drive the vacuum pump (W_{Pump}), the sensible heat needed to raise the temperature of the reactor from T_L to T_H (Q_{Reheat}), the energy needed to drive the endothermic reduction reaction (Q_{RXN}), and the sensible and latent heat associated

with generating steam (Q_{Water}) which serves as the reactant. Note that by carrying out heat recuperation, some portion of the sensible heat removed from the reactor (Q_{Out}) and some portion of the sensible heat removed from the product stream (H_2+H_2O) during step two can be recovered at an efficiency of ε_S and ε_G , respectively. During the time required to complete both steps of the reaction (Δt), heat is leaking from the system to the environment (Q_{Loss}).

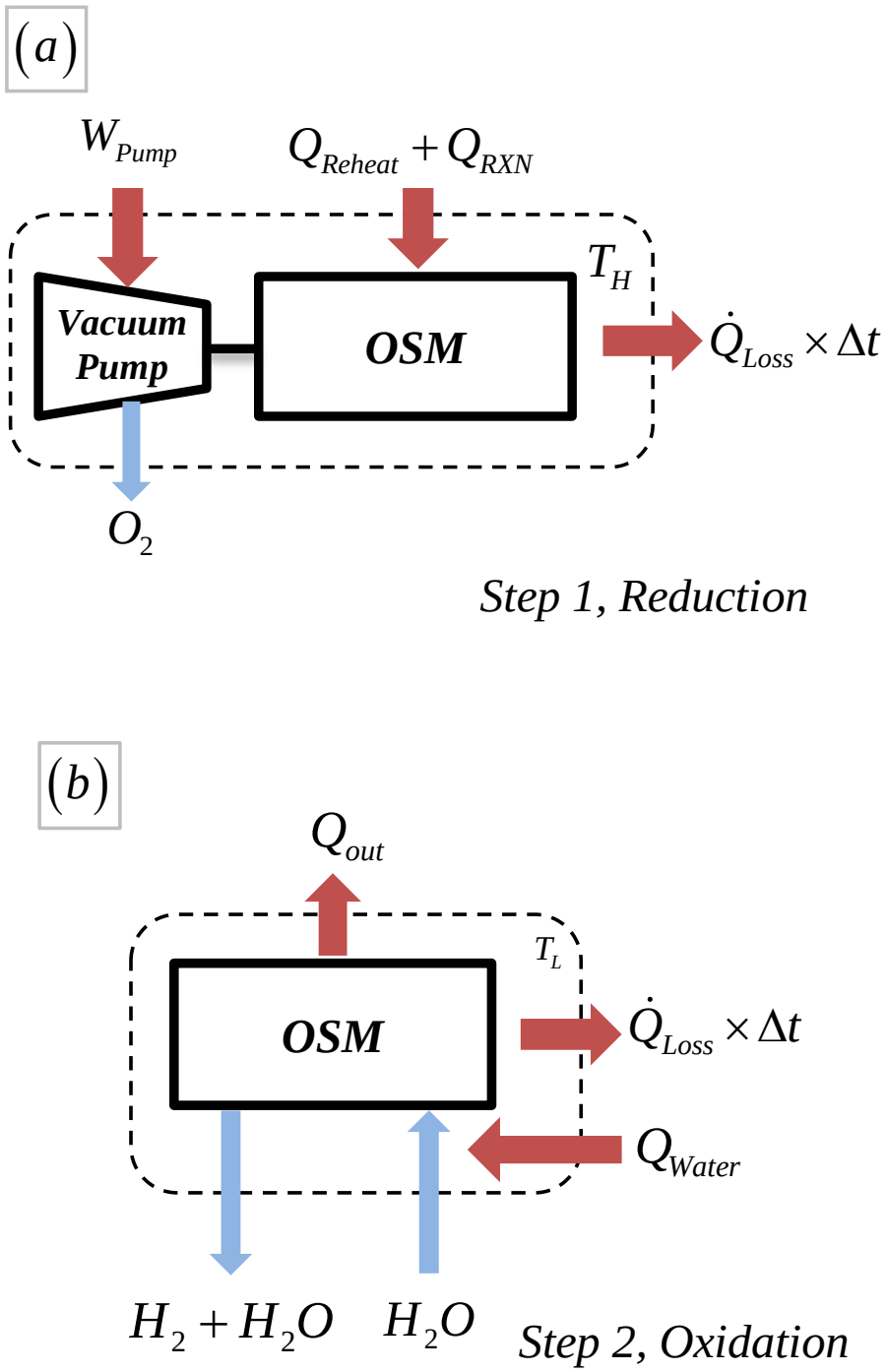

Figure 2.1: Schematic of energy and mass transfer in a two-step thermochemical redox reactor, (*a*) reduction, *(b)* oxidation. Q_{Reheat}, Q_{RXN}, and Q_{Out} refer to the sensible heat need to raise the OSM temperature, the heat needed to drive the endothermic reduction reaction, and heat that is removed upon cooling of the OSM, respectively. W_{Pump} is the work needed to drive the vacuum pump, and $\dot{Q}_{Loss} \times \Delta t$ is the heat that is assumed to leak from the system each reaction cycle.

Energy Factors Affecting NRC Efficiency

The generally accepted definition for thermochemical conversion efficiency (η) of a NRC is the ratio of energy stored chemically in hydrogen (defined by the higher heating value of, HHV_{H2}) to total energy input required to drive the process [13] which is given below

$$\eta = \frac{n_{H_2} \times HHV_{H_2}}{Q_{Total}} \tag{2.1}$$

where,

$$Q_{Total} = Q_{Reheat} + Q_{RXN} + Q_{Water} + W_{Pump} + Q_{Loss} \tag{2.2}$$

In Eq. (2.1) n_{H2} is the number moles of hydrogen produced per cycle (δ_R-δ_O), HHV_{H2} is the higher heating value of hydrogen, and Q_{Total} is the total energy input per cycle. Thermochemical reactors are inherently complex systems. Fluid mechanics, chemical reactions, and heat and mass transfer, as well as their coupling, must be considered in order to model the reactor efficiency. Additionally, the design space for the reactor parameters (such as T_H, T_L, p_{O2}, etc.) and the range of options for the OSM are large. Hence, it is difficult to develop a single all-encompassing model for efficiency and OSM performance. Furthermore, it is not possible to define a unified figure of merit to evaluate OSMs based only on material properties (without defining any system/reactor parameters). Reports on systems where the OSM is restricted to

ceria can be found by Lapp *et al.*[32], Siegel, *et al.* [15], and Ermanoski, *et al.* [35]. Parameters that affect efficiency included operational and design parameters such as heat recovery, the inert thermal mass of the reactor, T_H, T_L, as well as material parameters such as specific heat of the OSM (C_P^{OSM}), ΔH and ΔS of reduction, and the extent of oxidation (δ_O). The extent of reduction, δ_R, is determined from OSM material properties, T_H, and p_{O2} through equation (1.8). To better understand the complex relationship between these parameters and performance, it is convenient to express the efficiency in terms of dimensionless energy factors (Eq.(2.3)), where each factor represents a particular required energy input of the cycle (shown in Figure 2.1) normalized by the output energy stored chemically in hydrogen, as follows:

$$\eta = \frac{1}{F_{Reheat} + F_{RXN} + F_{Water} + F_{Pump} + F_{Loss}} \tag{2.3}$$

where, F_{Reheat}, F_{RXN}, F_{Water}, F_{Pump}, and F_{Loss} are the energy factors associated with heating the OSM, driving the endothermic reduction reaction, producing steam, driving the vacuum pump, and heat leaking from the system respectively. By evaluating the relative magnitudes of each factor, one can identify which energy inputs dominate, relative to the system output. The parameters that govern these dominant inputs can provide insight into potential directions for improvement. Later, the energy factors of Eq. (2.3) will be defined with Eqs (2.4)-(2.10).

A quasi-static two-step redox cycle is schematically illustrated by closed loop of solid lines in Figure 2.2. Although this path is not possible in an actual reactor, assuming such an idealized cycle allows an upper bound to be placed on system efficiency. In this figure, the isothermal reduction step (points 2→3) and the

isothermal oxidation step (points 4→1) are assumed to follow the equilibrium relationships between p_{O2}, T, and δ described by Eq.(1.8). The heating step (points 1→2) is conducted at a constant p_{O2} and is also assumed to follow the equilibrium relationship of Eq.(1.8). By assuming the cooling step (points 3→ 4) is conducted at a sufficiently rapid rate as to keep the nonstoichiometry (δ) of the OSM constant, the hydrogen produced per cycle is maximized. Therefore, these conditions determine the upper limit for NRC efficiency.

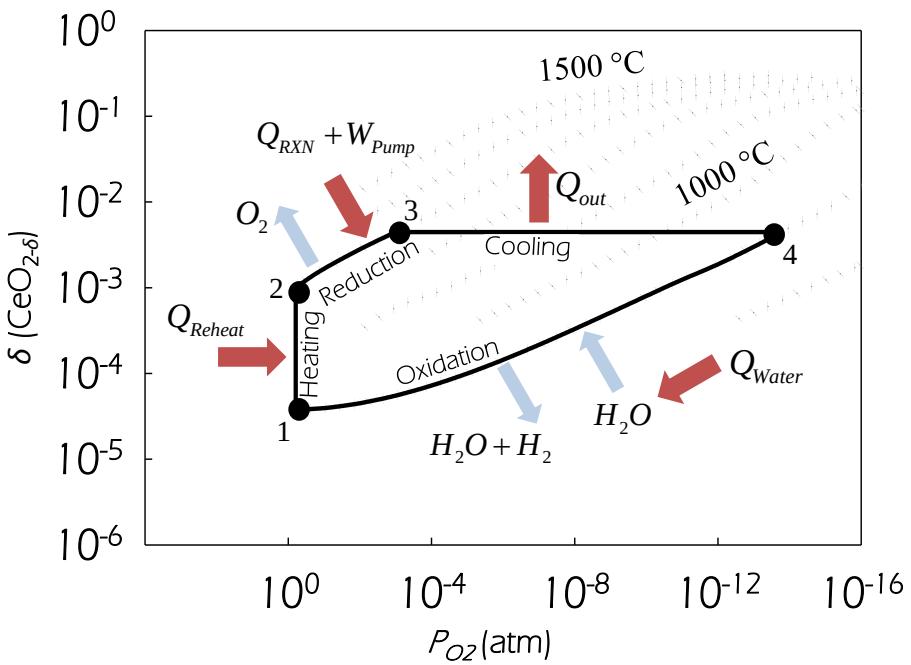

Figure 2.2: Equilibrium oxygen off-stoichiometry *(δ)* of ceria vs. $p_{O2.}$ Isotherms (dotted lines) are shown in 100°C incremented for temperatures in the range of in 800-1500°C[45]. An idealized oxygen off-stoichiometric cycle of the OSM for a two-step NRC is superimposed on this plot with solid lines (T_R=1300C, T_L=800C, p_{O2}=10^{-3} atm, and δ_O=0.0025). The OSM is headed from 800°C to 1300°C from points 1→2, reduced at 1300°C from points 2→3, cooled from 1300°C to 800°C from points 3 →4, and oxidized at 800°C from points 4→1.

Under these upper limiting assumptions, F_{Reheat}, which accounts for the sensible energy required to heat the OSM and inert reactor components from T_L to T_H (points 1→2), is modelled as follows:

$$F_{Reheat} = \frac{Q_{Reheat}}{n_{H_2} \times HHV_{H_2}} = \frac{(1-\varepsilon_S)(R_{TM}+1)\int_{T_L}^{T_H} C_P^{OSM} dT}{(\delta_R - \delta_O) \times HHV_{H_2}} \tag{2.4}$$

where ε_S is the fraction of solid phase heat that is recovered upon cooling (points 3→4), R_{TM} is the ratio of inert reactor thermal mass to OSM thermal mass, and C_P is the specific heat of the OSM.

F_{RXN}, which represents the energy required to liberate oxygen during the endothermic reduction reaction relative to the energy stored chemically in hydrogen (points 2→3), is modelled as:

$$F_{RXN} = \frac{Q_{RXN}}{n_{H_2} \times HHV_{H_2}} = \frac{\Delta H}{HHV_{H_2}} \tag{2.5}$$

F_{Water}, which accounts for the sensible heat needed to vaporize and preheat water used to oxidize the OSM (Figure 2.2, 4→1), is modelled as:

$$F_{Water} = \frac{Q_{Water}}{n_{H_2} \times HHV_{H_2}} = \frac{(1-\varepsilon_G)\left\{n_{H_2O}\int_{T^o}^{T_L} C_P^{H_2O} dT - \left(\Delta H - LHV_{H_2}\right)\right\}}{(\delta_R - \delta_O) \times HHV_{H_2}} \tag{2.6}$$

where ε_G is the fraction of gas phase heat that is recovered, C_P is the specific heat of water, and T^o is the ambient temperature of the reactants fed into the system. Here, the difference between ΔH and the lower heating value of H_2 (LHV_{H2}) accounts for the exothermic energy released during oxidation with steam that can be utilized to preheat water. The exothermic energy released when the OSM is oxidized with steam

(ΔH^{Steam}) is determined by the change in enthalpy of reaction (1.7), shown below as the enthalpy of the products minus the enthalpy of the reactants.

$$\Delta H^{Steam} = \left\{ h^{s}_{M_xO_{y-\delta_O}} + \left(\delta_R - \delta_O\right) h^{g}_{H_2} \right\} - \left\{ h^{s}_{M_xO_{y-\delta_R}} + \left(\delta_R - \delta_O\right) h^{g}_{H_2O} \right\} \tag{2.7}$$

By adding the enthalpy of the diatomic oxygen to the reactants and subtracting oxygen's enthalpy from the products (which is possibly zero depending on your reference state), Eq. (2.7) simplifies to the difference in the OSM reduction enthalpy and the lower heating value of water which is shown below, multiplied by a stoichiometric constant.

$$\begin{aligned} \Delta H^{Steam} &= \left(h^{s}_{M_xO_{y-\delta_O}} - h^{s}_{M_xO_{y-\delta_R}} - \frac{\left(\delta_R - \delta_O\right)}{2} h^{g}_{O_2} \right) + \left(\delta_R - \delta_O\right) \left\{ h^{g}_{H_2} + \tfrac{1}{2} h^{g}_{O_2} - h^{g}_{H_2O} \right\} \\ &= \left(\delta_R - \delta_O\right) \left\{ \Delta H - LHV_{H_2} \right\} \end{aligned} \tag{2.8}$$

Here, the right side the Eq. (2.8) is represented by LHV_{H2} rather than HHV_{H2} because the reaction proceeds isothermally, and the water has already been vaporized and preheated to the oxidation temperature. Because the enthalpy of vaporization is accounted for by preheating, LHV_{H2} must be used which is the enthalpy of stored chemically in water excluding of phase change. If ΔH^{Steam} is greater than or equal to the energetic expense of heating water, then the excess exothermic energy is rejected from the system (wasted) and F_{Water} becomes zero.

F_{Pump}, which accounts for the energy required to produce the low p_{O2} atmosphere during reduction (2→3), is modelled as:

$$F_{Pump} = \frac{W_{Pump}}{n_{H_2} \times HHV_{H_2}} = \frac{W_{Pump}}{(\delta_R - \delta_O) \times HHV_{H_2}} \tag{2.9}$$

For OSMs and reduction temperatures that require a p_{O2} less than 0.21 atm, W_{Pump} is the work required to reduce the pressure to p_{O2}.

Finally, F_{Loss}, which accounts for the heat leakage in the system (where Δt is the time required to complete one reaction cycle), is expressed as:

$$F_{Loss} = \frac{Q_{Loss}}{n_{H_2} \times HHV_{H_2}} = \frac{(\dot{Q}_{Loss}) \times \Delta t}{(\delta_R - \delta_O) \times HHV_{H_2}} \tag{2.10}$$

As defined here, the thermochemical conversion efficiency (η) only describes the reactor's ability to convert thermal energy to chemical energy; that is, losses associated with converting sunlight to thermal energy are ignored. Therefore in Eq. (2.10) $\dot{Q}_{Loss}$ represents the heat leakage from the reactor and does not include heat losses associated with converting sunlight to heat (e.g. such as re-radiation losses, which are known to limit the performance of current systems [30]).

Operational Considerations

Prior Work on Reactor Optimization

The high theoretical efficiencies reported for NRC's [15, 32, 35, 52] have yet to be realized in experimental reactors [29, 33]. In previous experimental reactors, T_H was achieved by heating via direct solar irradiation. Keene, *et al*. [30] showed that low efficiencies observed in such systems are primarily caused by massive heat losses associated with re-radiation ($\dot{Q}_{Re\text{-}rad}$). However, it is important to recognize that for the reactor itself, F_{Loss} is the only energy factor which is proportional to cycle time.

Therefore minimization of heat losses and increasing power density are the only motivations for lowering Δt, (i.e. fast thermal cycling and reaction kinetics). Noting that increasing power density is of high practical importance due to economic consideration but outside of the scope of this work, all other energy factors are essentially time independent.

Ermanoski, *et al*. [35] reported on a moving packed bed reactor concept that decoupled the fuel production rate from the incoming solar flux. This design allowed the fuel production rate to be tuned, minimizing F_{Loss}. Furthermore, Lapp, *et al*. [53] reported on a counter-rotating reactor with a value of ε_S that is larger than 50% for temperature swings greater than 400°C.

While reactor designs are improving and re-radiation losses are decreasing, the optimization of thermochemical conversion efficiency remains an important issue that has been extensively studied [15, 32, 35, 36, 53]. For these studies, the reactor, operating conditions, and modelling methods vary. Nonetheless, there have been three primary pathways identified for future improvement. First, due to the large thermal load required to swing the OSM temperature from T_L to T_H, under optimum operation conditions F_{Reheat} is typically the largest energy factor. Because the energy used to heat the OSM is sensible heat that must be removed from the OSM during cooling, recovering and utilizing this sensible heat is critical to high performance. This implies that the best reactor merely serves as an effective heat exchanger that achieves the conditions required to make each reaction thermodynamically favorable with minimal losses. The effectiveness of a cross flow heat exchanger is defined below [54]:

$$\varepsilon = \frac{C_C\left(T_{c,i} - T_{c,o}\right)}{C_{\min}\left(T_{h,i} - T_{c,i}\right)} \tag{2.11}$$

where, C_C is the specific heat of cold fluid, Tc is the inlet and outlet temperature of the cold fluid, C_{min} is the minimum specific heat of both fluids, and $T_{h,i}$ is the hot fluid's inlet temperature. This definition also applies to solid phase heat recovery. However for solid phase heat exchange, the materials which exchange heat are not flowing through the tubes of a heat exchanger, and the mechanical mechanism used to facilitate this heat transfer is more sophisticated. A typical approach for solid phase heat recovery includes exchanging heat between two different OSM masses (one OSM which has been reduced at T_H and needs to be cooled to T_L and another OSM which has been oxidized at T_L and needs to be heated to T_H [35]). Another approach incorporates counter rotating rings, one made of the OSM and the other of an inert ceramic material. Here, the heat is stored in the inert material and then used to assist reheating the OSM during the next reaction cycle [55]. In either case, Eq. (2.11) defines the efficiency of solid phase heat exchange where the denominator represents the amount of heat which is removed from the OSM upon cooling from T_H to T_L and the numerator is the faction of this removed heat which is delivered to the OSM during reheating from T_L to T_H. Assuming the specific heats of reduced and stoichiometric OSM equivalent, if all the heat removed from the OSM during step 2 is used to reheat the OSM during step 1, no extra sensible heat is required to reach T_H, and ε (or ε_S) equals one (F_{Reheat} is zero). Hence, increased performance could come from reactors with better heat recovery.

The second pathway to high efficiencies focuses on the OSM. In the limit of a perfect reactor (ε_s=1, ε_G=1, and W_{Pump} and Q_{Loss} are negligible), the maximum theoretical efficiency is the inverse of F_{RXN} (discussed further later in this chapter and in Chapter 3). Decreasing ΔH therefore decreases this energy factor, which serves as a fundamental limiting efficiency for the material itself. Furthermore, as ΔH decreases, the OSM can achieve deeper reductions and δ_R increases. With δ_O fixed, larger δ_R reduces all other energy factors (except F_{RXN}). Thus, the discovery of a new OSM with a lower value of ΔH could improve cycle efficiency.

Third, as the energy required to drive a vacuum has been shown to be small relative to the energy stored chemically in hydrogen, operating reactors at the lowest possible pressure will also achieve deeper extents of reduction, increasing δ_R which should result in high efficiencies [35].

Importance of OSM Reduction Enthalpy Change and the Extent of Chemical Conversion

The extent of chemical conversion describes the fraction of a reactant that is converted into reaction products. This important quantity is of interest because it determines the thermal load required to preheat the water used during oxidation (n_{H2O}) from T^o to T_L. We define the extent chemical conversion of steam during OSM oxidation of a step two NRC as follows:

$$C_{H_2O} = 1 - \frac{n_{H_2O} - (\delta_R - \delta_O)}{n_{H_2O}} = \frac{n_{H_2}}{n_{H_2O}} \tag{2.12}$$

The ratio of unreacted steam to hydrogen in the product stream of the oxidation reaction, R_{H2O}, is the defined as,

$$R_{H_2O} = \frac{1}{C_{H_2O}} - 1 \tag{2.13}$$

Generally, increasing C_{H2O} lowers F_{water} and increases efficiency. An upper limit for C_{H2O} and therefore efficiency can be established by neglecting reaction kinetics. With this assumption, the maximum instantaneous conversion can be found from the equilibrium effective p_{O2} established by R_{H2O} at a given value of δ (Figure 2.2 and Eq. (1.8)). With the effective p_{O2}, the R_{H2O} at the reactor outlet can be found with the following equation,

$$K_{WS}(T) = p_{O_2}^{1/2} \Big/ R_{H_2O} = \frac{1}{C_{H_2O}} - 1 \tag{2.14}$$

where K_{WS} is the equilibrium reaction constant for $H_2O \rightarrow H_2 + 1/2O_2$. Combining Eq. (1.8) and (2.14), C_{H2O} can be written as a function of temperature, ΔH, and ΔS as follows:

$$C_{H_2O} = \frac{K_{ws}(T)}{\left(\exp\left(\frac{-(\Delta H(\delta) - T\Delta S(\delta))}{RT}\right)\right)^{1/2} + K_{ws}(T)} \tag{2.15}$$

This expression is plotted in Figure 2.3 for different values of $R_{\Delta H}$, where $R_{\Delta H}$ defines the ratio of the OSM ΔH of reduction to LHV_{H2}. Figure 2.3 was created using the value of ΔS corresponding to ceria at δ=0.005. As the value of ΔH is reduced at constant oxidation temperature, C_{H2O} also decreases and the hydrogen concentration

in the product stream consequently decreases. Thus for low values of ΔH and high T_L, a large amount of unreacted water is required to drive the OSM oxidation (step 2). Figure 2.3 also shows how low conversion can be combatted by lowering the oxidation temperature; meaning, lower oxidation temperatures are required for materials with low values of ΔH.

The inverse of C_{H2O} represents the moles of water required for oxidation per mole of H_2. The water required for oxidation can be evaluated from Eq. (2.16) and can be substituted into Eq. (2.6) to evaluate F_{Water}.

$$n_{H_2O} = \int_{\delta_O}^{\delta_R} 1 \Big/ C_{H_2O} \, d\delta \tag{2.16}$$

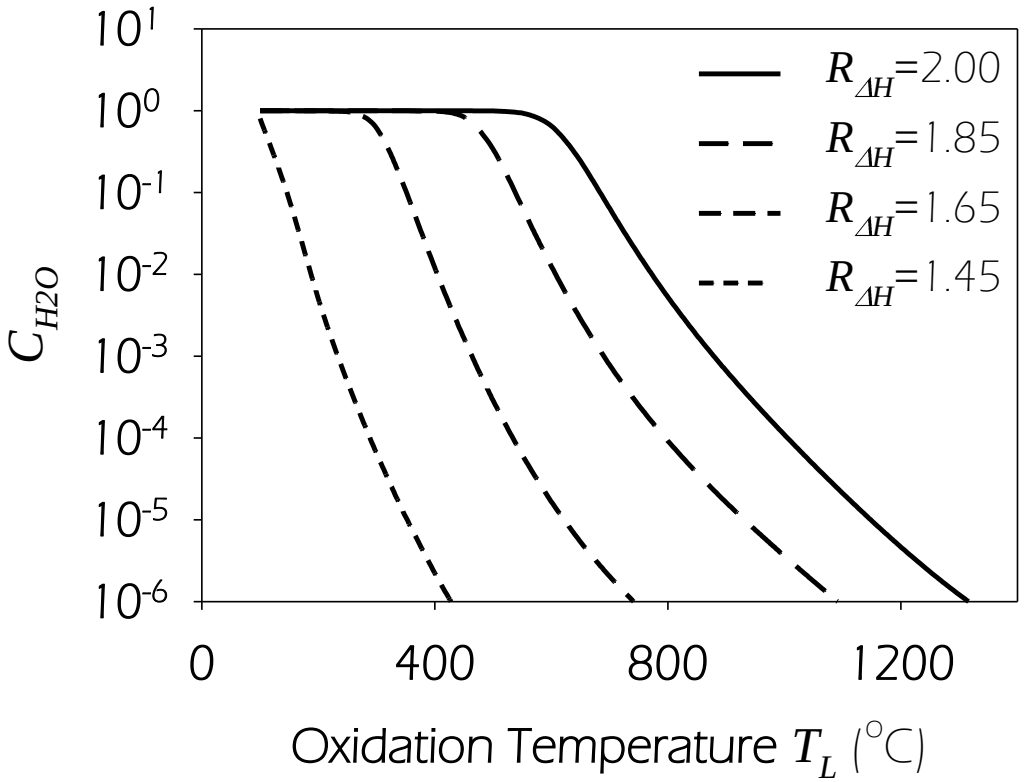

Figure 2.3: Fraction of water conversion as defined by Eq. (2.15) with ΔS=316 J/K-mol H_2 (Here, ΔS is assumed to be that of ceria at δ=0.005 [45]). For ceria with δ=0.005, $R_{\Delta H} \approx 2.0$.

The experimental equilibrium off-stoichiometry of ceria is shown as a function of p_{O2} and T in Figure 2.2 [45]. This OSM approaches complete oxidation even at very low values of p_{O2}, implying that ceria has very high C_{H2O} over the course of oxidation. This high C_{H2O} is due to the relativity high large of ΔH of ceria, which is nearly twice the enthalpy change required for water dissociation [28]. With T_L held constant, reducing ΔH decreases C_{H2O} and increases F_{Water}. Thus there is a trade-off

associated with smaller values of ΔH, as lowering ΔH decreases F_{RXN} and increases δ_R, it also increases F_{Water} and/or F_{Reheat}.

Although the relationship between the ΔH and efficiency is complicated, there are upper and lower limits to the values of ΔH desirable for a NRC. If $R_{\Delta H}$ is less than 1, then the oxidation shown in reaction (1.7) will be endothermic and the OSM is not likely to have the thermodynamic potential to overcome the entropy decrease during OSM oxidation with steam (step 2). On the other hand, if $R_{\Delta H}$ is too large, then the T_H will be prohibitively high and/or the p_{O2} will be prohibitively low for significant fuel production. For the ensuing discussion, we have assumed the δ and T dependence of the value of ΔH to be that of ceria, to simplify our analysis. However, it should be noted, that if the dependence for another OSM is different, then the major qualitative conclusions from the subsequent analysis are likely to be unchanged.

Meredig, *et al*. [42] mapped ranges for the value of ΔH and ΔS that are viable for thermochemical water splitting by evaluating the ability for water to oxidize a reduced OSM from a thermodynamic perspective. Miller, *et al*. [56] reviewed the many factors affecting OSM design including, but not limited to, OSM thermodynamic properties. The authors noted that a maximum theoretical efficiency is achieved at the lowest limit on the value of ΔH (i.e. the enthalpy of water dissociation). However, because calculations of theoretical efficiency ignore the losses from low C_{H2O} this conclusion may not translate to real reactors.

For some OSMs with high values of C_{H2O} (ceria), very little unreacted water flows through the reactor and, therefore, the losses from preheating excess water are negligible. Detailed system efficiency analyses of NRCs using ceria as the OSM have

either neglected these losses ($n_{H2O}=\delta_R-\delta_O$) [32] or assumed that the losses are fixed and small (3%) [15], which are both valid and good assumptions for ceria. However, when modelling cycles which use new materials with lower values of ΔH [46, 48, 49], the lower value of C_{H2O} could require larger amounts of unreacted water ($n_{H2O}-(\delta_R-\delta_{OX})$), increasing the energy penalty associated with preheating this excess water (F_{Water}). The goal of the new model presented herein is to develop a framework that can be used to evaluate the efficiencies achievable by different OSMs, while accounting for the coupling between reactor design, operational parameters, and OSM properties. Such considerations allow for enhanced optimization of the highly coupled system parameters outlined above.

The Influence of Pump Efficiency

The value of p_{O2} for reaction (1.6) (OSM reduction, step 1) is commonly lowered to increase the thermodynamic driving force for reduction. Doing so increases δ_R with the aim of achieving higher efficiencies. One method of decreasing the p_{O2} utilizes an inert sweep gas such as nitrogen or argon and this approach has been studied in detail [29, 31, 32, 57]. Ermanoski et al. calculated thermochemical conversion efficiency possible at different values of p_{O2} during step 1 using an inert sweep gas. Their results are shown below [35].

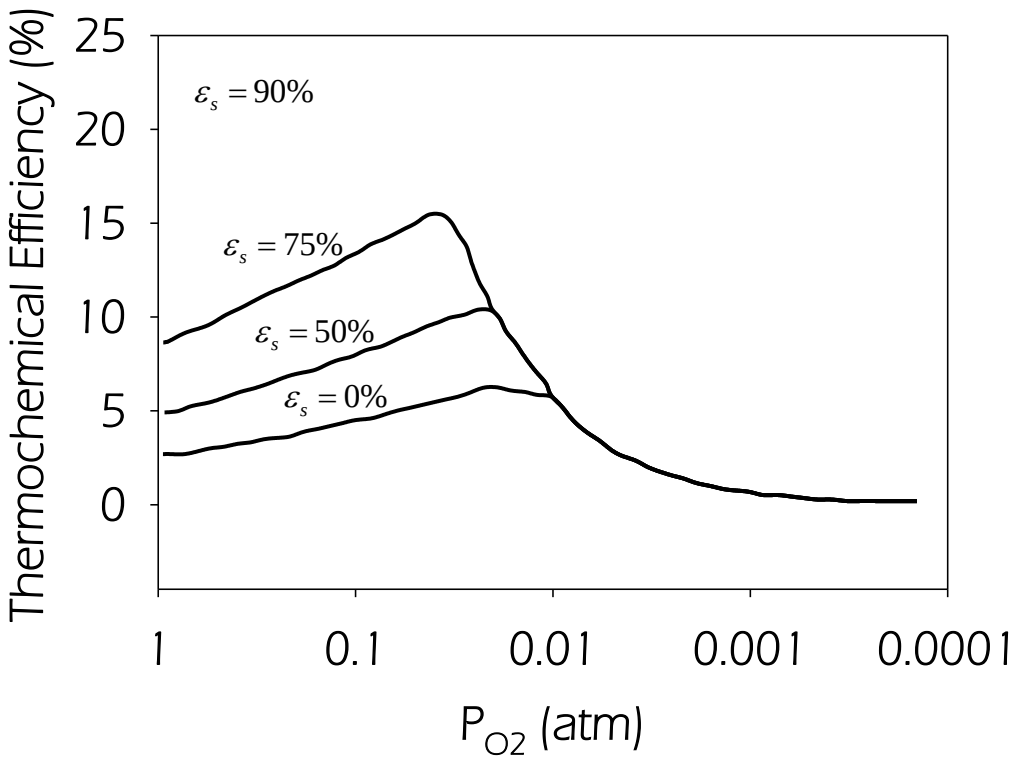

Figure 2.4: Thermochemical conversion efficiencies (η) vs. the oxygen partial pressure (p_{o2}) when an inert sweep gas is used during reduction (step 1) [35]. Efficiency is shown for different values of solid phase heat recovery (εs).

By accounting for the energetic penalty of producing the inert sweep gas (20 kJ/mol [58]), Figure 2.4 shows how efficiency trends to zero for very low values of p_{O2} because the amount of inert sweep gas require to further reduce the oxygen partial pressure increases as the p_{O2} decreases. Therefore, when operating at lower values of p_{O2} the amount of inert sweep gas require is too energetically expensive to achieve high conversion efficiencies. Therefore, a vacuum pump has been highlighted as a more promising means of achieving higher conversion efficiencies with lower values of p_{O2} [15, 35]. As a result, attention has shifted to using mechanical vacuum pumping

to achieve low pressures, and it has even prompted analysis and testing of isothermal cycles[38, 59].

The minimum possible work required to produce a vacuum can be derived by assuming negligible heat transfer and isothermal compression. The result of this derivation (found in the appendix) is shown below.

$$W_{Pump} = \int_{\delta_O}^{\delta_R} \frac{n_{O_2}(\delta)}{\eta_{Pump}\left(P(\delta,T)\right)} RT^o \ln\left(\frac{P^O}{p_{O_2}(\delta,T)}\right) d\delta \tag{2.17}$$

where η_{Pump} is the efficiency of the mechanical vacuum pump, n_{O2} is the number of moles of oxygen lost by the OSM during reduction, R is the gas constant, T^o is the pump temperature, P^o is the reference pressure on the high pressure side of the vacuum pump, and p_{O2} is the oxygen partial pressure during reduction. This expression differs slightly from previous models which assumed that all of the oxygen (n_{O2}) was removed at a constant value of p_{O2} equal to the final reduction pressure [15, 35]. Eq. (2.17) accounts for the oxygen gas that evolves during the transient reduction of reactor pressure. Here, n_{O2} is a function of δ and is defined by:

$$n_{O_2} = \frac{\left(\delta_R - \delta_O\right)}{2} \tag{2.18}$$

Where Eq. (2.18) converts the number of oxygen atoms leaving the solid OSM lattice to gaseous oxygen dimers. The factor of two accounts for the two oxygen atom required to create each oxygen gas molecule (O_2).

Neglecting pump efficiency, W_{Pump} as defined by Eq. (2.17) is always smaller than W_{Pump} as defined in previous expressions where P is held constant at the final p_{O2} [15, 35] (shown later in Eq. (2.19)). Ermonoski, *et al*. [35] report a monotonic

relationship between the final value of p_{O2} after reduction and reactor efficiency [35], but suggest a lower limit of p_{O2} between 10^{-3}-10^{-4} atm for reactors ranging from 10^{2}-10^{3} kW. This limit results from the hardware requirements of pumping large volumes of low density gas. In previous analyses, the efficiency of the pump is either neglected or assumed to be on the order of 10% and constant. Other methods of reducing the p_{O2} could also be used (e.g., electrochemical pumps), however, if mechanical vacuum pumps are used (similar to those used in the silicon manufacturing industry), then an estimation of the pump efficiency is straightforward (provided that pump performance data is available).

Different pumping technologies may be required, depending on the desired operating pressures. For pressures of 10^{-4}-10^{-6} atm, displacement pumps are most commonly used. For lower pressures, a displacement pump is often used to lower the pressure to approximately 10^{-4} followed by the use of another pump to reach the final vacuum pressure (e.g., a magnetically levitated turbo pump or a diffusion pump). The efficiency of these pumps can be defined as the ideal pump work over the actual electrical power consumption as follows:

$$W_{Pump}^{Ideal} = n_{O_2} R T^{o} \ln\left(\frac{P^{O}}{P}\right) \tag{2.19}$$

$$\eta_{Pump} = \frac{W_{Pump}^{Ideal}}{W_{Electrical}} = \frac{W_{Pump}^{Ideal}}{W_{Pump}^{Ideal} + W_{Friction}} \tag{2.20}$$

where $W_{Friction}$ is the work lost to internal friction.

Figure 2.5 shows the efficiency of two commercially-available pumps operating at different vacuum levels. As can be seen in this figure, vacuum pump

performance becomes extremely poor at pressures less than 10^{-3} atm. This poor performance can be explained by modelling the pump efficiency using Eq. (2.20), which is justified by the following rationale. As the pressure decreases, the gas density decreases and the number of gas molecules removed by the pump for each impeller rotation decreases (n_{O2}). However, the work lost to a small amount of internal friction remains essentially constant as pressure drops. Using the frictional loss as a fitting parameter, Eq. (2.20) was fit to the performance data and exhibits excellent agreement confirming the validity of the aforementioned explanation (Figure 2.5). Although these pumps have not been optimized specifically for thermochemical reactors, the efficiency trend shown in Fig. 4 is not likely to change dramatically and therefore, order of magnitude efficiency improvements are unlikely. With the aim of accurately predicting the energy required to achieve low values of p_{O2}, the functional dependence of the pump efficiency shown in Figure 2.5 was incorporated into Eq. (2.17) to calculate F_{Pump} in the ensuing analysis.

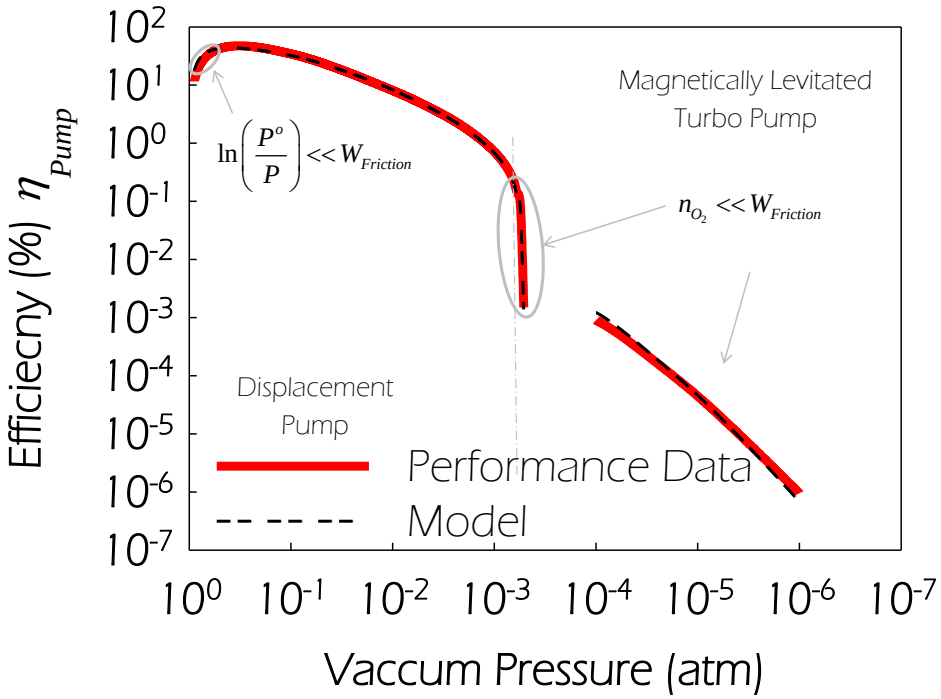

Figure 2.5: Efficiency of two example pumps used to achieve medium and low pressures. Preformance data was acquired from Becker Pumps Corp. and Turbo Vacuum Pumps for the displacement and turbo pump respectively.

An Efficiency Model That Links Material Properties and Operational Parameters

For the model of thermochemical conversion efficiency described in equations (2.3) - (2.17), the following parameters determine the NRC efficiency:

$$\eta = \eta(\dot{Q}_{Leak}, \Delta t, T_H, \varepsilon_G, \varepsilon_S, R_{TM}, \Delta H(\delta), \Delta S(\delta), C_P^{OSM}, T_L, P_{O_2}, \delta_O) \tag{2.21}$$

where $\dot{Q}_{Leak}$ is the heat losses rate from the reactor, which is proportional to the reactor's surface area. These losses can be mitigated through reactor design and by

minimizing cycle time (Δt). While the kinetics of the OSM oxidation and reduction reactions can determine cycle time, other considerations may also limit the rate at which the reactor can be cycled. Such factors include: the time required to reach the desired value of p_{O2} and the time required to change the OSM temperature from T_H to T_L (which can be bounded by thermal shock or heat and mass transport limitations). If temperature swings of more than a few hundred degrees are required, then avoidance of excessive thermal shock may set a lower bound on the value of Δt on the order of minutes. Since current reactors have exhibited cycle times on the order of tens of minutes, it seems unlikely that more than one order of magnitude decrease in cycle time can be realized without sacrificing long reactor life. In the subsequent analysis, $\dot{Q}_{Leak}$ is set to zero and F_{Leak} is excluded for simplicity. As a result, the remaining efficiency parameters can be grouped into three important and distinctive categories: *reactor parameters*, *OSM properties*, and *operational parameters*.

The *reactor parameters* include T_H, ε_G, ε_S, and $1/R_{TM}$. These parameters are typically determined by reactor design and are important to distinguish because they exhibit a monotonically increasing influence on the thermochemical conversion efficiency. Thus, an optimal reactor simply has maximum possible values for all *reactor parameters*, as limited by materials, cost or other feasibility issues. This relationship suggests that all reactors should strive to maximize T_H, ε_G and ε_S, and minimize R_{TM}. While T_H can be as high as 1500°C for ceria and could be lower for improved OSMs, it should be noted that the upper limit of T_H can be bounded by OSM stability. ε_G and ε_S can vary from zero to one and R_{TM} can vary between zero and infinite.

OSM properties include ΔH, ΔS, and C_P^{OSM}. These parameters are not as freely chosen as *operational parameters*. In theory, the values of ΔH and ΔS could be optimized and C_P^{OSM} minimized to increase η. While the tuning of ΔS and C_P^{OSM} have not received extensive attention, previous studies have shown that the value of ΔH can be systematically tuned for certain materials [43, 48, 60-67]. ΔH is therefore one of the most promising *OSM properties* to explore with regards to improving reactor performance in the immediate future. The range of ΔH applicable for NRC has been previously discussed. However, the value of ΔS varies little relative to ΔH because the value of ΔS is mostly dominated by the entropy of oxygen generation and the contribution to ΔS from the solid phase entropy change are small by comparison.

Finally, *operational parameters*, unlike *reactor parameters*, do not have monotonic relation to η and are expected to have optimal values. For a given set of *reactor parameters* and *OSM properties*, the *operational parameters* (p_{O2}, T_L, and δ_O) should be selected to maximize efficiency. For example, lowering p_{O2} increases δ_R and the hydrogen produced per cycle, but it also requires escalating amounts of pump work due to low η_{Pump} at low pressures. p_{O2} can range from 0.21 (oxygen in air) to very small values (e.g. 10^{-10}). Reducing δ_O increases the hydrogen production per cycle but also increases the water required for oxidation because C_{H2O} typically decreases as an OSM nears completion oxidation. δ_O can range from δ_R to zero when the OSM is oxidized completely. Reducing T_L increases the thermal load of reheating the reactor and the OSM, but it can also decrease δ_O (producing more hydrogen per cycle) or decrease the amount of water required for oxidation. T_L in theory range from

0 K to T_H, but the optimum value and range of each *operational parameter* will be discussed in detail later.

For a given OSM, these relationships define a 4-D design space $\eta(p_{O2}, T_L, \delta_O)$ which can be optimized for maximum system efficiency through parametric study. Realistic ranges and typical values of each of these parameters is given in the Table below to indicate the accessible range for the value.

Table 2.1: Maximum, minimum, and typical values for all reactor parameters, operational parameters, and OSM properties.

	Minimum	Maximum	Typical for Ceria
T_H	100°C	2400°C	1500°C
ε_G	0	1	0.95
ε_G	0	1	0.5
R_{TM}	0	∞	0
ΔH	241 kJ/mol H_2	480 kJ/mol H_2	480 kJ/mol H_2 [28]
ΔS	220 kJ/K-mol H_2	330 J/K-mol H_2	260 J/K-mol H_2 [28]
C_P^{OSM}	0.12 kJ/kg-K	3.6 kJ/kg-K	.44 kJ/kg-K [28]
p_{O2}	1.00E-10	0.21	1.00E-03 {This Work]
T_L	100°C	2400°C	900°C {This Work]
δ_O	0	2	0.0015 {This Work]

Heat Exchangers

Mechanisms for solid phase heat exchange have been previously discussed earlier this chapter [35], and improvements could significantly impact reactor performance. Additionally, to reduce the energy load of preheating the water needed for oxidation, gas phase heat exchange can be used to recover sensible heat from the oxygen and hydrogen/water products of reaction steps one and two respectively. In a typical fluid heat exchanger, hot and cold fluids enter the heat exchanger at the inlets and flow past a solid wall that prevents chemical interaction/mixing between the two

streams. Furthermore, this wall facilitates the exchange of sensible and/or latent heat. The effectiveness of a heat exchanger (ε) is directly related to the contact area, solid wall thermal conductivity and the convection coefficients of the fluids that exchange heat. Contact area is a function of the size and determines the capital cost of the heat exchanger. The convection coefficient, while a function of many parameters, is strongly dependent on the density of the fluid. The heat exchanger needed to recover a significant portion of the sensible heat of the oxygen produced in reaction step 1 will likely be limited by the low convection coefficient on the low pressure side (at a pressure of p_{O2}), and therefore this heat exchanger is likely to be large in sized (e.g., of low power density). Additionally, the efficiency impact of recovering heat from the oxygen gas is minor due to the relatively small sensible heat carried by the oxygen gas stream [35, 53]. Therefore, the recovery of the oxygen's sensible heat is neglected from this analysis. Recovering the sensible heat of the water-hydrogen mixture produced in step two (OSM oxidation), on the other hand, is of particular importance when the OSM has a low value of C_{H2O}, and a ε_g value of 95% has previously accepted as realistic level of heat exchange [32, 35]. Furthermore, it is critical to note that F_{Water} is fundamentally tied to the gas phase heat exchange efficiency (Eq. (2.6)). If ε_g were exactly 100%, F_{Water} would be zero. However $\varepsilon_g > 99\%$ will likely be cost prohibitive and still would not change the qualitative conclusions that will be discussed later this chapter. As a result, the energy penalty for preheating water is expected to be at least on the order of 1% of the energy required to heat n_{H2O} from T^o to T_L. Figure 2.3 shows how C_{H2O} can easily change by orders of magnitude. Therefore, even paying only 1% of this penalty can significantly impact efficiency

when the value of C_{H2O} is very low, and the results of this study represent a lower limit for F_{Water}.

One can establish the upper limit for efficiency by assuming the reactor is well-mixed with fast reaction kinetics and follows idealized reduction and oxidation paths similar to those shown in Figure 2.2 (shown again in Figure 2.6). Under these assumptions, the amount of water (n_{H2O}) required to oxidize the OSM from δ_R to δ_O can be calculated using this off-stoichiometric path, shown below.

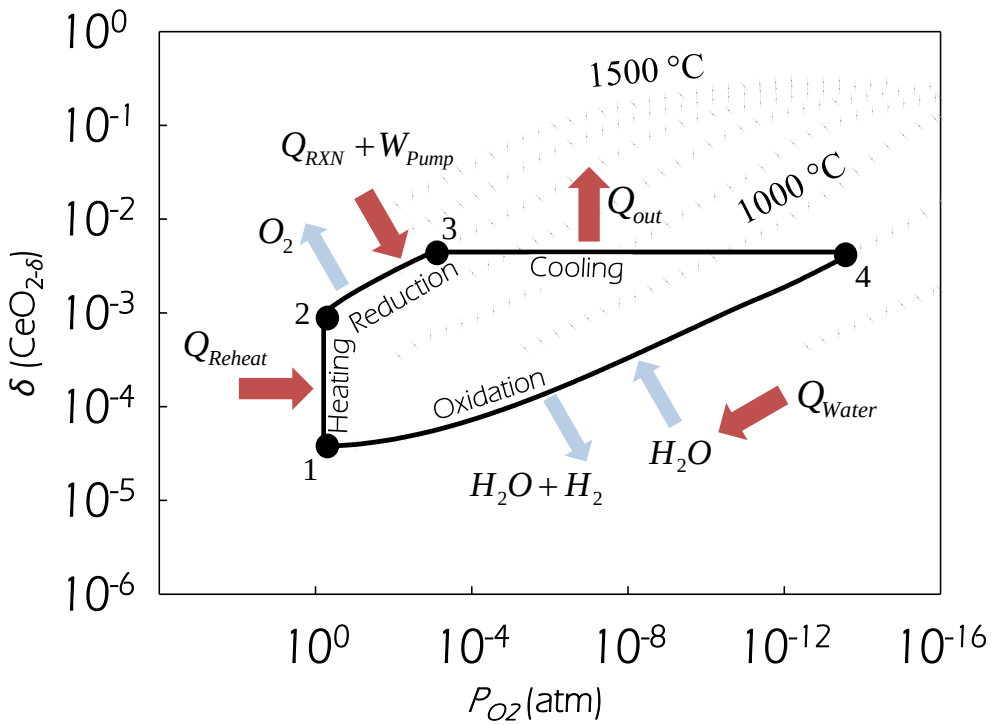

Figure 2.6: Equilibrium oxygen off-stoichiometry *(δ)* of ceria vs. $p_{O2.}$ Isotherms (dotted lines) are shown in 100°C incremented for temperatures in the range of in 800-1500°C[45]. An idealized oxygen off-stoichiometric cycle of the OSM for a two-step NRC is superimposed on this plot with solid lines (T_R=1300C, T_L=800C, p_{O2}=10^{-3} atm, and δ_O=0.0025). The OSM is headed from 800°C to 1300°C from points 1→2, reduced at 1300°C from points 2→3, cooled from 1300°C to 800°C from points 3 →4, and oxidized at 800°C from points 4→1.

After the OSM is reduced to δ_R, the temperature is lowered to T_L (Figure 2.6, location 4) and the OSM is then oxidized via exposure to steam (Figure 2.6, location 1). Assuming sufficiently fast kinetics, the equilibrium δ prescribed by Eq. (1.8) can be maintained at each p_{O2} along the oxidation path (Figure 2.6, 4→1). Furthermore, if the reactor gases are well mixed and in equilibrium, the p_{O2} along this path is established by the ratio between the hydrogen generated and unreacted water vapor present in the reactor. Because the reaction will never proceed past thermodynamic equilibrium, this calculation represents best case scenario and minimum amount of unreacted water traveling through the reactor. Using Eq. (2.15), the percentage of water converted to hydrogen can then be found as a function of δ. In this manner, the water required for oxidation can be found by evaluating Eq. (2.16), and in turn the energy factor associated with preheating this water is found with Eq. (2.6).

While these assumptions give a conservative estimate of the energy required to preheat water for oxidation, such calculations indicate how reactor performance is truly impacted by different materials and how efficiency can be ultimately improved. In reality, energy efficiency would be lower than this limiting case. However, relaxing these assumptions requires a more detailed description and analysis of the reactor that considers the kinetics of each reaction and is beyond the scope of this work.

Insights Obtained from Improved Model

Operational Parameters for Ceria, Optimized Reduction Pressure

Incorporating the losses associated with incomplete conversion and pressure dependent pump efficiency not only change the expected efficiency, but also the

optimum operating conditions. Figure 2.7 shows reference simulation data [35] for efficiency vs. p_{O2} and how this reference compares with results of the model described herein. This figure shows how the reference efficiency monotonically increases as p_{O2} decreases (Fig. 5 – black line). If only F_{Reheat} and F_{RXN} are considered, the efficiency predicted by the model presented herein (Fig. 5 – red dotted line) matches the reference data with good agreement. However, even for an OSM with a large value of ΔH such as ceria, when the energy required to preheat water is included, the efficiency reduces substantially when the oxidation temperature is fixed at 1100°C (Fig. 5 – red dashed line). Furthermore, if F_{pump} is considered, the monotonic relationship with decreasing p_{O2} is lost and efficiency decreases significantly when the value of p_{O2} becomes very low (Fig. 5 – solid red line). However, if the oxidation temperature is reduced to 900°C, the overall efficiency increases because the decrease in F_{Water} is greater than the increase in F_{Reheat} (Fig. 5 – solid blue line).

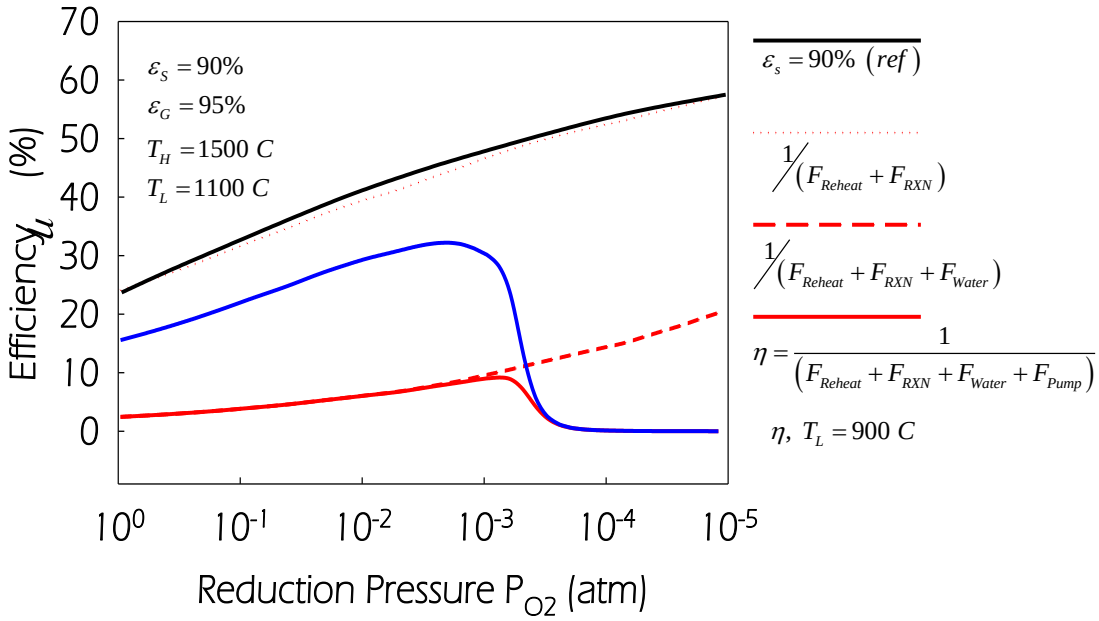

Figure 2.7: Efficiency of ceria vs. p_{O2} [35] (black, ε_S=90%, ε_G=95%, T_H=1500°C, T_L=1100°C, and δ_O=0.001). Predicted efficiency by model of this thesis (red - solid), predicted efficiency neglecting certain energy factors (red – dotted and dashed) , and predicted efficiency when T_L is reduced to 900°C (blue).

To further understand how each *operational parameter* (T_L, p_{O2}, and δ_O) impacts performance, energy factors for different conditions can be compared.

Table 2.2 : Default model parameters, unless otherwise specified.

Percent Solid Phase Heat Recovery	ε_S	50%
Percent Gas Phase Heat Recovery	ε_G	90%
Reduction Temperature	T_H	1500°C
Ratio of OSM Thermal Mass to Inert Reactor Thermal Mass	R_{TM}	0
Pump Efficiency	η_{Pump}	Figure 2.5
Specific Heat of OSM (ceria)	C_p^{OSM}	ref[68]
Specific Heat of Water	C_p^{H2O}	ref[50]
Reduction Enthalpy	$\Delta H(\delta)$	470 kJ/mol H_2* ref[45]
Reduction Entropy	$\Delta S(\delta)$	260 J/mol H_2* ref[45]

*Value represents and average valued of a functional property evaluated at typical operating conditions.

Figure 2.8(a) shows the energy factors and efficiency vs. p_{O2} of an optimized reactor. Of particular note is the effect of the pressure dependence of vacuum pump efficiency on reactor performance. Here, the efficiency reaches a maximum around $p_{O2}=10^{-3}$ atm. As the value of p_{O2} is reduced, the heat required to swing the temperature (Q_{Reheat}) remains constant but δ_R increases, thereby decreasing all energy factors other than F_{RXN}. As δ_R increases, more water is required to oxidize the OSM, but this additional water is used for oxidation when δ is large and C_{H2O} is high. Therefore, the energy required to preheat this water increases slower than the energy stored chemically, causing F_{Water} to decrease. For values of p_{O2} above 10^{-3} atm, the pump efficiency ranges between 1-50% and F_{Pump} is small. However at lower values of p_{O2}, pump efficiency becomes very poor and F_{Pump} increases dramatically which causes reactor performance (efficiency) to quickly decline.

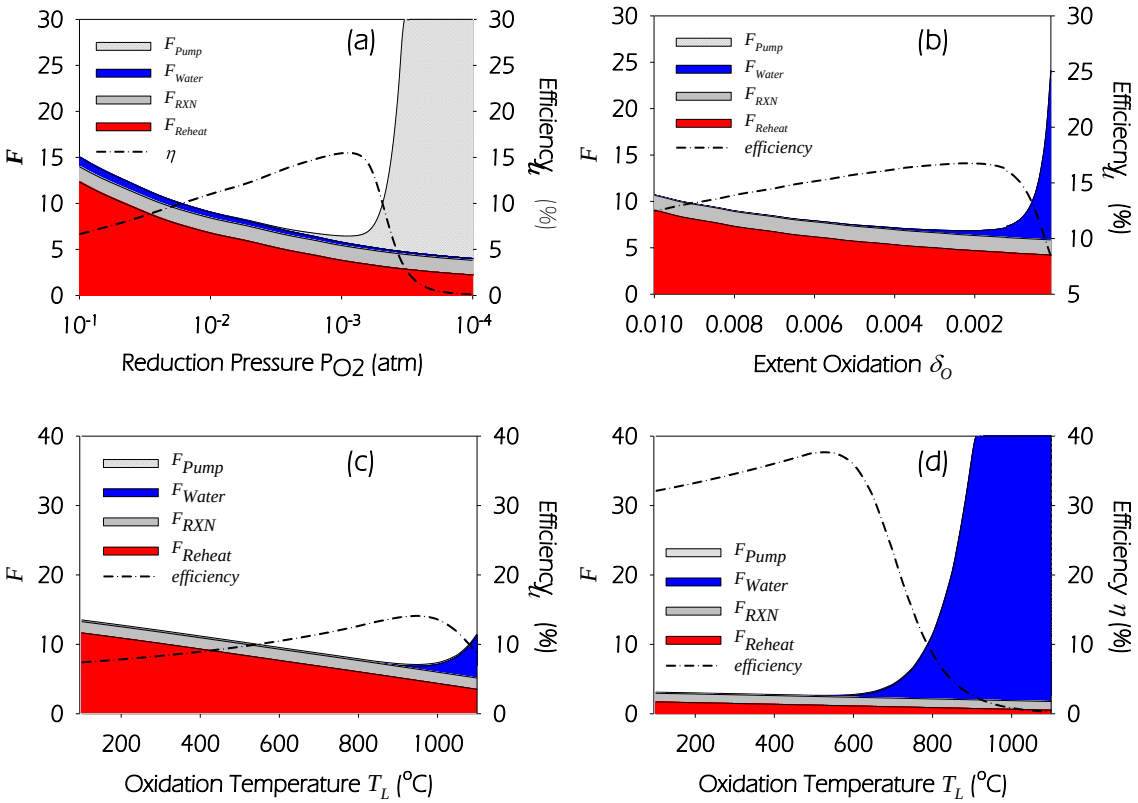

Figure 2.8: Optimized efficiency and energy factors vs. various *operating parameters* for ceria (a-c) and ceria with a value of ΔH reduced by 15% (b). For *operational parameters* other than the specific one shown, all plots were created with optimized values. Values of T_L=950°C, p_{O2}=0.0009 (atm), and δ_O=0.0023 were used for plots (a-c). Values of δ_O=0.0023 and p_{O2}=0.0009 (atm) were used for plot (d).

Although not analyzed quantitatively in the present work, the combined use of a vacuum and inert sweep gas to achieve lower values of p_{O2} and high η has been previously explored. Ermanoski, *et al*. [35] discussed how η is near zero for low values of p_{O2} when a sweep gas is used, owing to the large amount of gas needed to reach very low values of p_{O2}. They also reported a monotonic relationship between p_{O2} and η using a vacuum pump, and concluded that combining a vacuum pump with an inert sweep gas is not a feasible approach for increasing η by reducing p_{O2}. However, for a vacuum pump with pressure dependent performance, Figure 2.8(a) shows a non-monotonic relationship between η and p_{O2}. With pressure dependent pump efficiency there is a point of diminishing return and η decreases as the value of p_{O2} decreases further. This implies that the situation for a vacuum pump is similar of that of a sweep gas where an optimum value of p_{O2} exists with a maximum η. Furthermore, the energetic expense of producing and preheating a fixed volume of inert gas decreases with total pressure due to the reduced gas density. Purging at a reduced total pressure could mitigate the energetic cost of an inert sweep gas, reducing the optimum value p_{O2} and increasing maximum efficiency. For such a system, initially a vacuum pump could be used to reduce the total pressure until pump efficiency became prohibitively small. Next, a sweep gas can be used at the low total pressure to achieve even lower values of p_{O2} until further reduction exhibits diminishing returns on system efficiency.

Optimization of the Oxidation Temperature and Extent of Oxidation

The effects of incomplete chemical conversion can be seen in Figure 2.8(b) which shows reactor efficiency vs. δ_O. Even for ceria, complete oxidation at high temperatures requires large amounts of water and efficiency suffers for δ_O below an optimum value.

Additionally, the water required for oxidation increases further as ΔH of reduction decreases. This trend can be seen directly in Figure 2.8(c) and (d). Here, the efficiency is plotted vs. oxidation temperature for ceria (Figure 2.8(c)) and a hypothetical material identical to ceria with the exception that the value of ΔH has been reduced by 15% (Figure 2.8(d)). The optimum oxidation temperature for ceria is much higher than the OSM with a lower value of ΔH, which can be understood through the conversion - dependence (C_{H2O}) on T_L (Figure 2.3). Additionally, T_L appears in the limits of the integrals used to find F_{Reheat} and F_{Water} (Eq. (2.4) and (2.6) respectively). In Figure 2.8(c) and (d), F_{Reheat} decreases as T_L increases, but eventually C_{H2O} is so low that F_{Water} quickly increases presenting an effective wall for the efficiency. This situation prescribes an optimum T_L, which demonstrates why C_{H2O} must be considered in NRCs. Nonetheless, the larger amount of hydrogen produced per cycle decreases all energy factors except F_{RXN}, making higher efficiencies still possible with a lower value of ΔH.

Potential Efficiency Improvements with Reduced ΔH

While some energetic penalties increase upon reducing the value of ΔH, the overall reactor efficiency can increase if the *operational parameters* are optimized appropriately. Furthermore, both theoretical and experimental studies have shown that ceria alloys can exhibit lower values of ΔH of reduction [43, 62-67]. However, for actual materials the values of ΔH and ΔS can rarely be tuned independently [67]. Perovskite and ferrite oxides have also been demonstrated as viable OSMs with potentially lower values of ΔH *[48, 49, 60, 61]*, but whether or not these materials will lead to high efficiency in actual reactors remains undetermined.

Ceria is one of the few OSMs where the off-stoichiometry, ΔH, and ΔS have been determined for a wide range of applicable conditions [28, 45]. This thermodynamic data is needed to build the model described in this chapter but requires extensive experimental characterization work. This information does not typically exist for new materials, making it difficult to predict their performance. While this paper has shown that material properties including ΔH, ΔS, and C_P all impact reactor performance, as previously discussed, methods for tuning ΔS and C_p of the OSM remain unclear. Additionally, these material properties are functions of δ and/or temperature and their functional dependencies differ from one material to the next. One promising approach to OSM design could involve not only modifying the values of these material properties, but also engineering their functional dependence on δ with the aim of improving NRC performance. Again, owing to the significant experimental effort required to fully characterize ΔH and ΔS as a function of T and δ for new materials, some initial approximations are needed to narrow the range of viable materials for such detailed characterization. However, to get a general sense, one may assume that new materials have a similar ΔS and C_P as ceria, as a first approximation. With these assumptions, the ΔH of ceria can be scaled and used to predict the efficiency improvements that can be achieved by lowering the value of ΔH, which may offer some insight into future directions for materials design/selection. By fixing ΔS and C_P at values corresponding to ceria and scaling ceria's ΔH, the maximum efficiency can be found by optimizing T_L, p_{O2}, and δ_O. These results are shown in Figure 2.9 for several combinations of ε_G and ε_S along with the maximum theoretical efficiency for a given value of ΔH. With maximum

theoretical efficiency defined as $1/F_{RXN}$ or $HHV_{H2}/\Delta H$, this value reaches 100% at a ΔH that is 20% larger than LHV_{H2} because HHV_{H2} is 20% larger than $LHV_{H2.}$

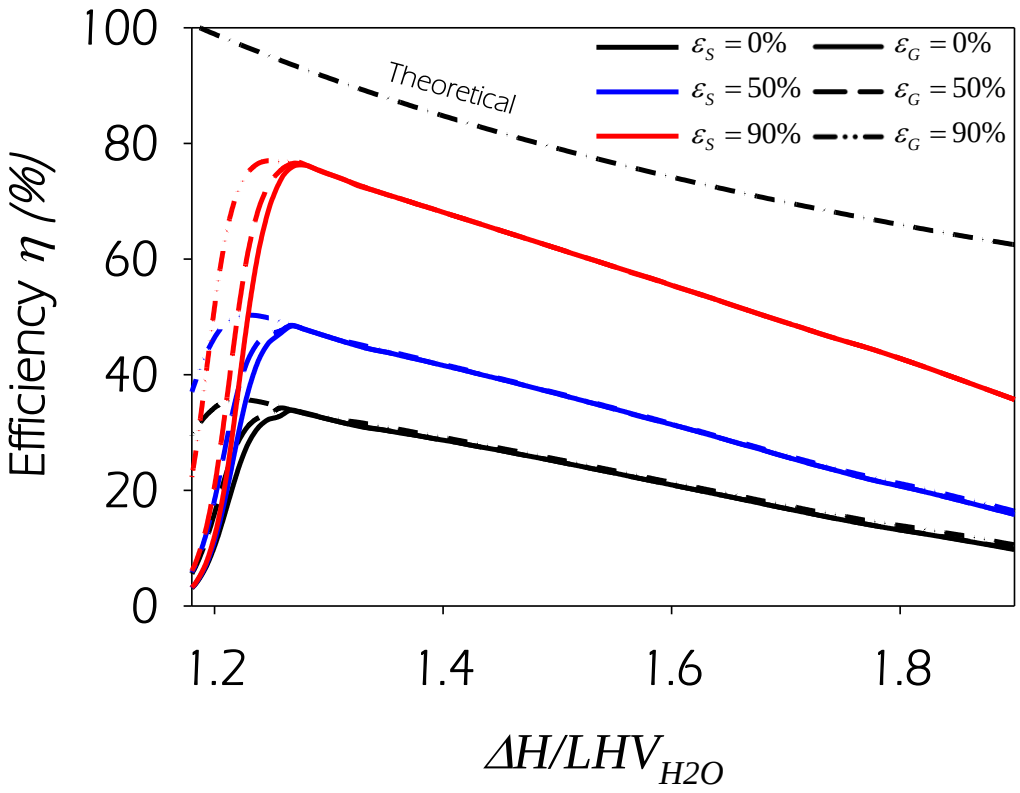

Figure 2.9: Optimized maximum theoretical efficiency and maximum NRC efficiency vs. ΔH for nine different combinations of ε_S and ε_G values. Line color indicates ε_S and line style indicate ε_G according to the legend. ΔH is normalized to the enthalpy of water dissociation (241 kJ/ mol H_2). The theortical maximum efficiency for a given OSM is the inverse of F_{RXN}. This value is 100% at $\Delta H/LHV_{H2O}$ of 1.2 because the ratio of the HHV_{H2O} to LHV_{H2O} is 1.2.

A lower limit on oxidation temperature was imposed at T_L of 100°C. Below this temperature water condenses and while it is conceivable to thermochemically split liquid water, the analysis must be modified which is beyond the scope of this work. Nonetheless, it may still be possible to split CO_2 or other oxygen containing molecules of interest below 100°C, but oxygen mobility in the OSM decreases at reduced temperatures and the lower limit for T_L is likely above 100°C and this will be discussed in detail later

this chapter. As expected, Figure 2.9 shows efficiency increases as the value of ΔH decreases, and efficiency is sensitive to ε_S but it is not sensitive to ε_G. Under optimized *operational parameters* and T_L > 100 °C, F_{water} is relatively small (Figure 2.8) and variations in ε_G have little impact. The reason F_{Water} is small because the optimum operating conditions occur shortly before encountering the dramatic order of magnitude increase in F_{Water} as δ_O is decreased. With this lower bound on oxidation temperature, for very low value of ΔH, C_{H2O} decreases but T_L cannot be further reduced to counteract the effects of poor conversion. With the inability to reduce T_L, the only way to oxidize the OSM is with excessive amounts of unreacted water and eventually F_{Water} becomes the dominating loss, reducing efficiency. Furthermore, because increasing F_{Water} is the reason efficiency decreases at low values of ΔH, the point at which further reducing the value ΔH decreases efficiency is moderately sensitive to ε_G. This sensitivity is observed in Figure 2.9 where higher efficiency peaks are achieved with larger values of ε_G.

While all *operational parameters* are coupled, the optimum value of p_{O2} is mainly governed by the η_{Pump}, ε_S, and ΔH, as shown in Figure 2.10. For optimized operating conditions, as the value of ε_S increases, F_{Reheat} decreases and F_{Pump} becomes a higher portion of the denominator of Eq. (2.3). As F_{Reheat} decreases, the value of p_{O2} must increase to reduce F_{Pump} in order to reach the highest possible efficiency.

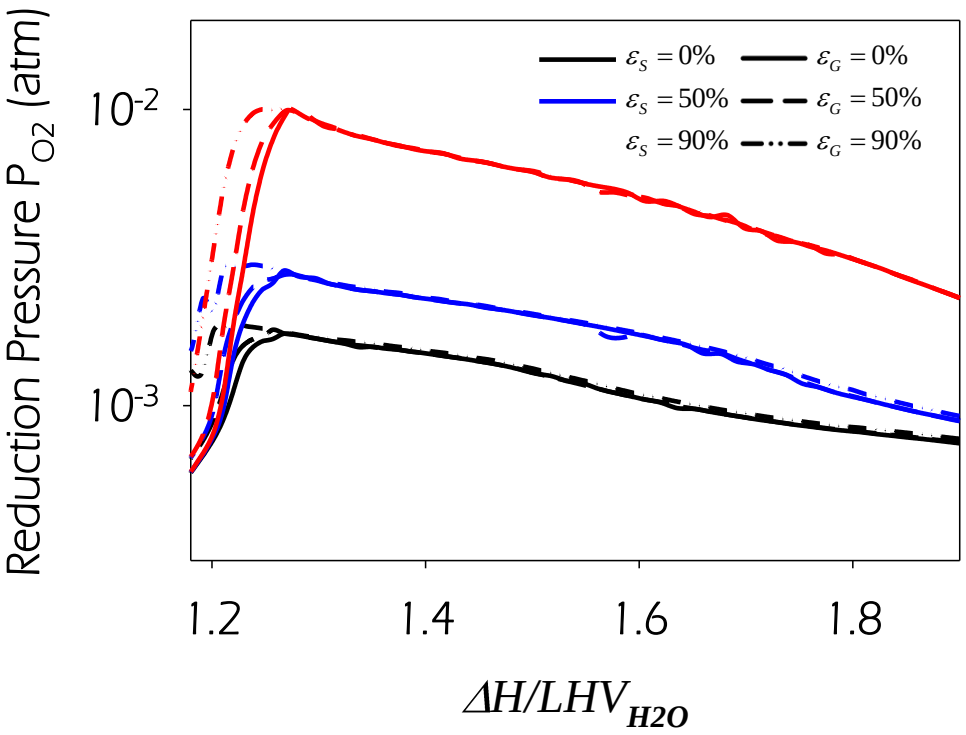

Figure 2.10: Optimized p_{O2} vs. ΔH for nine different combinations of ε_S and ε_G values. Line color indicates ε_S and line style indicate ε_G according to the legend. ΔH is normalized to the enthaply of water dissociation (241 kJ/ mol H_2).

Figure 2.11 shows the largest and smallest values of optimal T_L for all combinations of ε_S and ε_G considered. Here, the optimal T_L increases as the value of ΔH increases, because materials with large values of ΔH have high C_{H2O}. Furthermore, optimal T_L increases as ε_G increase because the energetic penalty for preheating unreacted water is small when ε_G is high. On the other hand, for high values of ε_S, the energetic expense of heating from T_L to T_H decreases, reducing optimum T_L. When ε_S=0 and ε_G=90%, the minimum temperature is never reached because F_{Reheat} is nearly equal to the sum of all other energy factors when $R_{\Delta H}$ is low. Therefore, further reductions in

temperature would reduce efficiency more than using large amounts of water for oxidation.

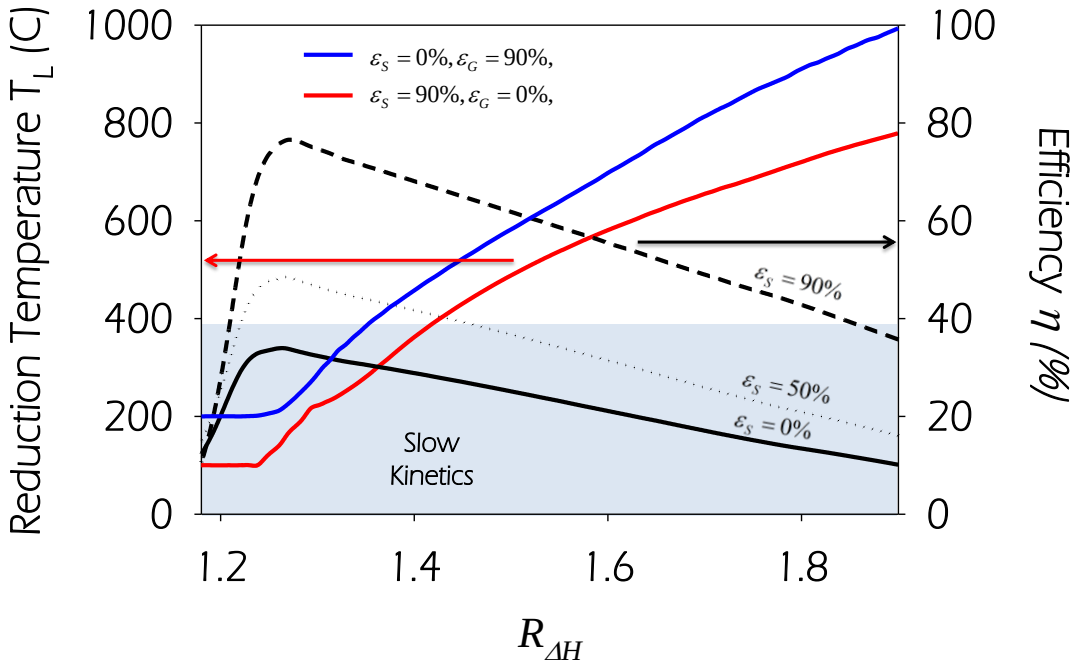

Figure 2.11: The maximum value and the minimum value of T_L for all combinations of ε_S and ε_G considered. Average optimized efficiency vs. ΔH for ε_S=0%, 50%, and 90% respectively. ΔH is normalized to the enthaply of water dissociation (aproximatly 241 kJ/ mol H_2).

In all cases, the optimum value of ΔH is higher than the enthalpy of water dissociation (approximately 241 kJ/mol H_2). In Figure 2.11, the optimum value of ΔH is more than 20% above the enthalpy of water dissociation. For values of $R_{\Delta H}$ below 1.2, C_{H2O} becomes very small and the large amounts of water required for oxidation decrease the efficiency. While low temperature oxidation has been demonstrated [69] for nanomaterials, oxidation kinetics could become prohibitively slow even at higher temperatures [70] for materials with larger grain/pore sizes (i.e., material that may exhibit

higher temperature stability and cycle durability). Furthermore, Figure 2.12 shows the oxidation of $(Sr_{0.2}Ca_{0.2}La_{0.6})(Al_{0.25}Ga_{0.25}Mn_{0.50})O_3$ with R_{H2O}≈20 at 400°C and 500°C. Both samples were a thin layer of fine powder, which will be further discussed in Chapter 4. The samples were gradually reduced at constant temperature where the low p_{O2} environment was achieved by purging an argon sweep gas. Next, the inert purge gas was replaced by 21% oxygen balanced in argon to oxidize the samples isothermally. This figure shows how oxidation at 400°C takes nearly 35 minutes to reach equilibrium. However at 500°C, equilibrium is reached in less than 5 minutes, further demonstrating the kinetic limitation of oxidizing at low values of $T_{L.}$

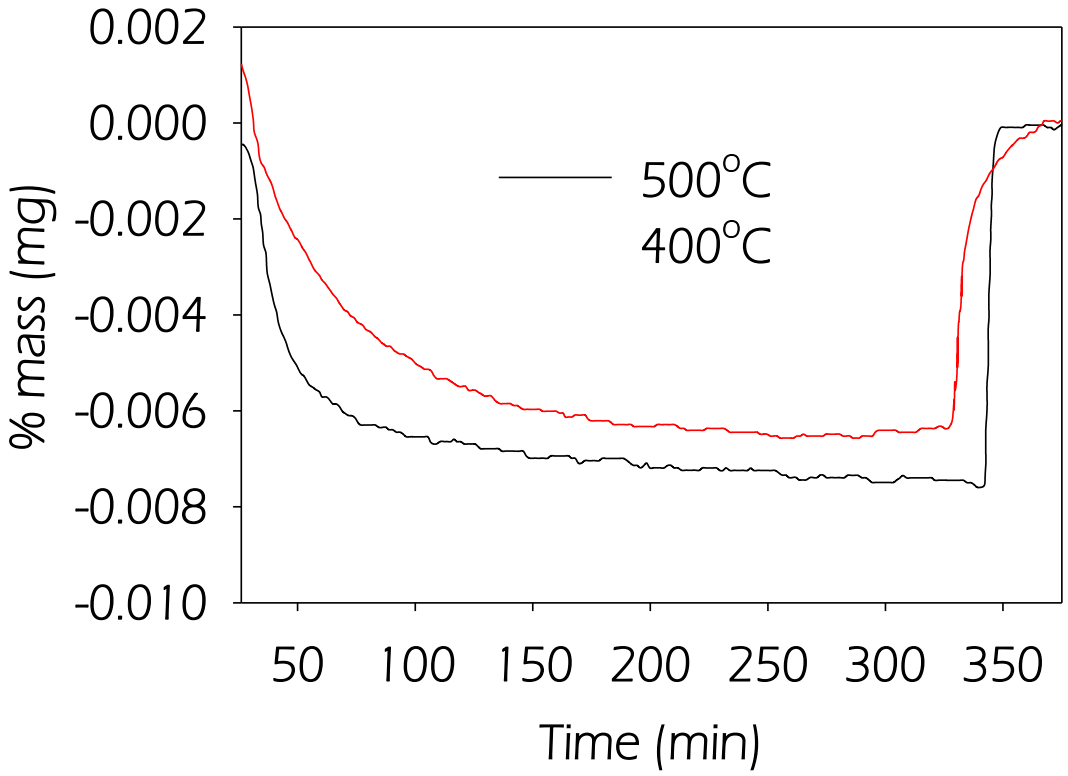

Figure 2.12: Thermogravimetric oxidation of $(Sr_{0.2}Ca_{0.2}La_{0.6})(Al_{0.25}Ga_{0.25}Mn_{0.50})O_3$ with R_{H2O}≈20 at 500°C (bottom) and 400°C (top). Oxidation at 400°C has not reached equilibrium after 35 minutes while oxidation at 500°C equilibrates in approximately 5 minutes. R_{H2O} was measured at 23 for 500°C and 38 for 400°C.

With slow kinetics, long reaction times and increased $F_{Loss.}$ If the lower limit for T_L is restricted to temperatures of approximately 400°C, then the optimum value of $R_{\Delta H}$ increases to almost 1.4.

Figure 2.13 shows the largest and smallest values of the averaged C_{H2O} for all combinations of ε_S and ε_G considered. For similar reasons, the relative values of these curves are similar to the values of T_L in Figure 2.11. All averaged C_{H2O} decrease sharply after T_L reaches its minimum value. Additionally, for $R_{\Delta H}$ above 1.3, the minimum value

of the averaged C_{H2O} is approximately 3.55%. This indicates how NRC efficiency will certainly be low for materials where the water required for oxidation is greater than 100 times the hydrogen produced and the implications of this will be discussed in Chapter 3.

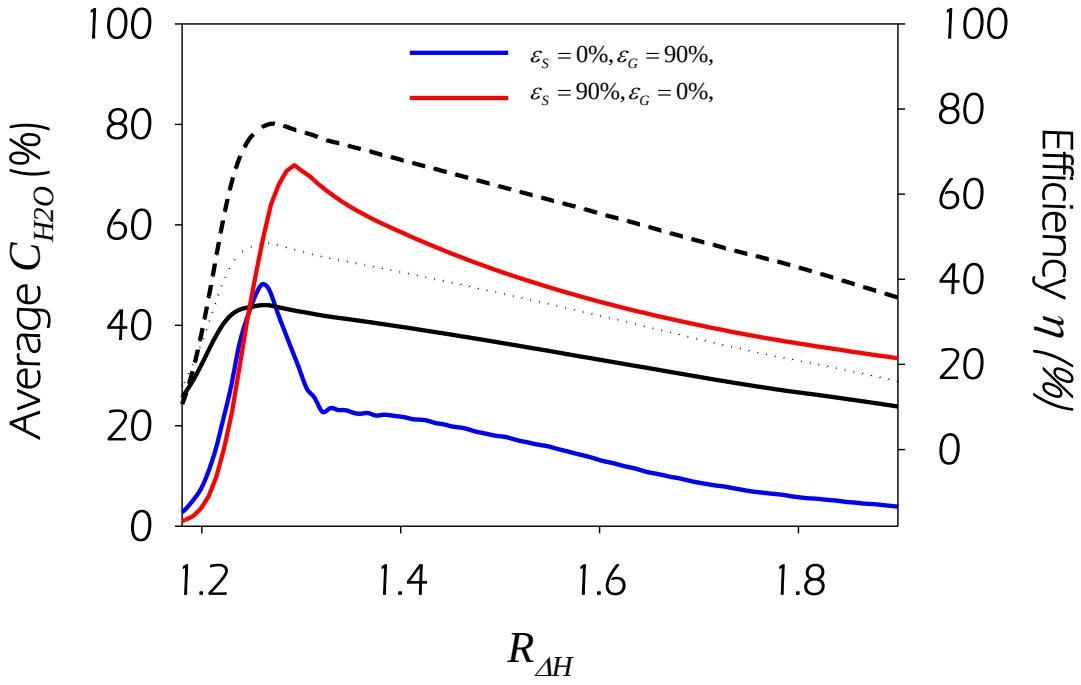

Figure 2.13: Maximum and minimum values of averaged C_{H2O} for all combinations of ε_S and ε_G considered. Average optimized efficiency vs. ΔH for ε_S=0%, 50%, and 90% respectivle. ΔH is normalized to the enthaply of water dissociation (241 kJ/mol H_2).

Trade-offs between T_L and δ_O

Due to the energetic trade-offs between oxidizing at lower temperature with a high value of C_{H2O} and oxidizing at higher temperature with low value of C_{H2O}, efficiency has a very shallow maximum with respect to T_L and δ_O. These shallow maxima indicate that many different combinations of these two parameters can give a similar, near maximum efficiency. This can be seen in Figure 2.14 for two values of ΔH and optimized *operational parameters*. For higher values of ΔH (Figure 2.14(a)), when the oxidation

temperature is low (<900°C), high efficiency is achieved by oxidizing the OSM closer to completion (i.e. low values of δ_O). However, at higher oxidation temperatures, large amounts of water are required to oxidize the OSM and the efficiency peaks further away from complete oxidation (i.e. at relatively large values of δo). For a lower ΔH (Figure 2.14(b)), a value of low C_{H2O} reduces the range of T_L with near maximum efficiency, and near maximum efficiencies are not possible for relatively low values of δ_O.

For a given material, the oxidation temperature (T_L) can be selected from a range of temperatures defined by this shallow maximum all of which have nearly the same efficiency (between 800-1000°C in Figure 2.14(a)). Faster oxidation reaction kinetics generally occur at higher temperatures, motivating higher value of $T_{L.}$ However, increasing T_L increases the average temperature of the reactor, increasing $\dot{Q}_{Loss}$. For high values of ΔH, where T_L can be selected from a range of values, optimum values should likely be selected from a more detailed analysis which considers the competition between reaction kinetics and heat leakage.

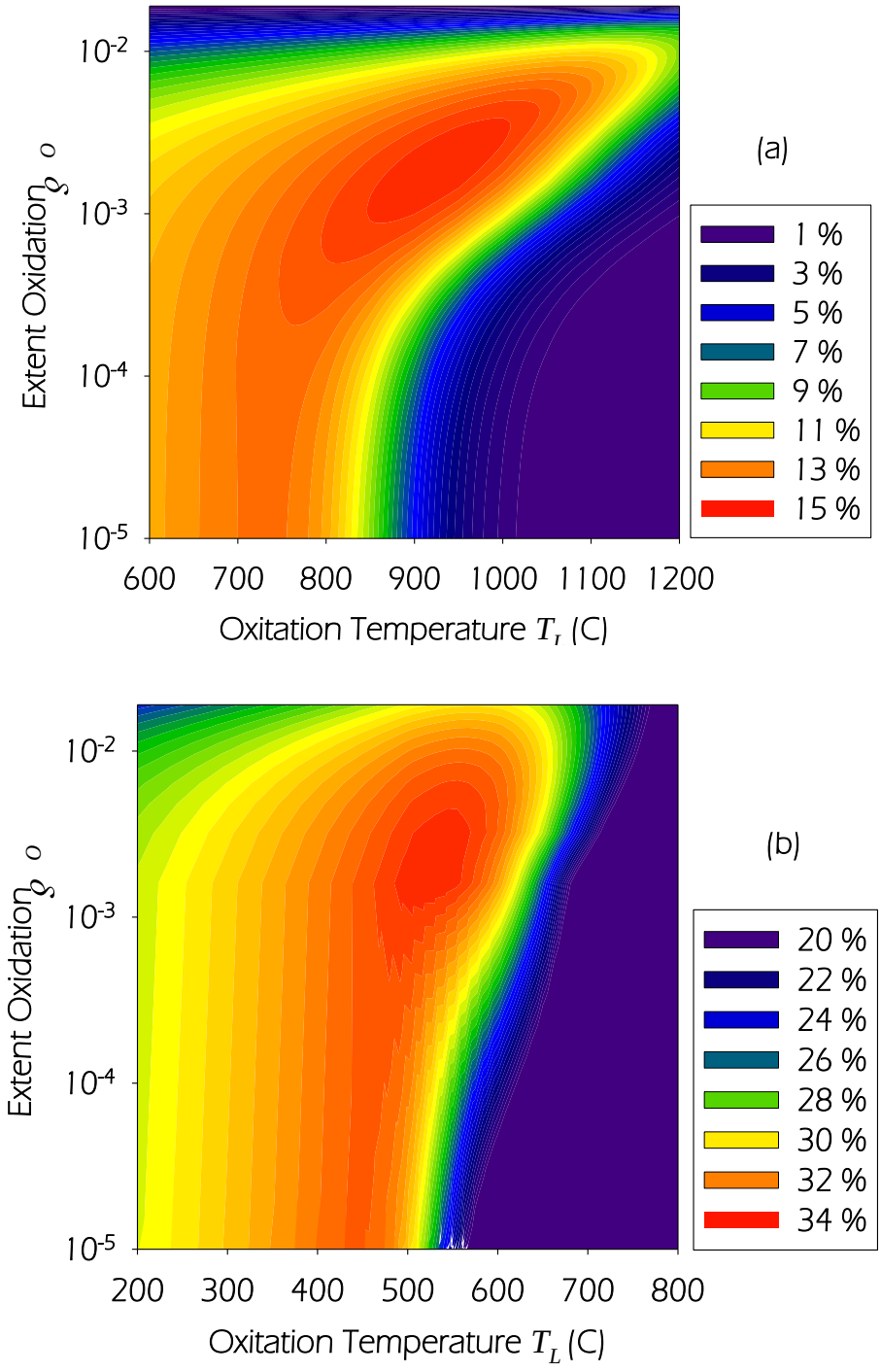

Figure 2.14: Efficiency (η) contour plots vs. δ_O verse T_L for (a) ceria and (b) a ceria-like material with the value of ΔH of reduction reduced by 15% (ε_G=0.9 and ε_S=0.5). The shallow maximum is shown by the near constant, maximum efficiency over a wide range of values for T_L.

Discussion of Modeling results

It should be emphasized that the quantitative results shown here are a direct result of the values in Table 2.2 and will change for different *reactor parameters*, such as T_H, pump efficiency, and *OSM properties* ($\Delta H(\delta)$, $\Delta S(\delta)$, and C_P). However the underlying physics and qualitative relationships governing these results are not expected to change dramatically, as the major innovation here is the new modeling method. Pump efficiency is a function of p_{O2}, and lower limits for the value of p_{O2} come from this dependence. Materials with low values of ΔH will also have low values of C_{H2O}. Furthermore, in combination with lower limits on T_L (likely due to kinetics), ε_G and C_{H2O} establish a lower limit for ΔH. This lower limiting value of ΔH will to be greater than the enthalpy of water dissociation for values of T_L greater than 100°C.

Furthermore, the importance of reactor design should be emphasized. While the *operational parameters* and ΔH define a highly coupled design space, T_R, ε_G, ε_S, and R_{TM} are also likely coupled through reactor geometry and operational conditions. As an example, Lapp, *et al*. discussed a reactor where ε_S depends on the difference between T_H and T_L (further motivating the operation of the reactor at the highest value of T_L inside the shallow maximum with near peak efficiency for a given value of ΔH) [53]. A more thorough analysis would account for this dependence and is likely specific to a given reactor design/concept. Other considerations include the coupling of ε_S and the ratio of inert reactor thermal mass to OSM thermal mass (R_{TM}) which appears as a coefficient in F_{Reheat} (Eq. (2.4)). A well designed reactor should minimize this ratio, similar to a packed bed reactor where none of the inert reactor material experiences a temperature swing

between T_H and T_L. For other reactor designs where this ratio is not small, Eq. (2.4) shows the important parameter to minimize is $(1-\varepsilon_S)(R_{TM}+1)$.

From the results in Figure 2.9, it can be seen that ΔH and $(1-\varepsilon_S)(R_{TM}+1)$ are of roughly equal importance for achieving high efficiency in NRCs. Siegle *et al*. reported that thermochemical conversion efficiency must exceed 30% to be competitive with solar driven electrolysis. Even for the conditions analyzed here, this metric is possible but will likely require improved OSMs. For ceria ($\Delta H/\Delta H_{H2O}\approx 2$), more than 50% solid phase heat recover is required to exceed NRC efficiencies of 30%, but with modest reductions in ΔH, η larger than 30% are possible for ε_S less than 50%. Therefore the most promising approach involves improvements in both reactors and OSMs. Furthermore, because the optimum ΔH is only a weak function of ε_S and ε_G, the work to improve reactor design and engineer new materials can proceed somewhat independently except for issues associated with materials compatibility.

For reactors with an OSM and reduction temperature that requires a low p_{O2} to achieve high δ, a vacuum pump has been commonly suggested as the method of choice for achieving a low value of p_{O2}. With constant pump efficiency, F_{Pump} is small relative to other energy factors and efficiency monotonically increases as p_{O2} decreases. However, as shown herein, mechanical pumping efficiencies are not constant and are highly sensitive to reduction pressure. Furthermore, this efficiency is very low at lower pressures due to reduced molecular flow rates from low gas densities and a constant frictional loss. While better pumps optimized for thermochemical cycles may be possible, flowrate and in turn efficiency will still be pressure dependent and this dependence in combination with ε_s defines the optimum p_{O2} for high performance. For the pumps considered, the

high losses that accrue from pumping large volumes of O_2 at low pressure makes the use of vacuums alone impractical for operating at reduction pressures less than ~10^{-3} atm. This is important, because much material testing focuses on operating at pressures in the range of 10^{-5}-10^{-6} [46, 48], mainly out of experimental convince because this are the p_{O2} of many commercially available pure inert gasses (argon, helium, and nitrogen). Additionally, the turbo pump shown in Figure 2.5 is considered a highly energy efficient pump for high vacuum as this technology is commonly used in semiconductor manufacturing, an industry where achieving a high vacuum efficiently is an economic driver.

Implementing new OSMs with low values of ΔH allows greater oxygen off-stoichiometry to be achieved during reduction which, may increase efficiency. As a result, discovering advanced OSMs is one of the most promising ways to increase system efficiency. Many analyses assume 100% water to hydrogen conversion or small or fixed losses from incomplete conversion (such as 3%) [15, 35]. While this assumption is valid for ceria (an OSM with high conversion), lowering ΔH reduces the extent of conversion. Thus, when evaluating new materials with lower values of ΔH or when oxidizing at a high T_L, the impact of such parameters on F_{Water} must be accounted for in efficiency calculations.

Lower values of ΔH lead to higher fuel production per cycle but also lower conversion (increasing F_{water}). These opposing effects suggest that for a given OSM, there are optimum *operational parameters* that are highly depended on T_L. For T_L as low as 100 °C and a material similar to ceria, the optimum value of ΔH is greater than the enthalpy change for water dissociation by a factor of ~ 1.2.

Implication for New Materials development.

Many studies compare new OSMs to ceria as an evaluation metric by measuring the hydrogen produced per cycle under a common reduction p_{O2}, a common reduction temperature, and with very large amounts water during oxidation (this will be discussed in more detail in the next chapter). While this method serves as a quick method for screening materials as viable OSMs, deeper reduction may not lead to higher efficiencies, because optimum efficiency can occur at different values of p_{O2} and T_L for different materials. A material that produces more H_2 than ceria will not necessarily achieve higher efficiencies in a real reactor. For example, ceria can be oxidized at a high temperature and even though less H_2 may be produced with ceria, Q_{Reheat} is smaller than that of a material with a lower value of ΔH, so it is possible that the overall efficiency could still be higher for ceria. We assert that a model such as the one described herein should be used to estimate the NRC efficiencies possible from selected *reactor parameters* and data describing $\Delta H(\delta)$ and $\Delta S(\delta)$ for new materials. This would allow one to predict limiting efficiencies, and compare candidate OSMs on an equal footing.

A METHOD FOR THERMOGRAVIMETRIC SCREENING OXYGEN STORAGE MATERIALS FOR THERMOCHEMICAL NONSTOICHIOMETRIC REDOX CYCLES

Figure 2.9 shows the possible performance enhancements for NRCs. Through innovative reactor designs with improved solid phase heat recovery and the implementation of OSMs with values of ΔH inside the ranges outlined in the previous chapter, thermochemical conversion efficiencies above 30% are possible. As discussed previously, advances in both areas are critical to the improvement of these systems. However, this chapter will focus only on the advances possible through lowering the OSM reduction enthalpy. This chapter begins by reviewing both materials that show promise as high performance OSMs and previous work that has focused on identifying and characterizing these materials. Particular attention is paid to the task of identifying new materials. Specifically, need to measure the amount of water used during oxidation and motivation for increasing the typical values of p_{O2} above 10^{-6} is explained. Furthermore, the amount of hydrogen produced per cycle alone does not serve as a good basis for comparison which will be illustrated by the ensuing discussion. Finally, an improved method for screening OSMs utilizing TGA will be introduced and explained.

Review of Promising Materials and Current OSM Screening Methods

Much effort has been given to the identification of new OSM materials. Previous studies have shown that alloyed CeO_2, iron oxides, *Mn*, *Mg*, *Co*, *Zn*, and/or *Ni* alloyed ferrites, and alloyed *La* and/or *Sr* based perovskites are potential high performance

OSMs capable of splitting water[8, 10, 43, 46, 48, 49, 57, 71-77]. Pure ceria is a particularly well characterized OSM [28, 45, 78], and the availability of complete thermochemical and kinetic information enables detailed system analysis and efficiency calculations [15, 32-36, 79]. However, perovskites and ferrites are of particular interest because, relative to ceria, these materials can be reduced to a greater extent at moderate temperatures, implying a lower value of ΔH. This lower ΔH allows large amounts of hydrogen production per cycle which can potentially lead to higher efficiencies.

For perovskites and ferrites, the number of options for OSM chemical composition is extensive due to the large number of material variations enabled by different alloy species and alloying amounts. Furthermore, the experimental effort needed for detailed material characterization of new OSMs is also extensive (such as the data available for ceria in the figure below). The large number of options available for perovskites and ferrites in combination with the appreciable experimental effort needed for their detailed characterization makes the construction of detailed system models for all OSMs time prohibitive. This motivates the need for quick OSM screening methods.

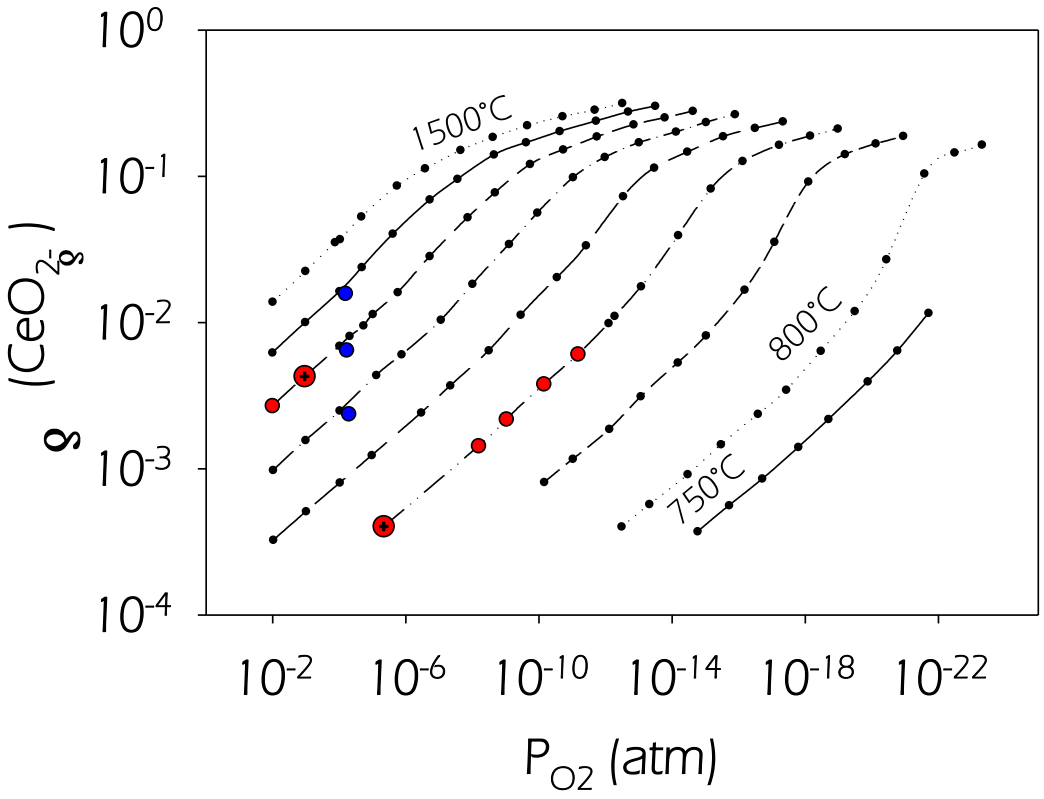

Figure 2.15: Isothermal δ versus p_{O2} for nonstoichiometric ceria from 750 °C and 800-1500°C in 100°C increments. Measurements by Panlener et al. [45] shown in black and measurements to reproduce this data with the method describe in Chapter 3 are shown in blue. Red dots show example data needed to predict a single efficiency for a specific set of *operational parameters*. Red dots with black crosshairs shows the example data needed to predict the hydrogen produced (OSC) per cycle for a specific set of operational parameters.

The most common screening method in literature utilizes a bench top reactor and gas chromatography to analyze the effluent gasses and determine fuel production capacity for specific values of T_H, T_L, and p_{O2}. This characterization method also typically oxidizes the OSM to a value of δ_O=0. The fuel production capacity is found from $n_{H_2} = \delta_R - \delta_O$, also known as the oxygen storage capacity (OSC) [75, 80]. Typically, such studies compare the OSC of a material of interest directly to ceria at specific testing

conditions. While this method is viable for determining a material's OSC and if it is able to split water under specific testing conditions, this test provides only a fraction of the information necessary to predict reactor efficiency. An example of such results is shown below [46].

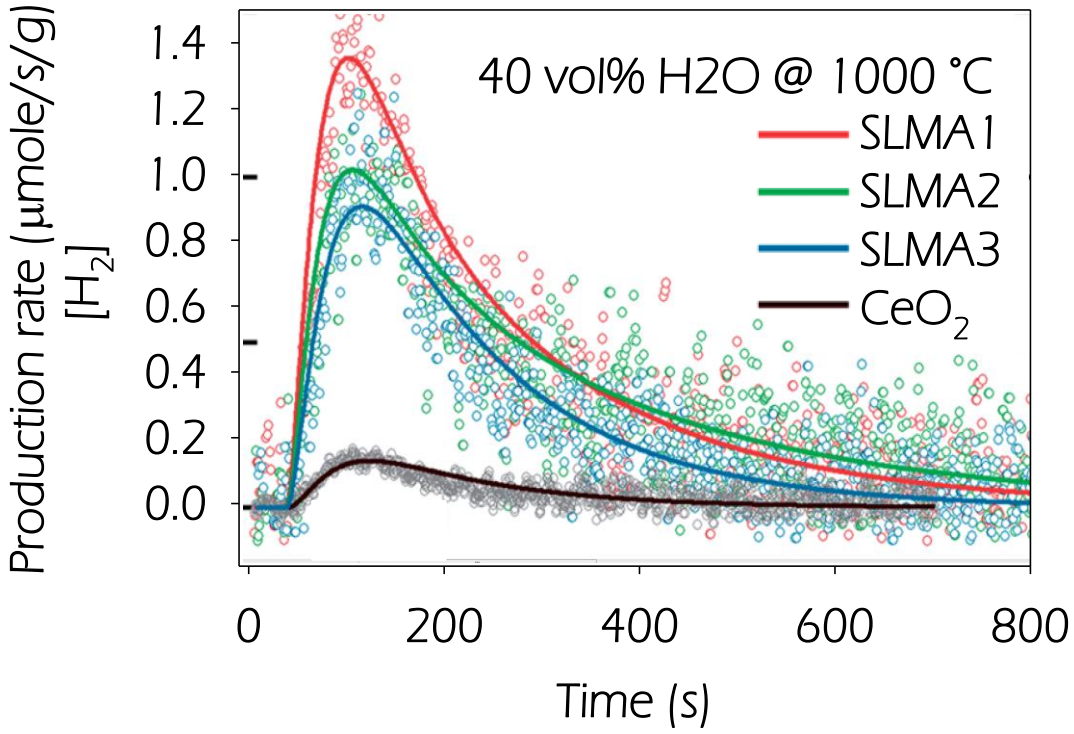

Figure 2.16: H_2 production of three perovskite chemistries and ceria vs. oxidation time taken from [46]. Samples were reduced at 1350°C in helium (approximately $p_{O2}=10^{-6}$) and oxidized at 1000°C in with an $R_{H2O}>100$. SLMA1 is $Sr_{0.6}La_{0.4}Mn_{0.6}Al_{0.4}O_3$. SLMA2 is $Sr_{0.4}La_{0.6}Mn_{0.6}Al_{0.4}O_3$. SLMA3 is $Sr_{0.4}La_{0.6}Mn_{0.4}Al_{0.6}O_3$.

For ceria with $\varepsilon_G=0.9$ and $\varepsilon_S=0.5$, Figure 2.14 shows how the optimum thermochemical conversion efficiency of 17% occurs at approximately $p_{O2}=10^{-3}$ atm, with T_L between 850-1000°C, and δ_O between 0.001-0.002. However, if the value of ΔH

were 15% lower, optimal efficiency of 38% occurs at approximately p_{O2}=1.7×10^{-3} atm, with T_L between 475-550°C, and δ_O between 0.001-0.022. This illustrates how the maximum efficiency of two materials can occur at different operation conditions. Furthermore, efficiency can be very sensitive to the operating conditions. For example, if each of these materials were operated under the optimum conditions of the other, efficiencies would fall to 10% for ceria and 0.8% for ceria with a 15% lower ΔH, respectively. These results alone suggest that a direct comparison at identical *operational parameters* will not determine if an OSM with a larger OSC will yield higher NRC efficiencies than ceria in an optimized reactor, specifically if the OSC of ceria is not measured under optimum conditions. Furthermore, for the data shown in Figure 2.16, the value of R_{H2O} was kept above 100. Translated to an actual reactor, this means that the amount of water in the product stream of the oxidation reaction is at least 100 parts water per one part hydrogen. This can be understood through Eq. (2.6), by setting $n_{H_2O} \big/ \left(\delta_R - \delta_O\right)$ = 101, T_L = 1000°C, and ε_G = 0.9. Utilizing these values and neglecting the exothermic energy release on oxidation would result in value of 2.9 for F_{Water}. Ignoring all other losses (e.g. F_{Reheat}, F_{RXN}, F_{Pump}, and F_{Loss}), a maximum efficiency of 35% can be determined from the losses of preheating water alone. If a reactor was operated under these conditions at this water to hydrogen ratio, actual efficiency would be much lower than 35% when other energy factors are considered. These same calculations are performed for water to hydrogen ratios ranging from 10-10,000 in the table below. It should be noted that these calculations are also a strong function of T_L and the losses associated with preheating water will decrease for lower values of T_L.

Table 2.3: Maximum efficiencies obtained by considering only the losses of preheating water and neglecting all other losses for different values of R_{H2O} amounts of unreacted water traveling through the reactor.

Ratio of Water used to Hydrogen Produced	10	100	1,000	10,000
Mole of Water to be Preheated	11	101	1001	10001
Fwater	1.3	2.9	28.6	117.6
Max Efficiency Ignoring Other Losses	77%	34%	3%	1%

While it may be possible for these materials to outperform ceria if lower water to hydrogen ratios are used, their ability to split water under lower ratios is unclear from the data presented in Figure 2.16 raising the question of what exact experiment would yield these conclusion. Furthermore, the previous discussion does not provide evidence against the perovskites examined in Figure 2.16, but rather evidence against the experiment used to compare these new OSMs to ceria. By not tracking the water used during oxidation and by providing unlimited amounts of water for oxidation, one cannot predict how an OSM will perform in an actual reactor. In practice, there are energy penalties associated with preheating water used during oxidation and therefore motivations for oxidizing with minimal water. Furthermore, if the helium used during reduction was of typical scientific grade ("ultra high purity," UHP helium), and the system had no significant leaks, oxygen levels are approximately 1 ppm or 10^{-6} atm, much lower than the optimum reduction pressure of any material in Figure 2.10 (it should be noted that lower bound on the optimum value of p_{O2} is a direct result of $\eta_{Pump}(p_{O2})$ and could be further decreased with improved vacuum pump efficiency). An experiment that would determine if new OSMs would lead to high thermochemical conversion efficiencies would determine the following: reducing them at values of p_{O2} that are more attainable in a reactor,

minimizing and measuring the water use during oxidation, and ascribing an appropriate penalty for preheating this water (similar to the numerator of Eq. (2.6)).

With this approach and good approximations for C_P^{OSM} and η_{Pump}, reasonable predictions can be made for all F_{Water}, F_{Reheat}, and F_{Pump} (specific to selected values of ε_S and ε_G). With these energy factors, a more complete understanding of the performance possible with new OSMs can be assembled. It should be noted that F_{RXN} can be large for materials with large values of ΔH. However, the search for new OSMs typically targets lower values of ΔH, and the losses from F_{RXN} will be less than those for ceria. Also, F_{Loss} is likely comparable for all OSMs. Assuming an upper limit of ΔH to be that of ceria allows the maximum value of F_{RXN} to be bound. Furthermore, by neglecting F_{Loss} and applying the results of Chapter 2, a more complete picture of the reactor efficiencies possible can be calculated.

Thermogravimetric Testing for Screening New Materials

The efficiency model detailed in Chapter 2 was constructed from the detailed thermodynamic map of δ for ceria, shown in Figure 2.15. Reviewing this method, first, T_H and p_{O2} are used to find δ_R. Second, the unreacted water traveling through the reactor is found by calculating the equilibrium value of R_{H2O} established by T_L and the instantaneous p_{O2} and then integrating along the y-axis of Figure 2.15 from δ_R to δ_O. Finally, each energy factor and in turn the cycle efficiency are determined using Eq. (2.4) - (2.19). This method required the entire map of δ in order to parametrically sweep the four dimensional space of $\eta = \eta\left(T_L, \delta_O, P_{O_2}\right)$ and optimize the reactor efficiency. As

previously stated, determining the complete maps of δ requires a large experimental effort and is not practical for a larger number of materials using currently available instruments. However, the efficiency associated with specific values for p_{O2}, T_L, and δ_O can be found with only a partial thermodynamic maps of δ (examples are shown by red dots in Figure 2.15). These data points are only a fraction of the complete δ map and therefore require a smaller experimental effort. For this approach, initially, a few values of δ_R are determined at selected values of T_H and p_{O2}. Next, δ_O is determined at a selected value of T_L for several water to hydrogen ratios (this ratio establishes an equilibrium oxygen partial pressure which is plotted on the x axis). With these experimental results, one can determine the value of several quantities: the hydrogen produced per cycle can be found for $\delta_R - \delta_O$, F_{Water} can be found by integrating under the T_L isotherm from δ_R to δ_O, F_{Reheat} is calculated with T_H and T_L, and F_{Pump} can be approximated with the p_{O2} corresponding to the chosen value of δ_R. While this approach only predicts a single efficiency, with intuitive choices of T_H and T_L, near maximum efficiency could be calculated quickly and used to evaluate a material, because it considers the unreacted water traveling through the reactor. This method is much faster than the method of fully characterizing the off-stoichiometry of a material which is required to determine the absolute maximum efficiency. For example, Figure 2.15 contains 113 data points each of which take roughly one day to determine through TGA. However, only the seven data points shown in red are used to find a single efficiency.

While seven measurements of δ can be conducted much faster than 113 measurements, taking six thermogravimetric data points still requires more than a week

of testing for a single material. With many OSM options, the time required by this approach could still be prohibitively large. However, the hydrogen produced per cycle (OSC) can be determined with only two measurements of δ (examples shown by red dots with black crosshairs in Figure 2.15). First, by selecting T_H and p_{O2}, δ_R can be determined. Next, after choosing T_L and a reasonable water to hydrogen ratio (so that the penalty of preheating this water does not result in very low efficiencies), δ_O can be determined. Then, the hydrogen produced per cycle is simply $\delta_R - \delta_O$. While this information is not sufficient to predict a single operating efficiency, operating efficiency mostly depends on hydrogen produced per cycle as long as excess amounts of water is used during oxidation or prohibitively large amount of vacuum pump work are required. Therefore, such measurements are good indicators of whether or not an OSM has the potential for high efficiency without requiring prohibitively low p_{O2} or prohibitively large amounts of water to oxidize. Furthermore, such information can be collected in a couple of days, enabling many materials to be screened more quickly.

By limiting the hydrogen to water ratios to reasonable values (less than 100 as predicted by the results of chapter 2), materials can be first screened by determining the hydrogen production per cycle from a pair of thermogravimetric measurements. Next, promising materials can be further studied by determining a partial δ maps and predicting a single efficiency. This approach allows many materials to be screen quickly while also collecting more detailed information the NRC efficiencies possible with these materials. This experimental screening will be discuss in detail in Chapter 4 and applied to a class of perovskite material in Chapter 5.

CHAPTER 3

THERMOGRAVIMETRIC EXPERIMENTAL SETUP

Thermogravimetric analysis (TGA) is a method for measuring mass change of a sample under specific temperatures and gaseous atmospheres. The mass changes of interest can result from a chemical reaction or phase change. Such measurements are well suited for determining the off-stoichiometry of OSMs under conditions of interest (δ_R and δ_O). This chapter will review the specific equipment and experiential procedure used to evaluate new OSMs. Additionally, instrument calibration, error, testing considerations, and limitations will be discussed.

Off-Stoichiometry

The value of δ quantifies the number of oxygen vacancies present in a nonstoichiometric OSM. The difference in the number of vacancies present in an OSM after step 1 (reduction) and at the end of step 2 (oxidation) determines the OSC of an OSM and hydrogen produced per cycle. Cycle efficiency is strongly dependent on the hydrogen produced per cycle. Additional, δ as a function of p_{O2} and T is a required input of the model described in Chapter 2. Thus, the evaluation of δ under the conditions for each NRC step is of critical importance for screening OSMs. Specifically, the off-stoichiometric map of δ for values of p_{O_2} at the T_L isotherm is used to calculate the water needed for oxidation.

In the case of ceria (CeO_2), $2-\delta$ represents the oxygen sublattice sites that are occupied by oxygen atoms; a change in δ can be observed as a change in the mass of the OSM. For any OSM, as δ grows, oxygen atoms leave the lattice and combine to form

diatomic oxygen gas molecules. For every mole of oxygen leaving the OSM, the OSM mass reduces by the molar mass of atomic oxygen (16 grams per mole). For a given OSM, δ is determined from ΔH , ΔS , p_{O2} , and T through Eq.(1.8). However, by measuring the mass change of an OSM between two different temperatures or between two different p_{O2} the change in δ can be determined through TGA without the knowledge of ΔH and ΔS.

Microbalance and Furnace

The experimental data for this thesis was collected using a commercially available Netzsch STA 449 F3 Jupiter® TGA. This instrument consists of a micro-gram resolution scale and two interchangeable furnaces, a high temperature furnace and a water vapor furnace. The high temperatures needed for step 1 of a NRC require the high temperature graphite furnace be used to evaluate δ_R . The water vapor furnace is used during oxidation test (evaluating δ_O) where the required temperatures are lower but a water vapor atmosphere is needed. An image of the TGA is shown below.

Figure 3.1: Image of thermogravimetric setup and gas handling test setup.

The high temperature furnace utilizes a graphite heating element to achieve temperatures as high as 1650°C and heating rates of 50°C/min. An alumina protective tube separates the volume containing the sample from the volume containing the furnace heating element. This tubing allows the volume containing the furnace element to be purged with argon, preventing the oxidation and destruction of the graphite heating element. For redox testing, this separation is needed because the volume containing the sample is exposed to oxidizing atmospheres in some instances and must be separated from the volume containing the heating element. The 1650°C upper temperature limit is determined from the melting point of the alumina protective tubing (2072°C). A cross-sectional view of the TGA microbalance stand and high temperature furnace is shown below.

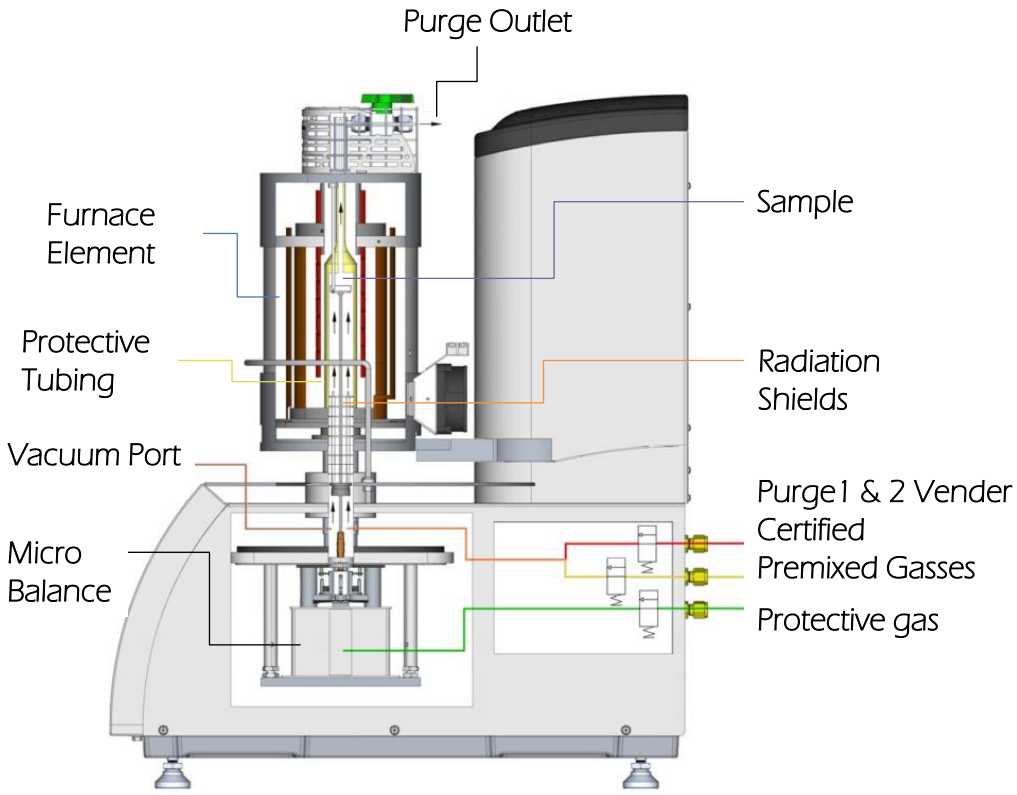

Figure 3.2: Cross section of TG 449 F3 Jupiter Thermo-Microbalance and high temperature Furnace.

For the high temperature furnace, two purge gasses are implemented, a low p_{O2} gas used for reduction (pure argon or premixed oxygen with argon) and a high p_{O2} gas which is used to oxidize the sample (premixed 21% oxygen balanced in argon). These gases enter through a flange connecting the furnace to the microbalance and flow up through the hot zone of the furnace, over the sample before exit at the top of the furnace. For experiments with both the high temperature furnace and water vapor furnace, a protective gas is used to prevent particulates from falling into the microbalance. This gas flows into the volume containing the microbalance and then up through the connection

flange and into the furnace. For experiments with the p_{O2} is controlled by a pre-mixed oxygen-argon gas, the protective gas is of the same composition as the purge gasses. For experiments when the p_{O2} is controlled through the mixing of buffer gasses (water vapor and hydrogen), the protective gas is inert argon.

The water vapor furnace uses a conventional kanthal heating element; therefore the maximum temperature is lower (1250°C). However, it is designed to prevent the water vapor purge gases from condensing during testing and destroying the exposed microbalance electrical components. A cross-sectional view of the water vapor furnace is shown below.

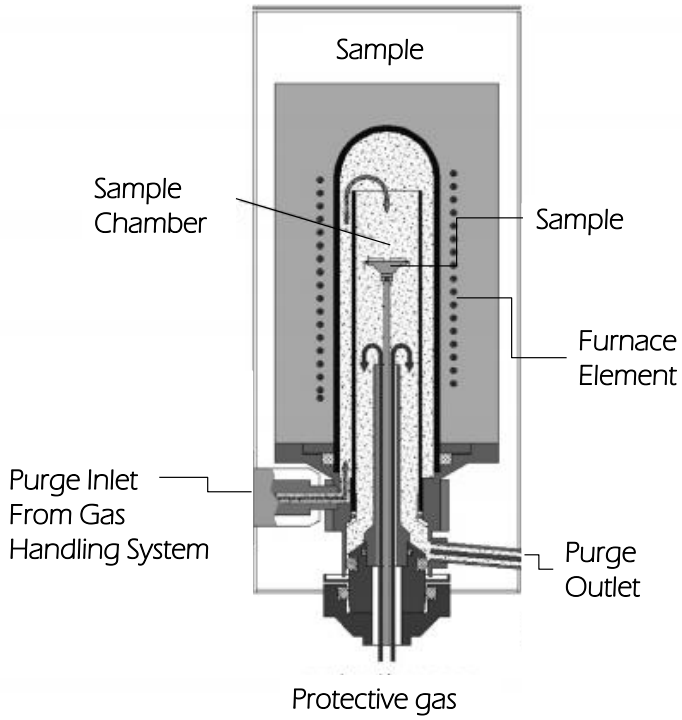

Figure 3.3: Cross sectional view of water vapor furnace.

For the water vapor furnace, the purge gases are produced and controlled by the auxiliary gas handling system. These gases enter at the bottom of the furnace, traveling to the top of the sample chamber through an annular space where they are preheated to the testing temperature. The gasses flow downward past the sample to the gas outlet at the bottom of the furnace. The purge gasses of the water vapor furnace flow in the opposite direction as the gas flow of the graphite furnace. For testing with the water vapor furnace, the protective gas flows through a small tube which exhausts into the furnace at a location that is higher than the lowest point in the sample chamber. This protective gas prevents purge gases (containing water vapor) from flowing into the microbalance chamber where they could condense and damage the scale electrical components.

Sample Temperature

Eq. (1.8) and Figure 1.3 demonstrate how δ of a given material is determined by both temperature and p_{O2}. Hence, controlling and measuring these two parameters are paramount for accurate measurements of δ. Figure 3.4 depicts the typical crucible and OSM sample used during TGA testing. Here, OSM is applied as a thin layer of finely ground powder (less than 1mm, created with agate mortar and pestle) which sits atop a thin layer of platinum foil. The motivation for this sample geometry will be discussed later in this chapter. Platinum foil is used as a reaction barrier for the OSM and Alumina plate which supports the sample. At the high temperature required for reduction testing, ceria and aluminum containing perovskites will react with alumina. However, platinum is inert to these materials at the temperatures of interest and is employed to prevent any reaction between the sample and alumina plate. Directly underneath the alumina plate is

an “S” type thermocouple. This thermocouple, in conjunction with the furnace heating element, is used to monitor and control the temperature of the sample.

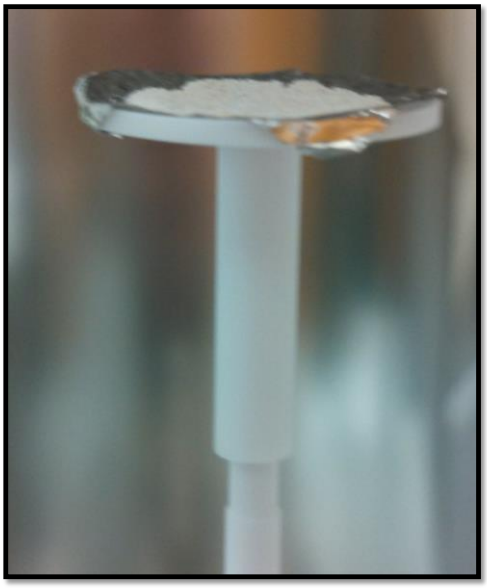

Figure 3.4: Image of curable, platinum foil, and sampled powder used during TGA testing.

The S type thermocouple is in direct contact with the alumina plate. Furthermore, for each test, the system is allowed to equilibrate for several hours. Therefore, the temperature of this thermocouple is taken to be the temperature of the sample. This temperature is measured and recorded for all experiments. The thermocouple measurements are also used to set the temperature of the OSM to a specific value of interest for a given experiment. From this point forward, this temperature will be referred to as the sample temperature.

The calibration of this thermocouple is performed by measuring the melting point of five pure metal samples for which the melting temperature is well known. First, a ~20 mg pure metal sample is heated at a constant heating rate up to and past the material

melting point. Next, the sample cooled back down below the melting point. As the sample reaches the melting point, the latent heat of fusion absorbs energy. The energy absorbed by the sample's phase change reduces the rate of change in the measured sample temperature. By calculating the time derivative of the sample temperature, the melting event can be observed as a sharp change on the plot of the derivative of sample temperature vs. time (Figure 3.5 below). For each calibration sample, the melting point was measured three times. The last two measurements were averaged and taken as the measured melting point. This was done to eliminate the effect of sample geometry on the melting point of the sample. These measured melting temperatures are input into the Proteus® software provided by Netzsch and fit with a polynomial curve which is used as the calibration equation for this thermocouple. This equation was used to calculate the actual sample temperature from the measured sample temperature. However, this fitted equation does not reproduce the known melting temperatures of the pure metal samples due to the inability to fit the polynomial expression the experimental data exactly. The error resulting from this imperfect fit is shown in Figure 3.6 for each calibration sample. Here, the maximum error for the temperature range explored and samples tested was found to be 2.3°C. The melting point measurements in combination with the calculated melting points from the polynomial expression are given in Table 3.1.

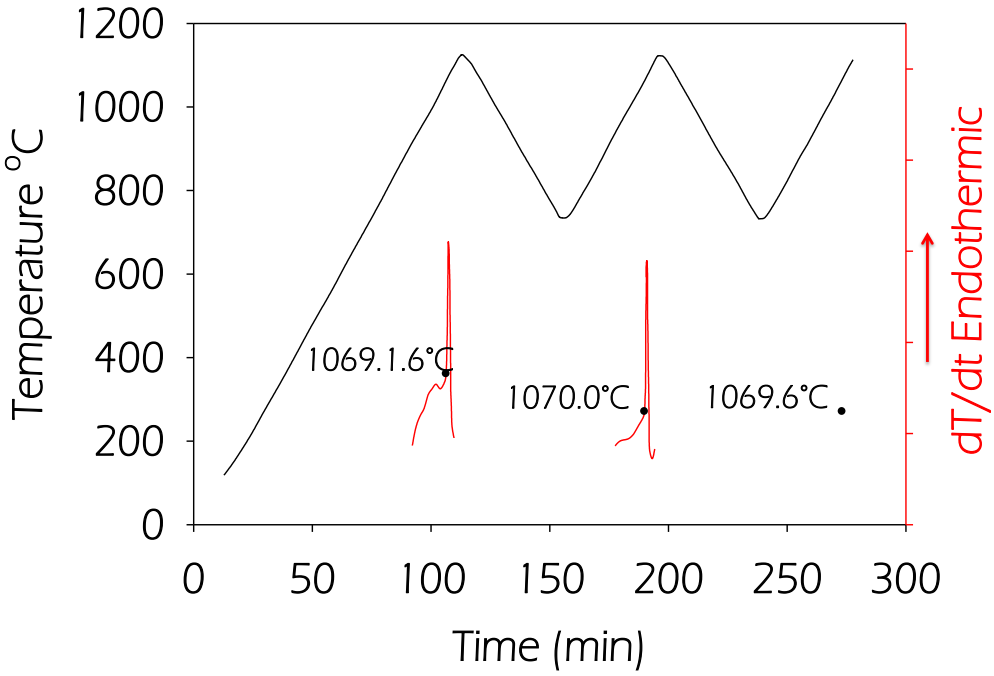

Figure 3.5: Temperature calibration measurements with gold. The continuous black curve is the sample temperature throughout the test (3 melting events). The 3 red curves are the absolute values of the derivative of the temperature profile during each melting event. The onsets of each sharp spike correspond to each melting event respectively.

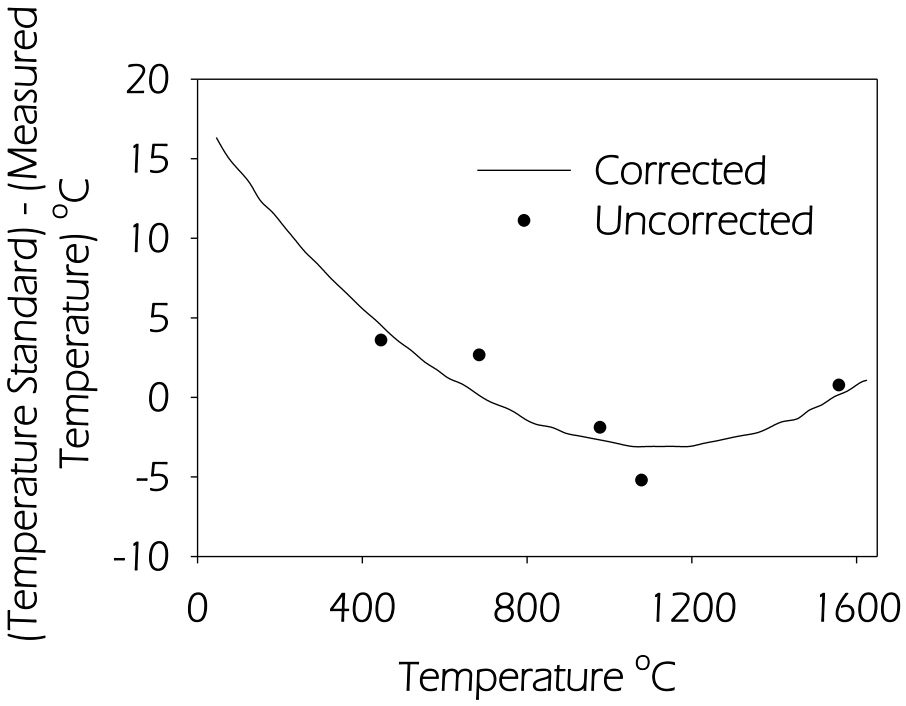

Figure 3.6: Error verses temperature for the calibrated measurements of sample thermocouple.

Table 3.1: Calibration data for S type thermocouple used to monitor and control the sample temperature of the OSM during TGA testing.

Material	Nominal Melting Temperature	Measured Melting Temperature	Corrected Melting Temperature
Zn	419.5	416.3	420.7
Al	660.3	658.0	658.0
Ag	961.8	964.0	961.1
Au	1064.2	1069.8	1066.5
Pd	1555.2	1554.9	1554.7

Experimental Oxygen Partial Pressure

Specifically designed for detailed redox reaction analysis, the auxiliary gas handling and monitoring equipment enables high resolution control of the oxygen partial pressure of the bulk gas inside the furnace. By controlled mixing of buffer gasses, this equipment enables testing under controlled oxygen partial pressures ranging from 1-10^{-25} atm at high temperatures. Combined, the TGA and auxiliary gas handling equipment is used to screen each OSM's potential for high performance in a NRC.

As previously described, controlling and monitoring p_{O2} is required for obtaining accurate measurements of δ. For reduction testing in the high temperature furnace, the value of p_{O2} is typically limited to values above 10^{-6} atm simply because lower oxygen partial pressures are difficult to reach with inert purge gasses alone due to leaks in the system and the required low purge gas flow rates. When screening new OSMs, previous work has often used scientific grade inert gases (He, N_2, or Ar) for reduction which has an oxygen partial pressure of approximately 10^{-6} atm. Therefore, two different values of p_{O2} are used for the reduction testing described herein. A p_{O2} value of 10^{-5} atm was

selected for convenience because a pure inert gas can be used to achieve this this value of p_{O2}. Furthermore, values at this p_{O2} are similar to the values in previous work. However, because the OSC measured between reduction and oxidation will be used to screen OSMs, a value of $p_{O2}=10^{-3}$ atm was selected to comply with the results from chapter 2, where values of p_{O2} less than 10^{-3} atm result in low vacuum pump efficiencies and small NRC system efficiencies.

To achieve both of these values of p_{O2} during TGA reduction measurements, vender certified gases were purchased and used as purge gases with flow rates of approximately 100 mL/min. The thermo-microbalance utilizes three internal mass flow controllers (MFCs) to control the flow of the two purge gasses and the protective gas.

During oxidation, both hydrogen and oxygen are present in the reactor. This hydrogen gas creates a reducing environment with a very low p_{O2}. To produce the low p_{O2} atmosphere needed to determine δ during oxidation, a gas handling system was constructed to mix the buffer gases at controlled rates (water vapor and hydrogen). A schematic of the TGA and auxiliary gas handling system is shown below.

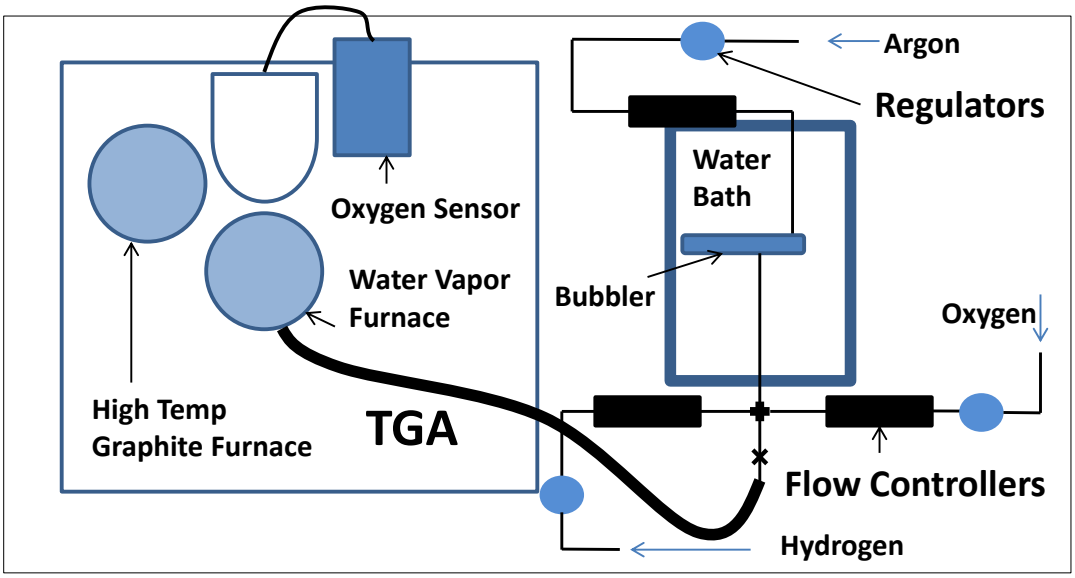

Figure 3.7: Schematic of TGA and gas handling system.

.

This system is composed of three regulators, three external MFCs used to mix the gases, a bubbler to saturate the pure argon purge gas with water, and a temperature controlled water bath used to fix the temperature of the bubbler. To produce the water vapor/hydrogen mixture, argon is first bubbled through water at a controlled temperature. Controlling the bubbler temperature facilitates the regulation of the saturation pressure. By regulating the saturation pressure and argon flow rate, the amount of water entering the system can be controlled with high resolution. This saturated argon stream is then mixed with a vendor certified mixture of hydrogen and argon at different premixed concentrations of hydrogen. The result is a gas containing a specified water to hydrogen ratio. This gas is then delivered to the water vapor furnace (Figure 3.3) via a heated line to prevent the water from condensing, which would alter the water to hydrogen ratio. The system is capable of achieving hydrogen to water vapor ratios ranging from 1:50 to 1000:1 (e.g. 0.02-1,000). These limits are a direct result of the maximum total flow rate

allowed by the microbalance (100-150 mL/min) and the minimum flow rate that can be accurately controlled by the MFC's (0.5 mL/min). Initial testing indicated that higher flow rates disturbed the microbalance, which decreases the repeatability observed in the TGA signal. After mixing, these two buffer gasses react through Eq. (4.1) to produce an equilibrium p_{O2} defined by this reaction's equilibrium constant as shown in Eq. (4.2). The value of p_{O2} achievable by this setup at different temperatures is shown in Figure 3.8. For the experiments describe here, an additional third gas is used independently of the other gases to oxidize the samples (discussed previously in Chapter 3).

$$H_2 + \tfrac{1}{2} O_2 \rightarrow H_2O \tag{4.1}$$

$$K_{ws} = \frac{\left(P_{H_2}\right)\left(P_{O_2}^{1/2}\right)}{P_{H_2O}} = \frac{P_{O_2}^{1/2}}{R_{H_2O}} \tag{4.2}$$

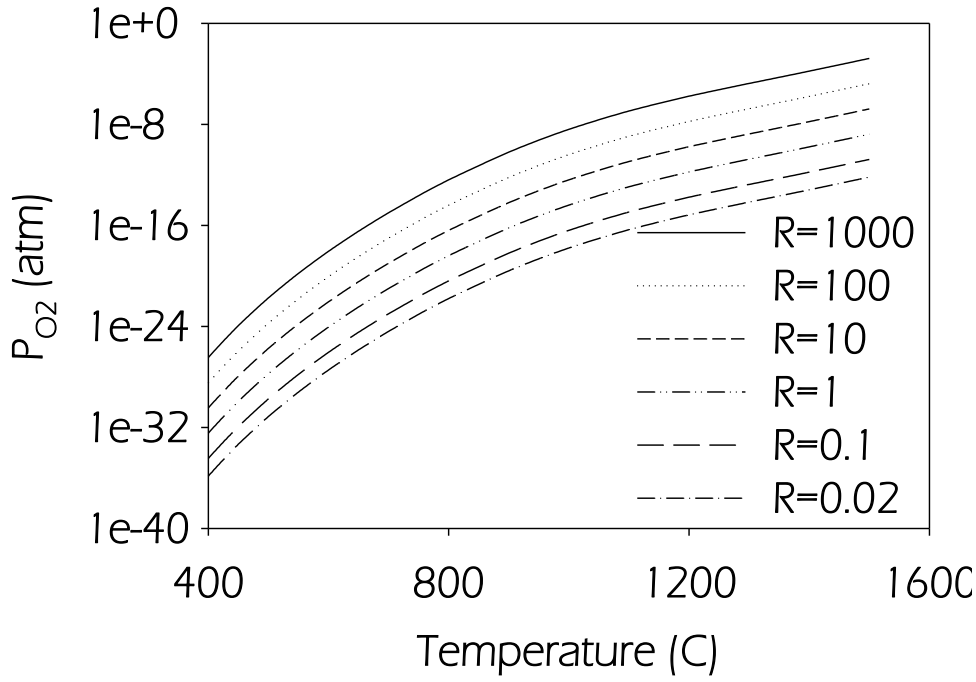

Figure 3.8: Accessible values of p_{O2} vs. temperature by mixing buffer gases with gas handling system.

For both oxidation and reduction, the established p_{O2} was measured and recorded by a commercially available Zirox ZR5® oxygen sensor attached to the exhaust of the TGA. This sensor has two chemically inert electrodes on each side of a yttrium stabilized zirconia cell heated to 750°C. At elevated temperatures the stabilized zirconia is conductive to oxygen ions and the voltage (V) across the cell is proportional to the difference in oxygen partial pressure on each side of the cell according to the Nernst equation, shown below in Eq. (4.3) . Here F is Faradays constant. With the reference electrode exposed to atmospheric air (0.21 atm of oxygen) and the internal electrode exposed to the effluent gasses of the experiment, the cell voltage can be monitored. This voltage is proportional to the value of p_{O2} of the effluent gasses recorded throughout testing in order to verify the desired value of p_{O2} is established by the premixed gas.

Furthermore, for oxidation testing, the measured value of p_{O2} can be used to calculate the value of R_{H2O} of the effluent gas through Eq. (4.2) where the equilibrium constant is found at the temperature of the sensor (750°C).

$$V = \frac{RT}{4F} \log\left(\frac{p_{O_2}^1}{p_{O_2}^2} \right) \tag{4.3}$$

Thermogravimetric Testing Procedure

For a typical test, clean platinum foil was placed on a scale and tared. For new perovskite samples, 60-150 mg was used for testing. Next, the sample is placed on the platinum foil and the mass is measured and recorded. The sample is spread out in a very thin layer. This sample geometry is used to maximize the sample surface area as seen by the purge gas which increases oxygen diffusion from the sample to the bulk gas, decreasing equilibration time. The sample and platinum foil is then loaded into the TGA where it is heated to the temperature of interest under the desired value of p_{O2}. This temperature and atmosphere is maintained for five hours while the sample mass decreases and slowly equilibrates. Next, the low p_{O2} environment is replaced by 21% oxygen balanced in argon and the sample oxidizes, gaining mass. The sample is allowed to equilibrate for thirty-five minutes in the high oxygen environment. Unlike during sample reduction where the generated oxygen gas significantly increases the p_{O2} of the atmosphere, during oxidation the amount of oxygen absorbed by the sample has negligible impact on the value of p_{O2} of the 21% oxygen environment. The result is much faster equilibration times for oxidation compared to reduction. Finally the sample is cooled to a reference temperature which is used to calculate the mass change between the

reduction condition (T_H and p_{O2}) and a reference condition (T_L and 21% oxygen). Next, the testing profile is repeated with empty platinum foil (this is known as the baseline test). Even during the baseline run, which only includes the empty Al_2O_3 plate and the platinum foil, mass changes can be observed on the TG signal in Figure 3.9. These changes in the measured mass are caused by effects of buoyancy and drag. Initially, as the temperature of the furnace and gases increase, the gas density surrounding the Al_2O_3 plate decreases. This decreases the buoyant forces acting upwards on the crucible, causing the mass to increase slightly (mass gain 1, Figure 3.9). However, the MFC, which controls the volumetric flow rate of the purge gas is set to a constant value, and is outside the furnace, at a constant temperature. Therefore the molar flow rate of this gas is also constant. As the temperature of the gas continues to rise, the volumetric flow rate of the gas in the hot zone of the furnace grows larger, resulting in an increased drag force on the Al_2O_3 plate. For the high temperature furnace, the purge gasses flow from the bottom of the furnace to the top of the furnace and the drag force acts upward on the crucible. As the drag force increases, the TG measures a mass loss (mass loss 2 Figure 3.9). After the temperature of the sample and furnace reaches steady state, the TG signal stabilizes and no mass change is observed. Finally, at 350 minutes the purge gas is switched from argon and 21% oxygen balanced in argon to pure argon. Here, argon is a heaver gas than oxygen and at the same velocities, the force from drag for argon will be larger than that of the oxygen/argon mixture. Again, because the force from drag lifts the crucible upwards, when the gases switch, a mass increase is observed (mass gain 3, Figure 3.9). These measured mass changes caused by drag and buoyancy are also present in the sample run, but combined with the mass changes of the sample resulting from reduction

(mass loss 4) and oxidation (mass gain 5 and 6). To correct for these mass changes not associated with the sample itself, the baseline is subtracted from the sample run. The remaining mass loss observed on the TGA signal is caused only by the sample. An example of the baseline and sample run is shown in Figure 3.9. Again, the non-zero values of the baseline are the effects of buoyancy on the microbalance which result from changing the temperature or gaseous atmosphere.

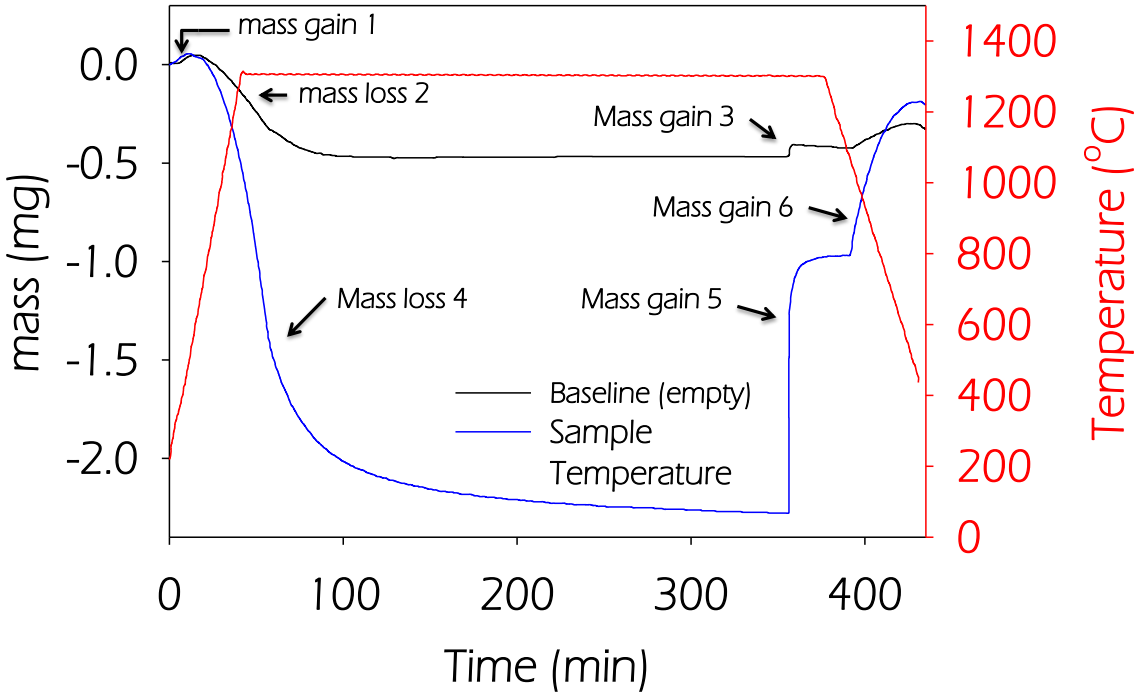

Figure 3.9: Example baseline (black) and sample (blue) TGA measurement for $(Sr_{0.8}La_{0.2})(Al_{0.25}Ga_{0.25}Mn_{0.5})O_3$. The measured temperature of the sample is shown in red.

The corrected mass loss data is shown in Figure 3.10 (sample measurement minus baseline measurement). The first large mass gain (around 350 minutes) is the sample oxidizing upon changing the p_{O2} of the environment. The second mass gain of the sample

is further oxidation which occurs from reducing the temperature under the constant 21% oxygen environment.

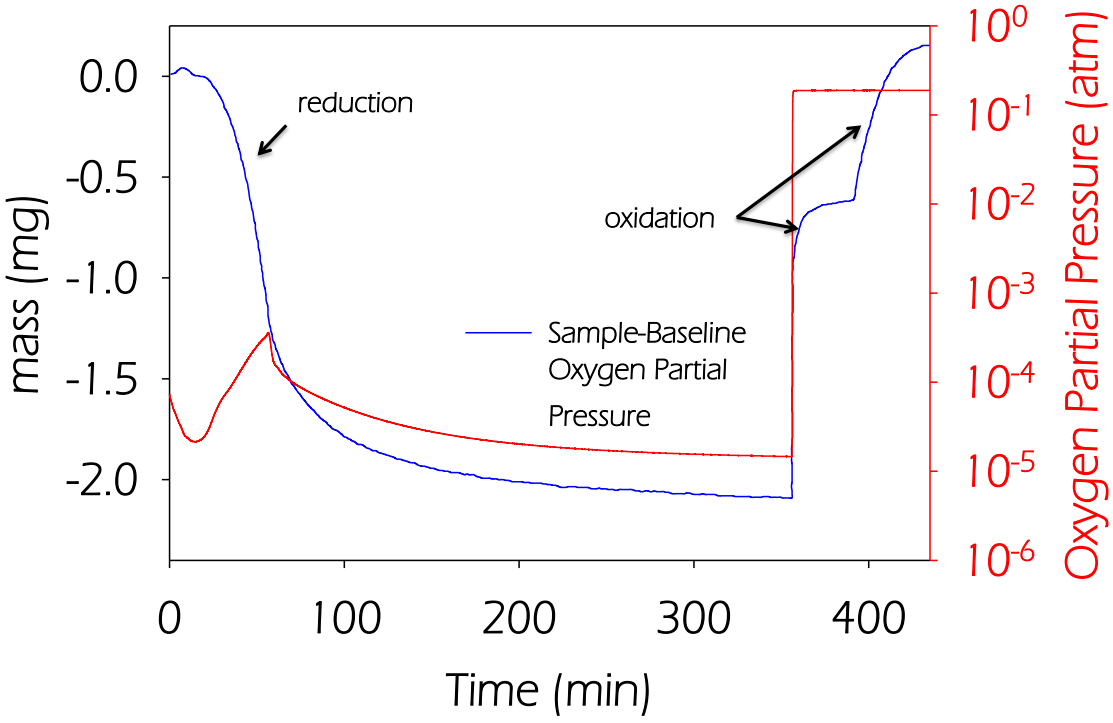

Figure 3.10: Corrected TGA measurement (sample minus baseline) for $(Sr_{0.8}La_{0.2})(Al_{0.25}Ga_{0.25}Mn_{0.5})O_3$, shown in blue. Measured oxygen partial pressure shown in red.

To calculate δ from the mass change measurement through TGA (as shown in Figure 3.10), the mass change is normalized by the total mass of the sample (Eq. (4.4)) . $\delta_R - \delta_{ref}$ is the change in off-stoichiometry of the OSM between the reduction condition and the reference condition ($T = 500$°C and p_{O2}=0.21 atm). $\delta_R - \delta_{ref}$ is found through the ratio of the OSM molar mass to oxygen's molar mass according to Eq. (4.5). Here, MM_{O_2} and MM_{OSM} are the molar masses of oxygen and the OSM respectively.

$$\%\ mass\ change = \frac{mass\ change\ (mg)}{total\ sample\ mass\ (mg)} \tag{4.4}$$

$$\delta_R - \delta_{ref} = \%\ mass\ change \times \frac{MM_{O_2}}{MM_{OSM}} \tag{4.5}$$

In a second thermogravimetric experiment the mass change between the reference oxidation condition and the reference condition are measured in a similar manner. This allows the hydrogen produced per cycle to be calculated through the equation below.

$$n_{H_2} = \delta_R - \delta_O = \left(\delta_R - \delta_{ref}\right) - \left(\delta_O - \delta_{ref}\right) \tag{4.6}$$

Microbalance Drift

Due to the nature of oxidation/reduction mass loss measurements which require the resolution of small mass losses and long equilibration times, microbalance drift can become a significant source of error. Equilibration times are determined by the purge gas flow rate and amount of oxygen released by the sample. Initially, when a sample begins to reduce, it generates oxygen gas. This oxygen is released to the bulk gas of the TGA

furnace where it increases the local $p_{O2.}$ However, the generated oxygen must be removed and the local value of p_{O2} lowered before the sample can reduce further. This is achieved with an inert purge gas and the limitation of bulk gas diffusion was validated by testing under different inert purge gas flow rate. As the gas flow rate increased, equilibration times decreased, indicating that solid-state diffusion of oxygen through the OSM is not the rate limiting step. However, microbalance stability places an upper limit on the purge gas flow rate (approximately 150 mL/min) resulting in a significant dwell time required to remove the oxygen generated by the sample. This situation causes very long equilibration times observed in Figure 3.9 and Figure 3.10. On the other hand, oxidation does not require long equilibration times because, unlike reduction, the oxygen consumed by the sample during oxidation is a very small portion of the oxygen present in the TGA. Therefore, the local p_{O2} remains relatively constant throughout oxidation and the equilibration time required for oxidation is small relative to the time required for reduction (Figure 3.9 and Figure 3.10). Errors from microbalance drift accumulate with time, meaning that mass changes that take a long time to equilibrate will have a large measurement error from drift. For this reason all mass change measurements were conducted during oxidation rather than reduction to take advantage of the short equilibration time. Furthermore, because the sample must be oxidized at the end of the experiment, only one mass change measurement was conducted per test. This minimizes the time between the equilibrated mass loss and the equilibrated oxidized reference mass. Figure 3.11 and Figure 3.12 are two plots identical to Figure 3.9 and Figure 3.10, except for the first iteration of the reduction testing temperature profile which was designed to measure multiple mass losses in a single measurement.

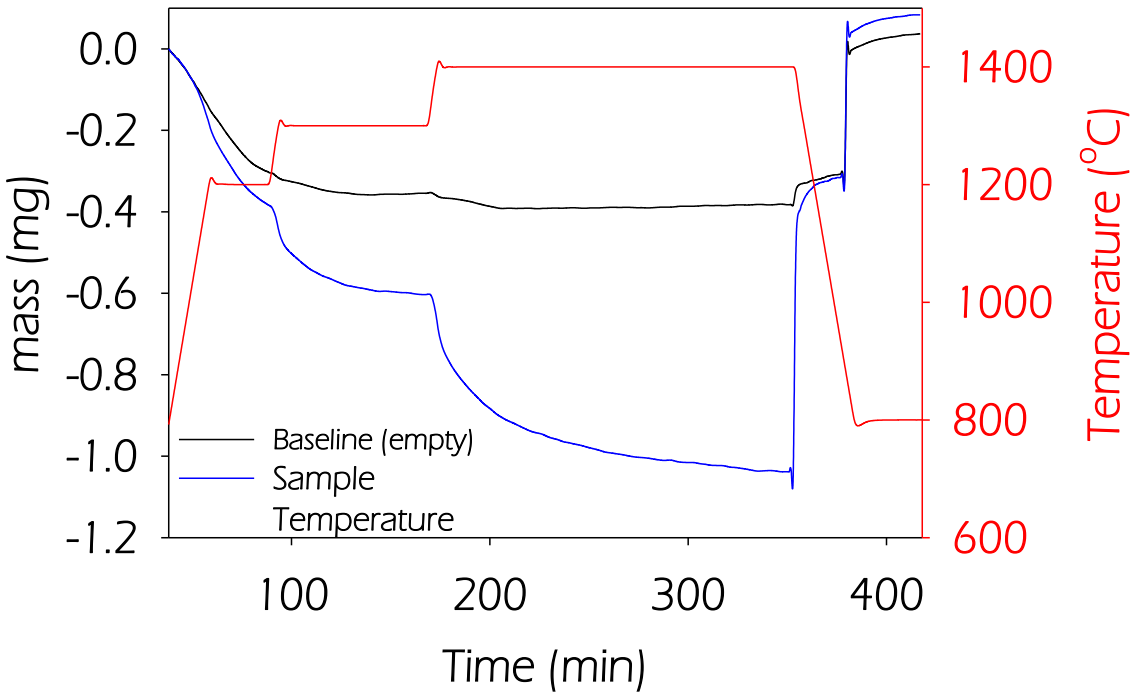

Figure 3.11: Baseline (black) and sample (blue) TGA measurement for ceria under the first attempted temperature profile. The measured temperature of the sample is shown in red.

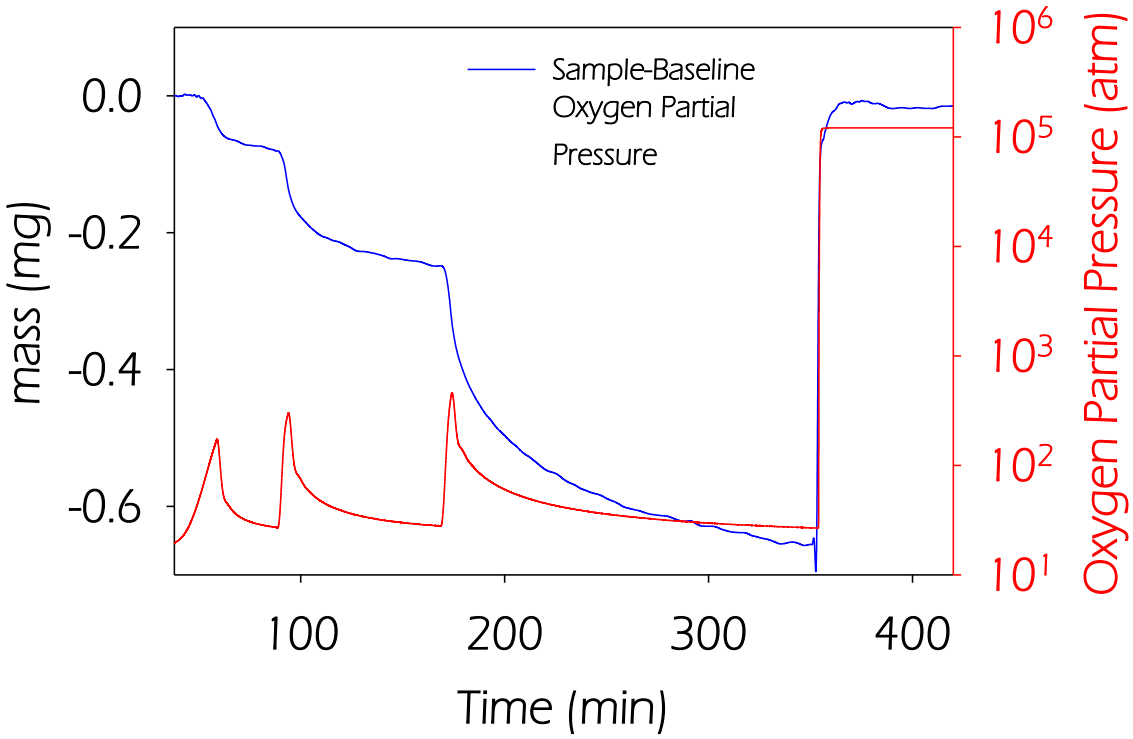

Figure 3.12 Corrected TGA measurement (sample minus baseline) for ceria under first attempted temperature profile, shown in blue. Measured oxygen partial pressure shown in red.

The objective of the test shown above was to obtain mass loss measurements under approximately 10 ppm p_{O2} at 1200ºC, 1300ºC, and 1400ºC. However, the data above has three coupled issues. First, during all isotherms, equilibrium is not reached and the mass of the sample is still decreasing at a substantial rate. This problem is resolved by implementing either longer isotherm dwell times or smaller sample masses. With smaller total masses, less oxygen is generated during reduction and the required isotherm dwell time to sweep the generated oxygen away also decreases. Second, because the mass loss measurement is made with reference to the oxidized mass after oxygen is introduced to the system (at 350 minutes), the time between the end of the first isotherm (1200°C) and

this reference mass measurement (80 min) can be several hours. Therefore, error from microbalance drift accumulates over this time. Drift for this instrument was measured to be 5.5 μg/hour. For the data of Figure 3.12 at 1200ºC, the mass change is 80 μg and equilibrium at this condition is established more than four hours before the reference mass is measured. This causes the errors from microbalance drift alone to accumulate over four hours. Increasing the mass will increase the measured mass change, but it will also increase the isotherm dwell time (leading to no improvement in the signal to noise ratio). Furthermore, because at 1200ºC, 1300°C, and 1400ºC measurements are made with the same mass, all isotherm dwell times must increase, further increasing the error from drift. This error is mitigated by oxidizing the sample directly after reduction to minimize the time between the mass change and reference mass measurements. Therefore, only one isotherm was used for each test to minimized microbalance drift (as shown in Figure 3.10).

Temperature stability of the microbalance is necessary to make repeatable TGA measurements along with minimizing error from microbalance drift. Microbalance stability is achieved by a temperature controlled water loop in contact with the scale. The sensible heat transferred to the scale from the high temperature furnace is removed by this coolant loop, and the temperature of this bath is kept slightly above room temperature (approximately 1-2°C) to maintain maximum temperature stability and prevent condensation of water on the microbalance.

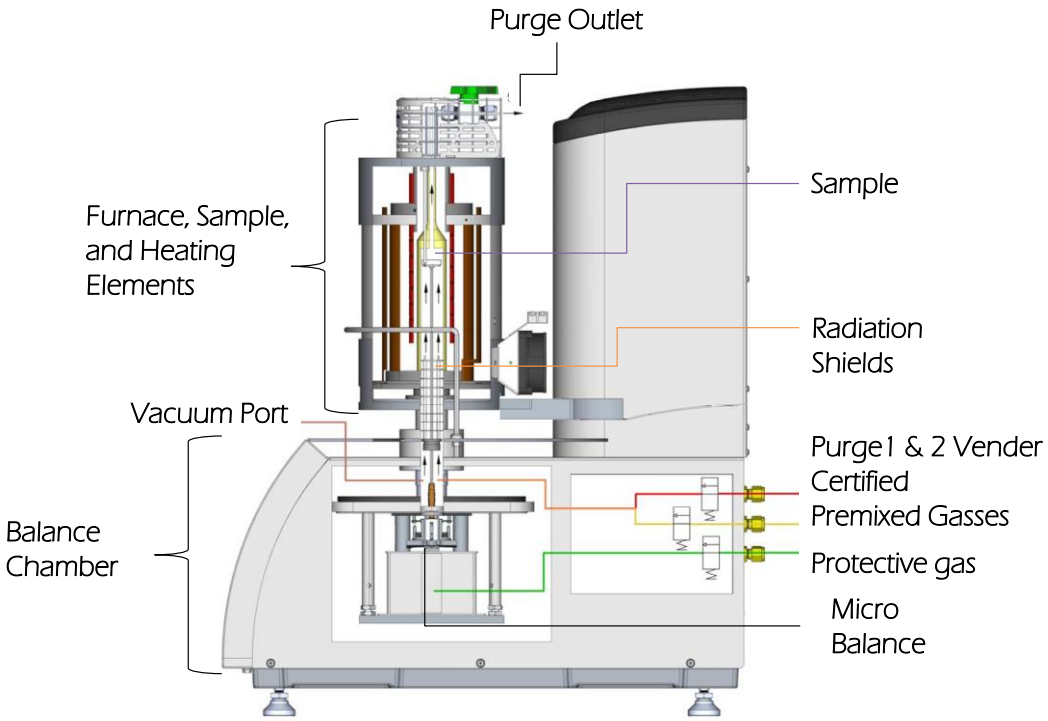

Figure 3.13 Cross section of TG 449 F3 Jupiter Thermo-Microbalance and high temperature furnace.

Figure 3.13 illustrates how the balance is placed in a separate chamber from the sample and heating elements. To further ensure temperature stability, the heat transfer from the furnace to the scale is minimized by thermally isolating the two chambers. This thermal isolation is achieved with several radiation shields arranged in series during high temperature testing and forced convection created by the protective gas flow. The protective gas flows into the scale chamber over the scale and up through the connection flange. This maintains a slight overpressure on the scale chamber to prevent water vapor and other purge gasses from entering the microbalance. Because this protective gas is in direct contact with the scale, flow rates must be low and the temperature must be

controlled. For all experiments described here, the protective gas flow rate was 20 mL/min, and before entering the port labeled “Protective Gas” of Figure 3.13, the gas temperature was preconditioned by passing the gas through coiled stainless steel tubing submerged in a temperature controlled water bath. This is the same water bath used to control the temperature of the water circulating through the microbalance (1-2ºC above room temperature) ensuring the temperature of this protective gas was very close to the actual temperature of the microbalance, maximizing temperature stability. The protective gas tubing between the water bath and the microbalance was insulated to minimize convective heat loss to the room as the gas flows to the TGA.

Microbalance drift is measured in μg/hour. As discussed previously, for experiments which require prolonged testing times, balance drift can become a significant source of error. Similar to all analog to digital converters, instrument drift can be influenced by numerous external parameters, most commonly, transient microbalance temperature due to the temperature dependence of the physical property being measured (e.g. electrical resistance). To mitigate error contributions from microbalance drift to measurement error, the TGA manufacturer (Netzsch) recommends the water loop and protective gas be allowed to equilibrate for a minimum of two hours before testing. After testing, the water loop and protective gas should remain on at all times, even when no test is running. This ensures the microbalance temperature is stable for future testing. If testing is halted, the water loop and protective gas must be turned on and the instrument must be allowed to reach thermal equilibrium before testing can resume. Additionally, testing times over which the mass gain of interest occurs should be as short as possible to minimize the contribution from drift to measurement error. By only considering the TGA

data during the mass gain of interest, the microbalance drift during the long reduction equilibration isotherm has no contribution to measurement error. Furthermore, because instrument configuration prevents the evacuation and backfill of the TGA multiply times during a test, the TGA cannot be simply programed to run through many temperatures and many different values of p_{O2} over the course of several weeks.

Consideration for Off-Stoichiometric Thermogravimetric Measurements

While TGA is capable of measuring many physical processes and chemical properties, determining the δ of an OSM for NRC requires additional considerations. Specifically, because the OSM only partially reduces, the mass loss can be a very small percentage of the total mass (for ceria at 1300°C and $P_{O_2} = 10^{-3}$, $\delta = 0.0044$ which translates to a mass loss of 0.041%). Depending on the stability and resolution of the microbalance, large sample masses may be required to achieve satisfactory signal to noise ratio. This might suggest using the largest sample mass possible, which can be achieved by replacing the platinum foil of Figure 3.4 with a platinum crucible which has a maximum allowable volume (the maximum volume possible without leaving the hot zone of the furnace or exceeding the maximum sample mass of the microbalance). While this approach is necessary in some situations, exceedingly large sample masses can be problematic. For large sample masses, the thermal mass of the sample can significantly impact the temperature distribution of the bulk gas in the sample chamber. Because the density of gas is temperature dependent, this difference in temperature distribution will alter the effect of buoyancy and drag on the TGA signal between the baseline and sample run. This effect can be observed in the figure below.

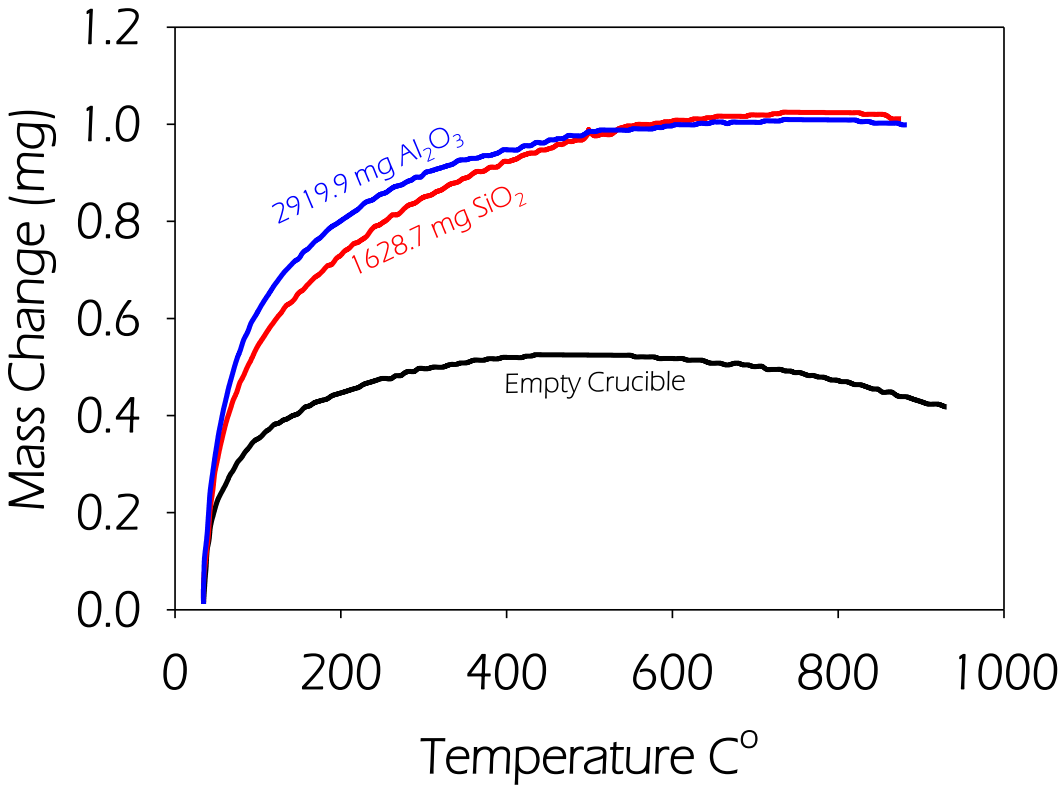

Figure 3.14: The effect of buoyance observed while heating inter samples. Uncorrected TGA data for three inert samples heated in air.

In this figure, the three samples examined (empty Al_2O_3 crucible, SiO_2 powder, and Al_2O_3 powder) should all have zero mass loss at the examined temperatures in air. Therefore, if the effects of buoyance and drift are equivalent, the TGA curves will be identical for each sample. However, the total mass and therefore the thermal mass of each sample is very different and how these different thermal masses affect buoyancy and drag can be observed by the difference in the TGA curves.

The only way to avoid this error is to test under a vacuum where effects of buoyancy are mitigated (not possible with the Netzsch TGA), or use an inert material with identical thermal mass as the sample of interest during the baseline measurement.

The second approach requires the specific heat of the sample be known and chemically inert material with similar specific heat as the sample material. These complications motivate the use of smaller sample masses when possible. Effectively, the smaller the off-stoichiometry of the material at conditions of interest, the more difficult the mass loss measurement will be. For the example, above where ceria's mass loss is only 0.041%, to achieve a TGA signal of 100 μg, 2.4 grams of sample are required. This is much larger than the recommended maximum sample mass of 150 mg (recommended by Netzsch to prevent a significate difference in buoyancy resulting from change in thermal mass). With these conditions, an inert material must be used during baseline measurements.

For materials and testing conditions where the off-stoichiometry is large and value of p_{O2} is low, unnecessarily large sample masses can be problematic. In this case, the amount of evolved oxygen can be large by comparison to the volume of gas in the furnace and significantly impact the value of p_{O2} in the bulk gas in the TGA. During reduction, at very low values of p_{O2} (i.e. 10^{-5}) as the sample reduces, oxygen gas evolves. Because low purge gas flow rates are required for balance stability, this evolved oxygen can drastically increase the value of p_{O2} of the bulk gas. These high values of p_{O2} prevent the OSM from reducing further and the evolved oxygen must be swept away before the OSM reduces to is equilibrium state according the value of p_{O2} at the purge gas inlet. This situation makes reduction a serial processes that can require very long dwell times to reach equilibrium. Similar issues also occur during oxidation testing where off-stoichiometry is measured under high water to hydrogen ratio because very few hydrogen atoms are present in the atmosphere, small amounts of evolved oxygen react with the hydrogen, significantly changing the amount of hydrogen in the bulk gas. This can also

significantly impact the p_{O2} of the oxidation atmosphere, leading to long equilibration times.

While long equilibration times are possible, two issues arise. First, long equilibration times cause a single test to take many hours, making screening materials very time consuming. Finally, there is inherent drift in the microbalance (approximately 5.5 μg/hour). Long equilibration times can lead to large values of drift and this can become a significant source of error. However, large accumulated error from drift during long sample runs can be avoided. Because oxidation equilibrates much faster than reduction, errors from drift during testing where the mass change is measured during oxidation are smaller. By measuring the mass change during oxidation alone, the error from drift only accrues during the time required for oxidation. This approach minimizing error from drift will be further discussed in the next section.

Thermogravimetric Testing Error

With these many considerations, a TGA test procedure was developed to minimize testing time and error while maximizing the signal to noise ratio. An isothermal equilibrium time of five hours was chosen so that two experiments could be completed per day. Next, the sample mass was chosen so that thermal mass had minimal effects on buoyancy (less than 150 mg as suggested by Netzsch technicians). Finally, the total sample mass was chosen to maximize the signal to noise ratio. However, because the mass change for new samples is unknown before testing, and targeting a specific value for the total mass change is not possible so nominal values of sample mass were chosen.

The measured TGA signal drift of the microbalance was determined to be 5.5 μg per hour, which is much larger than other sources of error in the system (microbalance

resolution is 1 micro-gram). For the experiments here, the oxidation time was limited to thirty-five minutes, but typically the samples equilibrate in a much shorter time. The time required to oxidize and reach equilibrium was taken to be the oxidation time (shorter oxidation time result in smaller errors from drift). For measurements where the entire oxidation time was used, an expected error from microbalance drift is calculated as 3.2 μg meaning a mass loss of 0.32 mg would result in a signal to noise ratio of one hundred. A mass loss of at least 0.32 mg was targeted for all tests, but predicting mass loss (and therefore the appropriate sample mass) is not possible for a new sample. For the data reported here, the minimum signal measured mass loss was 0.043 mg which results in a signal to noise ratio of greater than 10.

Limitations Thermogravimetric Analysis for Oxygen Storage Materials

Depending on the microbalance, furnace, and gas handling system used, TGA has many limitations when evaluating oxygen storage materials. As previously discussed, for materials with very small mass losses (e.g., OSMs with high ΔH , reducing with a low T_H, or reducing with a high values of p_{O2}), large sample masses can be required. However, when the mass becomes so large that the sample's thermal mass has an impact on the buoyancy and drag seen by the scale during heating and cooling, matching this buoyancy effect during the baseline run becomes difficult and should be avoided. This variation occurs for samples with mass above 150 mg for the TGA setup described herein. When screening materials for high performance OSMs under typical reduction conditions of interest (T_H less than 1600°C and P_{O_2} greater than 10^{-5}), it becomes increasingly difficult to measure the off-stoichiometry of materials with a value of ΔH greater than that of ceria. However, the results of Chapter 2 depict how improved OSMs

have a lower reduction enthalpy than ceria making the TGA setup described here appropriate for measuring the off-stoichiometry high performance OSMs.

Additionally, the possibility of measuring kinetics with the TGA test stand was explored. To measure the kinetics of the reduction and oxidation reaction, the thermodynamic driving potentials for each reaction (temperature or p_{O2}) must be changed quickly so that the reaction is only limited by the reaction kinetics. As previously discussed, for the reduction reaction, long isotherm dwell times are required to equilibrate the sample due to the serial process of removing the oxygen gas generated by reduction with a sweep gas. This process lowers the value of p_{O2} slowly (possibly taking five hours) and is rate limiting for the reduction reaction. The inability to change the value of p_{O2} quickly makes resolving reaction kinetics impossible for OSM reduction via TGA.

On the other hand, for oxidation reaction, the p_{O2} can be changed quickly. After equilibrating under the reducing conditions, the p_{O2} can be increased almost instantly by purging the system with a 21% oxygen balanced in argon gas. However, the oxidizing agent for such a test is oxygen gas rather than steam and the kinetics of oxidation with oxygen can be different than oxidizing with steam. Furthermore, the water vapor furnace is required to oxidize with steam, but has a maximum temperature of 1250°C, making the measurement of oxidation kinetics above 1250°C impossible with this TGA setup. For most experiments herein, T_H is greater than 1250°C and kinetic measurements were not attempted.

Finally, with the Netzsch STA 449 F3 Jupiter simultaneous TGA and differential scanning calorimetric measurements (DSC) are possible. These two simultaneous measurements might suggest the possibility of reducing an OSM while measuring the

energy absorbed by the sample with the aim of calculating the value of ΔH. For OSM characterization, having information about $\Delta H(\delta)$ is very valuable. Chapter 2 discussed how thermochemical conversion efficiency is strongly dependent on this OSM material property. Therefore, a simple method to evaluate $\Delta H(\delta)$ such as calorimetry would be very advantages. Calorimetry can be used to evaluate ΔH for a single value of δ [81]. However, if DSC could be used to determine ΔH as an OSM is gradually reduced and δ is simultaneously measured with TGA, the functional dependence of ΔH on δ could be used with *insitu* measurements of p_{O2} to calculate $\Delta S(\delta)$ through equation (1.8).

With accurate measurements of the total energy absorbed and the oxygen released (collected with DSC and TGA respectively), the reduction enthalpy of the material is simply the energy absorbed per mole of the oxygen released as a function of the off-stoichiometry of the material. As previously discussed, for accurate off-stoichiometry measurements of some materials/conditions, prohibitively large sample masses are required. DSC measures rely on the temperature difference between the sample temperature and a reference thermocouple to measure the temperature change caused by energy absorbed or released by a sample. This temperature change is correlated to the energy absorbed or released by measuring the temperature change of a calibration material (e.g. sapphire for continuous properties measurements such as specific heat and pure metals for measurements of energetic events such as phase change). This correlation is then used to calculate the energy absorbed or released by a sample of interest to the known specific heat or heat of fusion of the reference material. Inherent to these measurements is the need for isothermal sample temperature to ensure temperature dependent properties are resolved. This is achieved by using a very thin layer of sample

powder. Additionally, the heat loss from sample crucible must also be identical between sample and correction runs to validate the correlation. This is achieved by using an enclosed crucible with a lid. Finally, thermal equilibrium between the sample and thermocouple is achieved by maximizing contact between the sample and the thermocouple and minimizing the mass of the sample far from the thermocouple.

These requirements make the measurement of ΔH very difficult with simultaneous TGA and DSC, and impossible for most materials with Netzsch STA 449 F3 Jupiter setup. To maintain good thermal contact with the thermocouple and isothermal sample temperature, a very thin layer of sample must be spread across the bottom of the DSC sample crucible. With the Netzsch STA 449 F3 Jupiter, this geometry limits the mass of the sample to approximately 50 mg of ceria. Due to the small percent mass loss of this material, there is not enough mass to measure off-stoichiometry of ceria. Additionally, the requirement of a lid makes controlling and measuring the p_{O2} exposed to the sample impossible during testing because evolved oxygen is trapped in the crucible. This prevents equilibration of the p_{O2} inside the crucible and the bulk flowing gas. Finally, because the energy needed to increase the temperature of the sample is large compared to the energy required to liberate oxygen, the heat absorbed by endothermic reduction is on the order of the energy absorbed during heating. This absorption requires the OSMs specific heat to be well characterized as a function of δ and temperature. For specific heat measurements conducted with the Netzsch STA 449 F3 Jupiter, accuracy as specified by Netzsch is at best equal to 10-15% using a sapphire standard. This would lead to a 20-30% error after combining specific heat and off-stoichiometric reduction measurements. This value for measurement error is prohibitively large, even if

controlling value of p_{O2} exposed to the sample was possible and enough mass could be used to measure mass loss accurately. Therefore, direct measurements of ΔH were not attempted using DSC.

CHAPTER 4

SCREENING PEROVSKITES OXYGEN STROAGE MATERIALS

Previous reports in literature have shown perovskites to be promising OSMs. However, as discussed in Chapter 3, it is still unclear whether these materials will out preform ceria. In this chapter, many perovskite chemistries are experimentally screened via TGA and the results discussed. Furthermore, while none of these materials are shown to outperform ceria under the conditions explored, the method described in Chapter 2 which evaluates the potential efficiency possible for new materials is illustrated with an example.

Perovskite OSMs

Ceria is a well-known, highly studied material. Its applications include: solid oxide fuel cell electrolyte[82], catalyst for automotive three way catalytic converters[83], an active catalyst support [84], oxygen sensors[85], and as an OSM for NRC's [15, 29, 32, 35, 45]. While ceria has many desirable material properties for NRCs, this OSM's value of ΔH is approximately 460 kJ/mol H_2 [28] - much larger than the enthalpy of water thermolysis (241 kJ/mol H_2). The value of $R_{\Delta H}$ for ceria is about 2 and Figure 2.9 shows how high efficiencies could be achieved with OSMs which have lower values of ΔH . While previous studies have shown that alloying ceria (i.e. zirconium or titanium alloying agents) can modify its value of ΔH [62-65, 67, 86, 87], alloying ceria does not produce an optimum OSM. Zirconium alloyed ceria with concentrations ranging from 19-86% produces an average value of $R_{\Delta H}$ of approximately 1.1 [67], which is too low for a high performance NRC according to Figure 2.9. Furthermore, zirconia alloyed ceria has a lower value of ΔS than pure ceria which reduces this OSM's performance.

Furthermore, alloying ceria with titanium yields a $R_{\Delta H}$ lower than zirconium alloyed ceria. For both of these alloying agents a reduction in ΔH may seem counterintuitive due to the fact that ΔH for both ZrO_2 and TiO_2 is larger than CeO_2. However, the mechanism behind this reduction of ΔH is not related to ΔH of the pure zirconium and titanium oxides, it is a result of the lattice distortion created by the introduction of the alloying element with a smaller atomic radius. This smaller atom allows its nearest neighbor oxygen atoms to relax, reducing the bond length between the alloying metal atom and its neighboring oxygen atoms. When this alloyed ceria is reduced, the energy needed to create the large lattice perturbations caused by an oxygen vacancy is smaller when starting from pre-perturbed alloyed-ceria, compared the perfectly symmetric pure ceria[63]. Therefore, when zirconium or titanium alloyed ceria is reduced, only oxygen atoms that are nearest neighbors to the alloying atom have a lower value of ΔH. After the oxygen atoms with lower ΔH, which are relatively easy to remove, are gone, oxygen atoms not near an alloying atom must be removed to reduce the OSM further. However these oxygen atoms are similar to the oxygen atoms in bulk CeO_2 with a larger value of ΔH. Therefore, alloying ceria causes ΔH to be reduced in a step like manner where only neighboring oxygen atoms of the alloying element have a lower values of ΔH , and the value of ΔH for vacancies without a nearest neighbor alloying atom remain relatively high. This effect can be observed clearly in the experiential work of data Zhou et Al. [67] for zirconium alloyed ceria. In Zhou's report, alloy concentration was controlled between 19-86% but $R_{\Delta H}$ only varied between 0.93-1.20, making ΔH relatively insensitive to alloy level. Furthermore, the options for further improving ΔH of ceria through alloying

are not promising. This is further demonstrated by inspecting ceria's crystal lattice, shown below.

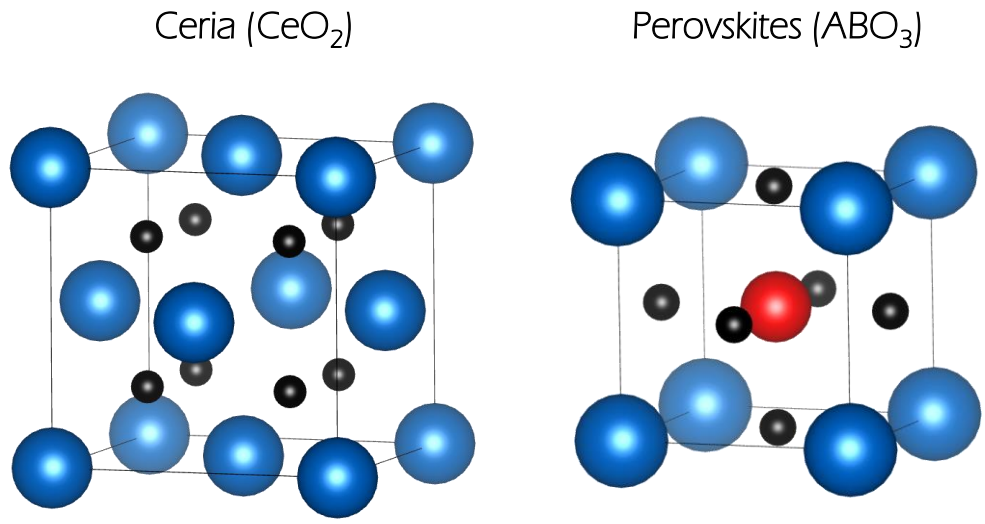

Figure 4.1: Ceria's crystal structure (left) and the perovskite crystal structure (right). Oxygen atoms are shown in black. Metal atoms are shown in red and blue.

For high temperature ceria, alloy agent solubility levels have been shown to be extremely low [88]. Furthermore, there is only one metal sublattice site to alloy, making the variation enabled by alloying limited. Perovskites, on the other hand, can support much higher alloy agent solubility levels and this crystal structure has two metal sub lattice sights to alloy (Figure 4.1). These properties make the perovskite structure more attractive with regards to engineering a material for a specific value of ΔH .

With the goal of screening alloyed La and/or Sr based perovskites for high performance OSMs, many samples were synthesized by sol-gel methods [89-91] by William Cheuh's lab at Stanford University. These samples were screened and

characterized by TGA experiments described in Chapters 3-4 and are presented in the following section.

Perovskite Thermogravimetric Testing Results

The first batch of perovskite samples were screened at values of $T_H = 1300\,°C$, $p_{O2}=10^{-5}$, $T_L = 500\,°C$, and $R_{H2O}=20$. Aiming to implement these new materials in an experimental reactor being constructed here at Georgia Institute of Technology, the reduction temperature (T_H) was selected as a temperature that was attainable by this reactor and below the melting point of these perovskites. This value of p_{O2} was selected mainly out of convenience and in accordance with other reports in literature but is admittedly too high to achieve high efficiencies in a NRC. While this pressure theoretically could be achieved by a vacuum pump in a reactor, the results of Chapter 2 suggest this is likely not an efficient operating condition. The screening value of p_{O2} was later revised according to the results of Chapter 2 to the higher value of $p_{O2}=10^{-3}$. As previously discussed, slow oxidation reaction kinetics could potentially establish the lower limit of T_L. Therefore 500°C was selected as the lower limit for T_L during initial screening.

As described in chapter 4, the difference in off-stoichiometry (δ) of a material between reduction and oxidation describes the OSC or hydrogen produced per cycle ($n_{H_2} = \delta_R - \delta_O$). This parameter is a strong indicator of OSM performance because it describes the moles of hydrogen produced per mole of OSM. For stationary power production or fuel refinement, weight is typically not a limiting factor driving design. However for NRC reactors, the OSM which can be cycled is limited by the amount of

OSM that can be utilized in the reactor. This could be as much as a solid OSM monolith in a pack bed reacted or as little as a thin layer deposited on a surface. In either case, volume limits the amount of OSM that can be used in a given cycle. Therefore, the hydrogen produced per unit volume of OSM (energy density) is a better metric of comparison. Furthermore, this value can be converted to the familiar form of energy density through the equation below. Where ρ^{atomic} is the atomic density of the OSM in m^3 per mole. The atomic density for a perovskite is approximated from the average atomic radius of the 12 coordinated A site through Eq. (5.2), where A_c is Avogadro's constant.

$$energy\ density\left(\frac{MJ}{m^3}\right) = n_{H_2} \times \frac{HHV_{H_2}}{\rho^{atomic}} \tag{5.1}$$

$$\rho^{atomic} = \left(\frac{2\left(r^{A\ site}\right) + 2\left(r^{O_2}\right)}{\sqrt{2}}\right)^3 \times A_C \tag{5.2}$$

The results of the first screening are shown below

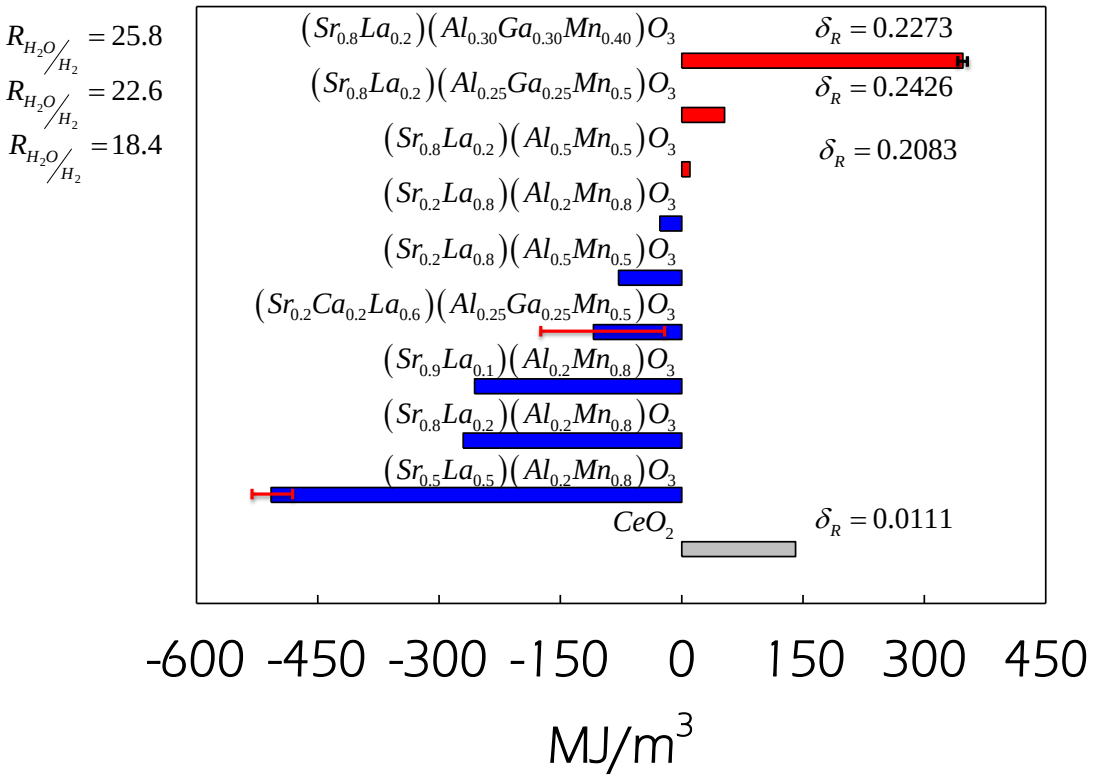

Figure 4.2: Results of the initial screening of perovskite OSMs. Reduction conditions: T_H =1300°C and p_{O2}=10^{-5} atm. Oxidation conditions: T_L =500°C and R_{H2O}=20. The measured equilibrium water to hydrogen ration and achieved off-stoichiometry during reduction is listed on the left and right respectively for materials of interest. For measurements which were repeated, deviations in the results are shown with error bars.

For many of the OSMs in Figure 4.2, n_{H_2} is negative, meaning these materials reduced further during oxidation than reduction. If such materials were used for water splitting, a value of R_{H2O} higher than 20 would be required to oxidize the OSM. As Figure 2.11 shows, excessively large amounts of water can result in poor NRC efficiencies. However, three of the screened OSMs did have a positive value of n_{H_2} and were able to oxidize to some degree. Furthermore, the magnitude of n_{H_2} for

$(Sr_{0.8}La_{0.2})(Al_{0.30}Ga_{0.30}Mn_{0.40})O_3$ was comparable to that of CeO_2, and δ_R was much larger than that of ceria. Because ceria oxidized near completion for conditions of Figure 4.2, higher water to hydrogen ratios will not increase performance. On the other hand, the value of δ_O for $(Sr_{0.8}La_{0.2})(Al_{0.30}Ga_{0.30}Mn_{0.40})O_3$ in Figure 4.2 is 0.1871 and this material will oxidize further at higher water to hydrogen ratios, warranting further investigation of this material.

With the simulation results of Chapter 2 and the experimental results of Figure 4.2, a second screening of perovskite material was conducted (Figure 4.3). In order to reduce under conditions similar to the optimum conditions predicted by Chapter 2 the value of p_{O2} during reduction was increased to $p_{O2}=10^{-3}$ in accordance with Figure 2.10. Additionally, the latter three of the perovskite samples melted during heat treatment at 1350°C. Therefore, the reduction temperature (T_H) was reduced to 1200°C. The oxidation conditions for this screening were identical to those of Figure 4.2.

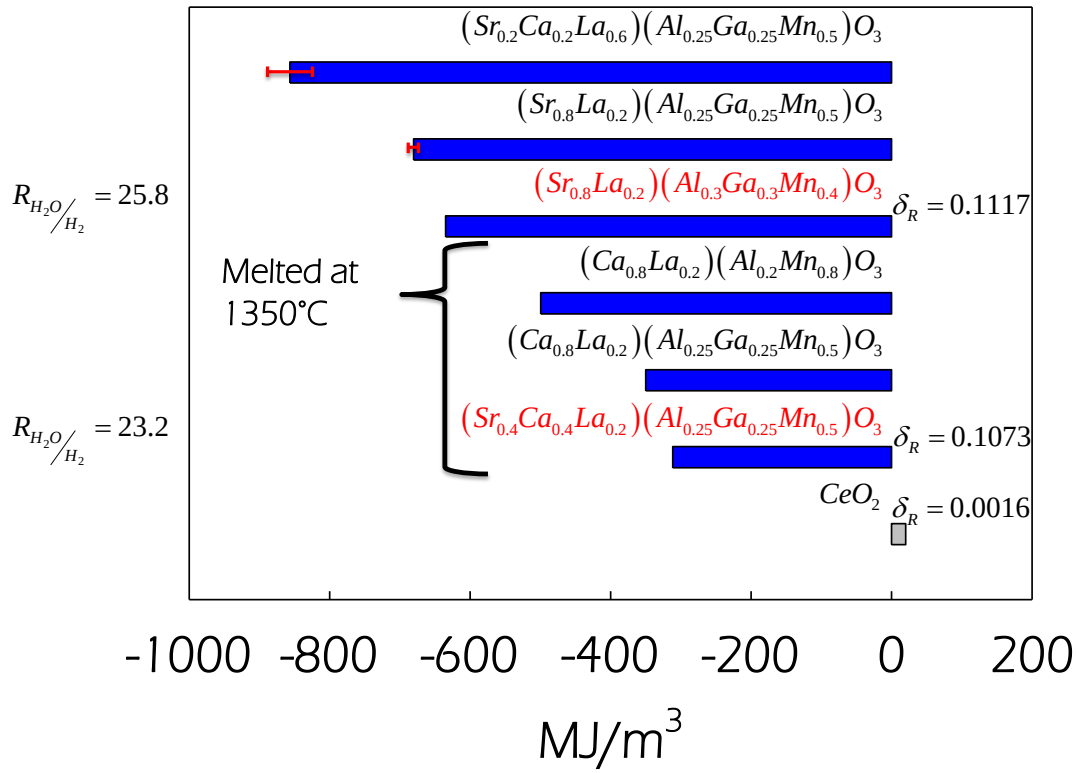

Figure 4.3: Results of second screening of perovskite OSMs. Reduction conditions: T_H=1200°C and p_{O2}=10^{-3}. Oxidation conditions: T_L=500°C and $R_{H2O/H2}$. The measured equilibrium water to hydrogen ratio and achieved off-stoichiometry during reduction is listed on the left and right respectively for materials of interest. The materials that melted at 1350°C are labeled. Best preforming materials are shown in red. For measurements which were repeated, deviations in the results are shown with error bars.

Figure 4.3 shows that for all the screened perovskite samples δ_O is larger than δ_R and the material reduced further under the oxidation conditions than the reduction conditions. Again, much larger water to hydrogen ratios would be required to oxidize these materials after reduction under the examined conditions. However, comparing the δ_R of the best material that melted at 1350°C and the best material which is stable above 1350°C ($(Sr_{0.4}Ca_{0.4}La_{0.2})(Al_{0.25}Ga_{0.25}Mn_{0.5})O_3$ and $(Sr_{0.8}La_{0.2})(Al_{0.3}Ga_{0.3}Mn_{0.4})O_3$ respectively, shown in red) to the δ_R of ceria, we see that their off-stoichiometry is 2

orders of magnitude larger then ceria. If either of these materials could oxidize without prohibitively large amounts of water, they could potentially produce much more hydrogen than ceria, and testing at larger water to hydrogen ratios is warranted.

Example Efficiency calculations from Thermogravimetric Data

In the absence of detailed thermodynamic data for a perovskite OSM that produces more hydrogen per cycle than ceria under the testing conditions of Figure 4.3, example calculations to predict efficiency are performed for a perovskite sample where detailed thermodynamic data was collected. The off stoichiometry of $\left(Sr_{0.2}Ca_{0.2}La_{0.6}\right)\left(Al_{0.25}Ga_{0.25}Mn_{0.5}\right)O_3$ under specific conditions of interest is shown below

.

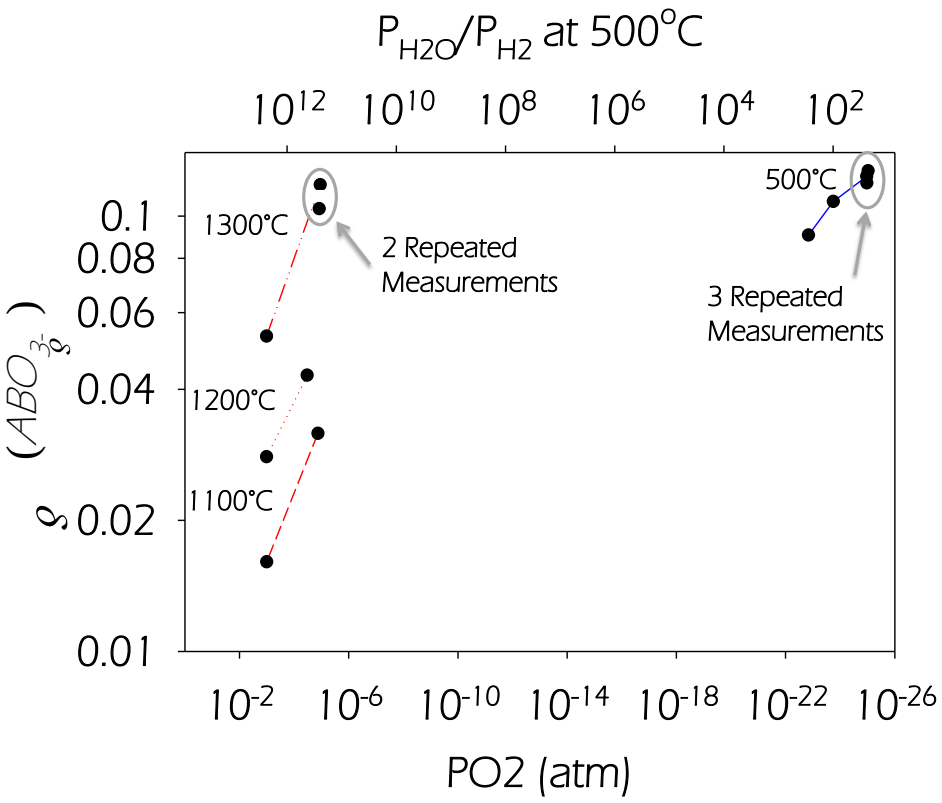

Figure 4.4 Measured off stoichiometry of $(Sr_{0.2}Ca_{0.2}La_{0.6})(Al_{0.25}Ga_{0.25}Mn_{0.5})O_3$ under reducing conditions (1300°C, 1200°C, and 1100°C) and oxidation conditions (500°C) are shown as black dots. Solid points are experimentally determined off-stoichiometry (δ) and solid lines are curve fits. The bottom x-axis show the p_{O2} established for that measurement, and the top x-axis shows the equivalent water to hydrogen ratio needed to establish each p_{O2} at 500°C. Measurements which were repeated are labeled.

The data shown above for $(Sr_{0.2}Ca_{0.2}La_{0.6})(Al_{0.25}Ga_{0.25}Mn_{0.5})O_3$ is similar to the example data shown in Figure 2.15. Here, only one oxidation data point exists with a value of δ_O less than any measured value of δ_R, meaning these two conditions are the only ones investigated which yield a positive fuel production for this OSM (reduction: T_H=1300°C and p_{O2}=10^{-5}, oxidation: T_L=500°C and p_{O2}=1.4×10^{-23}). However, the results of chapter 2 concluded that pump efficiency places a lower limit on p_{O2} much larger than 10^{-5} atm, and these oxidation and reduction conditions will have very small efficiencies

due to the large amount of work required to reduce the p_{O2} below a value of approximately 10^{-3}.

Furthermore, Figure 4.4 shows how the value of δ_R and δ_O for this perovskite sample (approximately 0.1 and 0.09 respectively) are much larger than δ_R and δ_O for ceria under optimized operating conditions (0.02 and 0.002). The result might lead one to think that if δ_O for the perovskite could be decreased further, more hydrogen could be produced per cycle and efficiency would increase. However, the top axis of Figure 4.4 shows how very large water to hydrogen ratios are required to oxidize this sample to a value of δ_O lower than 0.9, which could dramatically reduce efficiency. Ceria, on the other hand, oxidizes to near completion at relatively low water to hydrogen ratios, as seen below.

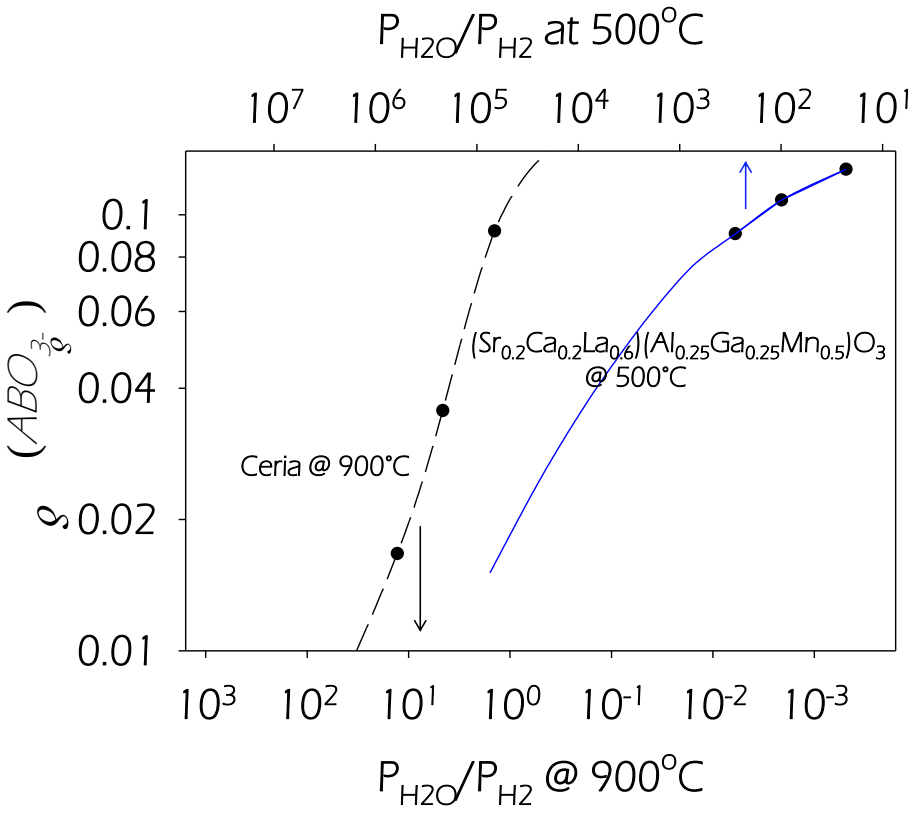

Figure 4.5: Measurements of δ_O for $(Sr_{0.2}Ca_{0.2}La_{0.6})(Al_{0.25}Ga_{0.25}Mn_{0.5})O_3$ at 500°C and ceria at 900°C plotted against the equivalent water to hydrogen ratio at each oxidation temperature.

Similar to the discussion in Chapter 3, the comparison of Figure 4.5 shows how OSMs that produce more hydrogen per cycle do not necessarily result in higher thermochemical conversion efficiencies. With the aim of discovering which material will achieve higher conversion efficiencies, the thermogravimetric data shown in Figure 4.4 will be curve fit and extrapolated to lower values of p_{O2} and δ_O in order to perform efficiency calculations which will be compared to ceria under optimal operating conditions. This extrapolation and the cycles to be calculated are shown below.

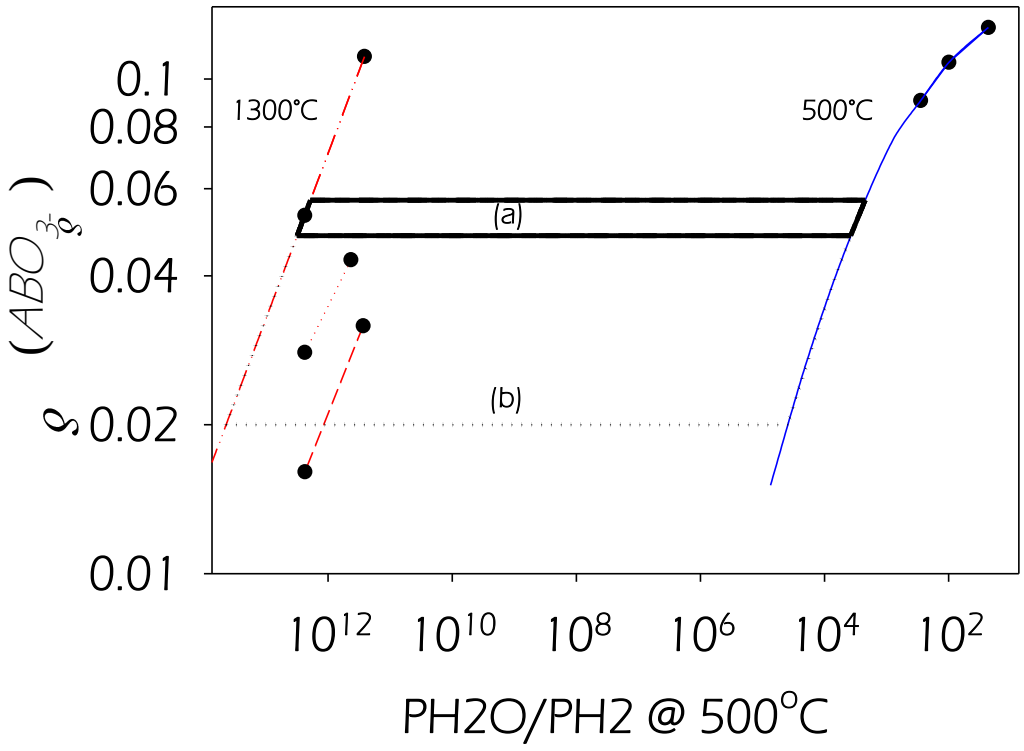

Figure 4.6: Measured off stoichiometry of $(Sr_{0.2}Ca_{0.2}La_{0.6})(Al_{0.25}Ga_{0.25}Mn_{0.5})O_3$ under reducing conditions at 1300°C and oxidizing conditions at 500°C. The red and blue lines are the extrapolated values used for efficiency calculations. The black solid lines represent cycle (a) and black dotted lines represent cycle (b).

It should be noted that the extrapolations may not correspond to the exact value of δ for these conditions and thermogravimetric measurements for higher values of p_{O2} should be made if accurate efficiency predictions are desired. However, at 500°C higher values of p_{O2} were not possible because hydrogen ratios required to completely oxidize this material are larger than the values that can be achieved by the gas handling equipment of this experimental setup. These ratios are so large that the efficiency penalty from heating that much water will certainly result in very low thermochemical conversion efficiencies. Thus further characterization of this material is unnecessary. In any case,

using the extrapolated data shown in Figure 4.4 for $(Sr_{0.2}Ca_{0.2}La_{0.6})(Al_{0.25}Ga_{0.25}Mn_{0.5})O_3$, the efficiency model of Chapter 2 can be applied. The results of these calculations are shown below.

Table 4.1: Efficiency, energy factors, and operational parameters for ceria and $(Sr_{0.2}Ca_{0.2}La_{0.6})(Al_{0.25}Ga_{0.25}Mn_{0.5})O_3$ calculated from the TGA results of Figure 4.4 (optimized with $\varepsilon_S = 0.5$ and $\varepsilon_G = 0.9$). ΔH of the perovskites was assumed to be that of ceria.

	Ceria	$(Sr_{0.2}Ca_{0.2}La_{0.6})(Al_{0.25}Ga_{0.25}Mc_{0.5})O_3$	
	a)	b)	c)
T_L	925	500	500
T_H	1500	1300	1300
p_{O2}(atm)	0.0018	0.0007	0.0007
δ_R	0.02	0.057	0.057
δ_O	0.002	0.048	0.02
F_{Reheat}	4.6	12.7	3
F_{RXN}	1.6	1.6	1.6
F_{water}	0.4	61.6	237
F_{pump}	0.8	7.6	2.2
Efficiency %	13.523	0.012	0.004

Table 4.1 shows how even at lower values of T_H (1300°C) this material can produce as much as 0.037 moles of hydrogen per mole of OSM per cycle ($n_{H_2} = \delta_R - \delta_O$, column c). This is more than double the hydrogen production of ceria under optimized *operational parameters* with high reduction temperatures (T_H=1500°C, column a). Under the conditions of column c, increased hydrogen production and lower reduction temperature result in a smaller value of F_{Reheat} (the largest energy factor for ceria). However, because the material requires large oxygen partial pressures to oxidize, prohibitively large amounts of water are needed and an extremely large value of F_{Water} results in very low efficiencies. This low efficiency is in part caused by the lower

reduction temperature which establishes a lower value of p_{O2} during oxidation for fixed water to hydrogen ratios.

Furthermore, even though a relatively large amount of hydrogen is produced per cycle with these perovskites under the conditions of column c, the efficiency is less than that of ceria and these conditions are also not the optimum operating conditions of this specific OSM. By not oxidizing the material to completion, less hydrogen is produced per cycle. However, by not oxidizing the material to a large extent, a higher NRC efficiency results because smaller amounts of water are needed (column b). This column was produced by optimizing δ_R and δ_O when T_H is limited to 1300°C and T_L is limited to 500°C. Here, 0.09 moles of hydrogen per mole of OSM are produced per cycle which is half of that produced by of ceria in column a.

This calculated efficiency for the perovskite under two different operating conditions show that while these materials may initially look promising as an OSM for NRCs because of their high OSC (producing large amounts of hydrogen per cycle), system level considerations show that it will not perform as well as ceria. Such a conclusion cannot be made when only OSC is measured without tracking the water needed for oxidation (Figure 2.16). This further demonstrates the importance of chemical conversion when screening OSM.

CHAPTER 5

SUMMARY AND CONCLUSIONS

With the aim of developing a clean, sustainable energy infrastructure, great progress has been made to identify and utilize energy sources other than fossil fuels. However, the challenge of dispatched energy storage and fuel generation for the transportation sector remains daunting. Solar driven NRCs have the potential to solve this problem, but the implementation of efficient cycles has not been demonstrated. The low efficiencies of current systems result from both reactor design (heat recovery) and non-optimized OSMs. Furthermore, the complex coupling of reactor design, OSM thermochemical properties, and system *operational parameters* make the task of demonstrating high efficiencies in NRCs complicated.

By modeling this highly coupled system and accounting for the pressure dependence of vacuum pump efficiencies and chemical conversion of water to hydrogen, predictions for the upper limit of system efficiency were made. This work provides a framework which can be used to screen materials. Previously, new OSMs were evaluated based solely on OSC under non optimum conditions, ignoring the penalty of oxidizing with excessive amounts of water or reducing with large amounts of vacuum pump work. By applying this approach to the screening of new OSMs, the ultimate figure of merit (NRC efficiency) can be used to compare two materials. This in turn provides an unambiguous way to evaluate and compare new OSMs when screening many materials. Additionally, by applying this model to fictitious materials with selected properties, we can gain insight to guide the design of new OSMs.

Through application of a series of justified assumptions in Chapter 2, the ideal OSM ΔH for a "ceria like" material was shown to be less than that of ceria but greater than water thermolysis and highly dependent on the lower limit for the oxidation

temperature. Estimating the lower limit for oxidation temperature to be on the order of 500°C, the ideal value of ΔH is expected to be approximately 140% of the enthalpy of water thermolysis. However, with the goal of discovering an OSM with a ΔH in this range, few alloy choices and relatively lower alloy solubility levels make ceria a less attractive base OSM material. On the other hand, the perovskite structure does not have these limitations and may be a better choice. Furthermore, not only have these materials already been shown to be a viable OSM capable of splitting water, but they also have an OSC larger than that of ceria, and previous studies have shown these materials have a ΔH which is tunable via alloying.

This large value for OSC of many perovskites materials make them attractive for NRCs because increasing the hydrogen production per cycle could increase efficiency. To determine if this high OSC will lead to high efficiency in an actually reactor, TGA experiments were conducted to both evaluate the OSC of a material and provide insight into the water needed for oxidation, which are two key indicators of the efficiencies possible with a specific OSM. Using this approach, two batches of TGA experiments were conducted to screen many perovskites as OSMs. Of these materials, none of them out preformed ceria under conditions expect to yield high efficiencies in NRCs. However, the two best preforming were identified and future work discussed. This work should focus on more detailed characterization of these materials and determine if they will increase the thermochemical conversion efficiencies of NRCs. While these measurements have not yet been made for the materials of interest, the necessary measurements and calculations are outlined in an example using a perovskite where a partial off-stoichiometric map was determined. While this calculation show that this OSM requires very large amounts of water to oxidize and will not have higher system efficiencies than ceria(as expected from the OSM screening results), other perovskites of interest may oxidize at a lower values of p_{O2}, requiring less water. This would lead to higher

efficiencies in actual reactors and further advance the effort to realize the implementation of NRCs to produce a dispatchable fuel from concentrated solar power.

APPENDIX A: MINIMUM AMOOUT OF WORK REQUIED BY A VACCUM PUMP

Choosing the control volume around the entire pump, an energy balance shows.

$$W_{in} - q_{out} = \Delta h + \Delta E_{kinetic} + \Delta E_{potential} \tag{1}$$

Assuming the system is adiabatic.

$$q_{out} = 0 \tag{2}$$

Ignoring changes in kenotic an potential energy.

$$W_{in} = \Delta h = \int_{in}^{out} Tds + \int_{in}^{out} vdP \tag{3}$$

Assuming the process is reversible.

$$Tds = \delta q = 0 \tag{4}$$

$$W_{in} = \int_{in}^{out} vdP \tag{5}$$

Assuming an ideal gas.

$$v = \frac{RT}{P} \tag{6}$$

$$W_{in} = RT \int_{in}^{out} \frac{1}{P} dP \tag{7}$$

Showing the work required to produce a vacuum per mole of gas is

$$W_{in} = RT \ln\left(\frac{P_{out}}{P_{in}}\right) \tag{8}$$

REFERENCES

1. *IEA's World Energy Outlook 2013.*

2. Chaisson, E.J., *Long-Term Global Heating from Energy Usage.* Eos, Transactions American Geophysical Union, 2008. **89**(28): p. 253-254.

3. Aleklett, K., et al., *The Peak of the Oil Age - Analyzing the world oil production Reference Scenario in World Energy Outlook 2008.* Energy Policy, 2010. **38**(3): p. 1398-1414.

4. Ngoh, S.K. and D. Njomo, *An overview of hydrogen gas production from solar energy.* Renewable & Sustainable Energy Reviews, 2012. **16**(9): p. 6782-6792.

5. Holladay, J.D., et al., *An overview of hydrogen production technologies.* Catalysis Today, 2009. **139**(4): p. 244-260.

6. Hasuike, H., et al., *Study on design of molten salt solar receivers for beam-down solar concentrator.* Solar Energy, 2006. **80**(10): p. 1255-1262.

7. Lata, J.M., M. Rodríguez, and M.Á. de Lara, *High Flux Central Receivers of Molten Salts for the New Generation of Commercial Stand-Alone Solar Power Plants.* Journal of Solar Energy Engineering, 2008. **130**(2): p. 021002-021002.

8. Chueh, W.C. and S.M. Haile, *A thermochemical study of ceria: exploiting an old material for new modes of energy conversion and CO2 mitigation.* Philosophical Transactions of the Royal Society a-Mathematical Physical and Engineering Sciences, 2010. **368**(1923): p. 3269-3294.

9. Funk, J.E. and Reinstro.Rm, *Energy Requirements in Production of Hydrogen from Water.* Industrial & Engineering Chemistry Process Design and Development, 1966. **5**(3): p. 336-342.

10. Nakamura, T., *Hydrogen Production from Water Utilizing Solar Heat at High-Temperatures.* Solar Energy, 1977. **19**(5): p. 467-475.

11. Steinfeld, A., et al., *Solar thermal production of zinc and syngas via combined ZnO-reduction and CH_4-reforming processes (vol 20, pg 793, 1995).* International Journal of Hydrogen Energy, 1996. **21**(3): p. 243-243.

12. Funk, J.E., *Thermochemical hydrogen production: past and present.* International Journal of Hydrogen Energy, 2001. **26**(3): p. 185-190.

13. Steinfeld, A., *Solar thermochemical production of hydrogen - a review.* Solar Energy, 2005. **78**(5): p. 603-615.

14. Gibson, T.L. and N.A. Kelly, *Optimization of solar powered hydrogen production using photovoltaic electrolysis devices.* International Journal of Hydrogen Energy, 2008. **33**(21): p. 5931-5940.

15. Siegel, N.P., et al., *Factors Affecting the Efficiency of Solar Driven Metal Oxide Thermochemical Cycles.* Industrial & Engineering Chemistry Research, 2013. **52**(9): p. 3276-3286.

16. Fletcher, E.A., *Solarthermal processing: A review.* Journal of Solar Energy Engineering-Transactions of the Asme, 2001. **123**(2): p. 63-74.

17. Ni, M., et al., *A review and recent developments in photocatalytic water-splitting using for hydrogen production.* Renewable and Sustainable Energy Reviews, 2007. **11**(3): p. 401-425.

18. Esswein, A.J. and D.G. Nocera, *Hydrogen production by molecular photocatalysis.* Chemical reviews, 2007. **107**(10): p. 4022-4047.

19. Perkins, C. and A.W. Weimer, *Likely near-term solar-thermal water splitting technologies.* International Journal of Hydrogen Energy, 2004. **29**(15): p. 1587-1599.

20. Baykara, S.Z., *Hydrogen production by direct solar thermal decomposition of water, possibilities for improvement of process efficiency.* International Journal of Hydrogen Energy, 2004. **29**(14): p. 1451-1458.

21. Wagner, M.J., S.A. Klein, and D.T. Reindl. *Simulation of Utility-Scale Central Receiver System Power Plants*. in *ASME 2009 3rd International Conference on Energy Sustainability collocated with the Heat Transfer and InterPACK09 Conferences*. 2009. American Society of Mechanical Engineers.

22. Martin, S., *Fired up about Efficiency, .* Pictures of the Future 2013, Siemins AG.

23. Henry, A. and R. Prasher, *The prospect of high temperature solid state energy conversion to reduce the cost of concentrated solar power.* Energy & Environmental Science, 2014. **7**(6): p. 1819-1828.

24. Osterloh, F.E. and B.A. Parkinson, *Recent developments in solar water-splitting photocatalysis.* Mrs Bulletin, 2011. **36**(1): p. 17-22.

25. Baykara, S.Z., *Experimental solar water thermolysis.* International Journal of Hydrogen Energy, 2004. **29**(14): p. 1459-1469.

26. Bockris, J.O., et al., *On the Splitting of Water.* International Journal of Hydrogen Energy, 1985. **10**(3): p. 179-201.

27. Abanades, S., et al., *Screening of water-splitting thermochemical cycles potentially attractive for hydrogen production by concentrated solar energy.* Energy, 2006. **31**(14): p. 2805-2822.

28. Zinkevich, M., D. Djurovic, and F. Aldinger, *Thermodynamic modelling of the cerium-oxygen system.* Solid State Ionics, 2006. **177**(11-12): p. 989-1001.

29. Chueh, W.C., et al., *High-Flux Solar-Driven Thermochemical Dissociation of CO_2 and H_2O Using Nonstoichiometric Ceria.* Science, 2010. **330**(6012): p. 1797-1801.

30. Keene, D.J., J.H. Davidson, and W. Lipinski, *A Model of Transient Heat and Mass Transfer in a Heterogeneous Medium of Ceria Undergoing Nonstoichiometric Reduction.* Journal of Heat Transfer-Transactions of the Asme, 2013. **135**(5).

31. Diver, R.B., et al., *Solar thermochemical water-splitting ferrite-cycle heat engines.* Journal of Solar Energy Engineering-Transactions of the Asme, 2008. **130**(4).

32. Lapp, J., J.H. Davidson, and W. Lipinski, *Efficiency of two-step solar thermochemical non-stoichiometric redox cycles with heat recovery.* Energy, 2012. **37**(1): p. 591-600.

33. Furler, P., et al., *Solar thermochemical CO_2 splitting utilizing a reticulated porous ceria redox system.* Energy & Fuels, 2013. **26**(11): p. 7051-7059.

34. Xu, R. and T.F. Wiesner, *Dynamic model of a solar thermochemical water-splitting reactor with integrated energy collection and storage.* International Journal of Hydrogen Energy, 2012. **37**(3): p. 2210-2223.

35. Ermanoski, I., N.P. Siegel, and E.B. Stechel, *A New Reactor Concept for Efficient Solar-Thermochemical Fuel Production.* Journal of Solar Energy Engineering-Transactions of the Asme, 2013. **135**(3).

36. Bader, R., et al., *Thermodynamic Analysis of Isothermal Redox Cycling of Ceria for Solar Fuel Production.* Energy & Fuels, 2013. **27**(9): p. 5533-5544.

37. Wei, B., et al., *Review on the two-step-conversion of CO_2 driven by solar energy.* The Journal of MacroTrends in Energy and Sustainability. **1**(1): p. 139-160.

38. Muhich, C.L., et al., *Efficient Generation of H_2 by Splitting Water with an Isothermal Redox Cycle.* Science, 2013. **341**(6145): p. 540-542.

39. Kim, J., et al., *Methanol production from CO_2 using solar-thermal energy: process development and techno-economic analysis.* Energy & Environmental Science, 2011. **4**(9): p. 3122-3132.

40. Kim, J., et al., *Fuel production from CO_2 using solar-thermal energy: system level analysis.* Energy & Environmental Science, 2012. **5**(9): p. 8417-8429.

41. Loutzenhiser, P.G. and A. Steinfeld, *Solar syngas production from CO_2 and H_2O in a two-step thermochemical cycle via Zn/ZnO redox reactions: Thermodynamic cycle analysis.* International Journal of Hydrogen Energy, 2011. **36**(19): p. 12141-12147.

42. Meredig, B. and C. Wolverton, *First-principles thermodynamic framework for the evaluation of thermochemical H_2O- or CO_2-splitting materials (vol 80, 245119, 2009).* Physical Review B, 2011. **83**(23).

43. Scheffe, J.R. and A. Steinfeld, *Thermodynamic Analysis of Cerium-Based Oxides for Solar Thermochemical Fuel Production.* Energy & Fuels, 2012. **26**(3): p. 1928-1936.

44. Schneider, D., M. Godickemeier, and L.J. Gauckler, *Nonstoichiometry and defect chemistry of ceria solid solutions.* Journal of Electroceramics, 1997. **1**(2): p. 165-172.

45. Panhans, M.A. and R.N. Blumenthal, *A Thermodynamic and Electrical-Conductivity Study of Nonstoichiometric Cerium Dioxide.* Solid State Ionics, 1993. **60**(4): p. 279-298.

46. McDaniel, A.H., et al., *Sr and Mn doped $LaAlO_{3-\delta}$ for solar thermochemical H_2 and CO production.* Energy & Environmental Science, 2013. **6**(8): p. 2424-2428.

47. McDaniel, A.H., et al., *Sr- and Mn-doped $LaAlO_{3-\delta}$ for solar thermochemical H_2 and CO production.* Energy & Environmental Science, 2013. **6**(8): p. 2424-2428.

48. Scheffe, J.R., D. Weibel, and A. Steinfed, *Lanthanum-Strontium-Manganese Perovskites as Redox Materials for Solar Thermochemical Splitting of H_2O and CO_2.* Energy & Fuels, 2013. **27**(8): p. 4250-4257.

49. Scheffe, J.R., J.H. Li, and A.W. Weimer, *A spinel ferrite/hercynite water-splitting redox cycle.* International Journal of Hydrogen Energy, 2010. **35**(8): p. 3333-3340.

50. Çengel, Y.A. and M.A. Boles, *Thermodynamics: an engineering approach*. 2006: McGraw-Hill Higher Education.

51. Furler, P., J.R. Scheffe, and A. Steinfeld, *Syngas production by simultaneous splitting of H_2O and CO_2 via ceria redox reactions in a high-temperature solar reactor.* Energy & Environmental Science, 2012. **5**(3): p. 6098-6103.

52. Lange, M., et al., *T–S diagram efficiency analysis of two-step thermochemical cycles for solar water splitting under various process conditions.* Energy. **67**: p. 298-308.

53. Lapp, J. and W. Lipiński, *Transient Three-Dimensional Heat Transfer Model of a Solar Thermochemical Reactor for H_2O and CO_2 Splitting Via Nonstoichiometric Ceria Redox Cycling.* Journal of Solar Energy Engineering, 2014. **136**(3).

54. Incropera, F.P., et al., *Fundamentals of Heat and Mass Transfer*. 2007.

55. Lapp, J., J.H. Davidson, and W. Lipiński, *Heat Transfer Analysis of a Solid-Solid Heat Recuperation System for Solar-Driven Nonstoichiometric Redox Cycles.* Journal of Solar Energy Engineering, 2013. **135**(3): p. 031004-031004.

56. Miller, J.E., A.H. McDaniel, and M.D. Allendorf, *Considerations in the Design of Materials for Solar-Driven Fuel Production Using Metal-Oxide Thermochemical Cycles.* Advanced Energy Materials, 2014. **4**(2).

57. Steinfeld, A., S. Sanders, and R. Palumbo, *DESIGN ASPECTS OF SOLAR THERMOCHEMICAL ENGINEERING—A CASE STUDY: TWO-STEP WATER-SPLITTING CYCLE USING THE Fe_3O_4/FeO REDOX SYSTEM.* Solar Energy, 1999. **65**(1): p. 43-53.

58. H. Häring, C.A., *Industrial Gas Processing*. 2008, New York: Wiley-VCH.

59. Bader, R., et al., *Solar syngas production via isothermal nonstoichiometric redox cycling of ceria with heat recovery.* Abstracts of Papers of the American Chemical Society, 2013. **245**.

60. Rormark, L., et al., *Enthalpies of oxidation of $CaMnO_{3-\delta}$, $Ca_2MnO_{4-\delta}$and $SrMnO_{3-\delta}$ - Deduced redox properties.* Chemistry of Materials, 2001. **13**(11): p. 4005-4013.

61. Mizusaki, J., et al., *Oxygen nonstoichiometry and defect equilibrium in the perovskite-type oxides $La_{1-x}Sr_xMnO_{3}^{+d}$*. Solid State Ionics, 2000. **129**(1-4): p. 163-177.

62. Andersson, D.A., et al., *Redox properties of CeO_2-MO_2 (M=Ti, Zr, Hf, or Th) solid solutions from first principles calculations.* Applied Physics Letters, 2007. **90**(3).

63. Yang, Z., T.K. Woo, and K. Hermansson, *Effects of Zr doping on stoichiometric and reduced ceria: A first-principles study.* Journal of Chemical Physics, 2006. **124**(22).

64. Dutta, G., et al., *Origin of enhanced reducibility/oxygen storage capacity of $Ce_{1-x}Ti_xO_2$ compared to CeO_2 or TiO_2.* Chemistry of Materials, 2006. **18**(14): p. 3249-3256.

65. Zhou, G., J. Hanson, and R.J. Gorte, *A thermodynamic investigation of the redox properties of ceria-titania mixed oxides.* Applied Catalysis a-General, 2008. **335**(2): p. 153-158.

66. Kim, T., J.M. Vohs, and R.J. Gorte, *Thermodynamic investigation of the redox properties of ceria-zirconia solid solutions.* Industrial & Engineering Chemistry Research, 2006. **45**(16): p. 5561-5565.

67. Zhou, G., et al., *Oxidation entropies and enthalpies of ceria-zirconia solid solutions.* Catalysis Today, 2007. **123**(1-4): p. 86-93.

68. Aguileragranja, F. and J.L. Moranlopez, *Specific-Heat and the Phase-Diagram of the Ising Square Lattice with Nearest-(Ji) and Next-Nearest Interactions.* Journal of Physics-Condensed Matter, 1993. **5**: p. A195-A196.

69. Singh, P. and M.S. Hegde, *$Ce_{0.67}Cr_{0.33}O_{2.11}$: A New Low-Temperature O_2 Evolution Material and H_2 Generation Catalyst by Thermochemical Splitting of Water.* Chemistry of Materials, 2009. **22**(3): p. 762-768.

70. Chueh, W.C. and S.M. Haile, *Ceria as a Thermochemical Reaction Medium for Selectively Generating Syngas or Methane from H_2O and CO_2.* Chemsuschem, 2009. **2**(8): p. 735-739.

71. Nalbandian, L., A. Evdou, and V. Zaspalis, *$La_{(1-x)}Sr_{(x)}MO_{(3)}$ (M = Mn, Fe) perovskites as materials for thermochemical hydrogen production in conventional and membrane reactors.* International Journal of Hydrogen Energy, 2009. **34**(17): p. 7162-7172.

72. Demont, A., S. Abanades, and E. Beche, *Investigation of Perovskite Structures as Oxygen-Exchange Redox Materials for Hydrogen Production from Thermochemical Two-Step Water-Splitting Cycles.* The Journal of Physical Chemistry C, 2014. **118**(24): p. 12628-12692.

73. Jiang, Q., et al., *Thermochemical CO_2 splitting reaction with supported $La_xA_{1-x}Fe_yB_{1-y}O_3$ (A=Sr, Ce, B=Co, Mn) perovskite oxides.* Solar Energy, 2014. **103**(0): p. 425-437.

74. Kawakami, S., et al., *Thermochemical Two-step Water Splitting Cycle using Ni-ferrite and CeO_2 Coated Ceramic foam Devices by Concentrated Xe-light Radiation.* Energy Procedia, 2014. **49**(0): p. 1980-1989.

75. Kodama, T., et al., *Thermochemical hydrogen production by a redox system of ZrO_2-supported Co(II)-ferrite.* Solar Energy, 2005. **78**(5): p. 623-631.

76. Kaneko, H., et al., *Solar thermochemical process for hydrogen production using ferrites.* Energy, 2005. **30**(11–12): p. 2171-2178.

77. Daza, Y.A., et al., *Carbon Dioxide Conversion by Reverse Water–Gas Shift Chemical Looping on Perovskite-Type Oxides.* Industrial & Engineering Chemistry Research, 2014. **53**(14): p. 5828-5837.

78. Chueh, W.C. and S.M. Haile, *Ceria as a Thermochemical Reaction Medium for Selectively Generating Syngas or Methane from H_2O and CO_2*

ChemSusChem, 2009. **2**(8): p. 735-739.

79. Keene, D.J., J.H. Davidson, and W. Lipiński, *A Model of Transient Heat and Mass Transfer in a Heterogeneous Medium of Ceria Undergoing Nonstoichiometric Reduction.* Journal of Heat Transfer, 2013. **135**(5): p. 052701-052701.

80. McDaniel, A.H., et al., *Sr- and Mn-doped LaAlO3-delta for solar thermochemical H-2 and CO production.* Energy & Environmental Science, 2013. **6**(8): p. 2424-2428.

81. Yang, L., O. Kresnawahjuesa, and R.J. Gorte, *A calorimetric study of oxygen-storage in Pd/ceria and Pd/ceria-zirconia catalysts.* Catalysis Letters, 2001. **72**(1-2): p. 33-37.

82. Inaba, H. and H. Tagawa, *Ceria-based solid electrolytes.* Solid State Ionics, 1996. **83**(1–2): p. 1-16.

83. Yao, H.C. and Y.F.Y. Yao, *Ceria in Automotive Exhaust Catalysts .1. Oxygen Storage.* Journal of Catalysis, 1984. **86**(2): p. 254-265.

84. Bozo, C., N. Guilhaume, and J.-M. Herrmann, *Role of the Ceria–Zirconia Support in the Reactivity of Platinum and Palladium Catalysts for Methane Total Oxidation under Lean Conditions.* Journal of Catalysis, 2001. **203**(2): p. 393-406.

85. Ghom, S.A., et al., *Oxygen sensing with mesoporous ceria–zirconia solid solutions.* Sensors and Actuators B: Chemical, 2009. **140**(1): p. 216-221.

86. Rynkowski, J., et al., *Redox behaviour of ceria-titania mixed oxides.* Applied Catalysis a-General, 2000. **203**(2): p. 335-348.

87. Gorte, R.J., et al., *Thermodynamic investigation of the redox properties of ceria-zirconia solid solutions.* Abstracts of Papers of the American Chemical Society, 2006. **231**.

88. Grau-Crespo, R., et al., *Phase separation and surface segregation in ceria-zirconia solid solutions.* Proceedings of the Royal Society a-Mathematical Physical and Engineering Sciences, 2011. **467**(2131): p. 1925-1938.

89. Quinelato, A.L., et al., *Synthesis and sintering of ZrO_2-CeO_2 powder by use of polymeric precursor based on Pechini process.* Journal of Materials Science, 2001. **36**(15): p. 3825-3830.

90. Sakka, S., *Sol-Gel Science and Technology Processing Characterization and Applications*. Sol-Gel Procession, ed. S. Sakka. Vol. 1. 2005, Norwell, Massachusetts: Kluwer Academic Publisher.

91. Luo, M.-F., et al., *Redox Properties of $Ce_xZr_{1-x}O_2$ Mixed Oxides Prepared by the Sol–gel Method.* Journal of Materials Science Letters, 1998. **17**(18): p. 1553-1557.